

الجمهورية الجزائرية الديمقراطية الشعبية
République Algérienne Démocratique et Populaire
وزارة التعليم العالي و البحث العلمي
Ministère de l'enseignement supérieur et de la recherche scientifique

Université Mohamed Khider – Biskra

Faculté des Sciences et de la technologie

Département : Génie Mécanique

Ref :



جامعة محمد خيضر بسكرة
كلية العلوم و التكنولوجيا
قسم: الهندسة الميكانيكية
المرجع:

ETUDE DE SYSTEME DE RECUPERATION D'ENERGIE PAR ASSOCIATION DE PALES BATTANTES AUX PALES D'EOLIENNE DE PROFILE NACA.

Thèse présentée en vue de l'obtention
Du diplôme de
Doctorat en sciences en Génie mécanique

Présentée par :

Bouzaher Mohamed Taher

Soutenue publiquement le 24 /05 / 2017

Devant le jury composé de :

Pr BRIMA Abd Hafid	Professeur, Université de Biskra	Président
Dr DERFOUF Semch eddine	Maître de Conférences, Université de Biskra	Rapporteur
Pr BRIOUA Mourad	Professeur, Université de Batna -2-	Examineur
Dr MASMOUDI Kamel	Maître de Conférences, Université de Batna -1-	Examineur
Dr DJOUIMAA Siham	Maître de Conférences, Université de Batna -1-	Examineur
Pr HADID Mohamed	Professeur, Université de Biskra	Co- rapporteur

الجمهورية الجزائرية الديمقراطية الشعبية
République Algérienne Démocratique et Populaire
وزارة التعليم العالي و البحث العلمي
Ministère de l'enseignement supérieur et de la recherche scientifique

University of Mohamed Khider – Biskra

Faculty of sciences and technology

Department: Mechanical Engineering

Ref :.....



جامعة محمد خيضر بسكرة
كلية العلوم و التكنولوجيا
قسم: الهندسة الميكانيكية
المرجع:.....

A STUDY OF A SYSTEM FOR ENERGY RECOVERING BY THE ASSOCIATION OF FLAPPING FOILS TO WINDMILL BLADES

ETUDE DE SYSTEME DE RECUPERATION D'ENERGIE PAR ASSOCIATION DE PALES BATTANTE AUX
PALES D'EOLIENNE DE PROFFILE NACA

A dissertation submitted in partial fulfillment
of the requirements for the degree of

Doctor of Science in Mechanical Engineering

Option: Mechanical Engineering

Presented by:

Bouzaher Mohamed Taher

Publicly defended the 24 /05 /2017

Board of Examiners:

Pr BRIMA Abd Hafid	Professor, University of Biskra	Chair
Dr DERFOUF Semch eddine	Associate Professor, University of Biskra	Supervisor
Pr BRIOUA Mourad	Professor, University of Batna -2-	Examiner
Dr MASMOUDI Kamel	Associate Professor, University of Batna -1-	Examiner
Dr DJOUIMAA Siham	Associate Professor, University of Batna -1-	Examiner
Pr HADID Mohamed	Professor, University of Biskra	Co- Supervisor

ACKNOWLEDGMENTS

I am pleased to express my deepest thankfulness to my advisor, Dr. Derfouf Semche Eddine, for his supervision and care. I am also appreciative for his patience and continuous encouragement throughout my research activity. I would also like to thank Pr. Hadid Mohamed, for his supervision and care.

I would also like to thank Pr BRIMA Abd Hafid, Pr BRIOUA Mourad, Dr MASMOUDI Kamel and Dr DJOUIMAA Siham for serving as members of my supervisory committee.

I would like to thank all my colleagues of the department of Mechanical Engineering for their friendship and support.

Finally, I would like to thank my parents for their understanding, patience and encouragement when it was most needed.

Table of Contents

List of Figures.....	V
List of Tables.....	VIII
List of Symbols.....	IX
General Introduction.....	1

Chapter I: Literature review

I.1. Introduction	4
I.2. Renewable energies.....	4
I.2.1. Wind energy.....	4
I.2.2. Wind energy utilization	5
I.3 Vertical axis wind turbines (VAWT)	7
I.4 Different types of VAWT.....	7
I.4.1. Egg-beater type Darrieus wind turbine	8
I.4.2. Straight bladed type Darrieus wind turbine	9
I.4.3 Variable geometry oval trajectory (VGOT) Darrieus turbine.....	10
I.4.4 Darrieus–Masgrowe (two-tier) rotor.....	10
I.4.5 Crossflex wind turbine	11
I.4.6 Two leaf semi rotary VAWT.....	12
I.4.7 Savonius rotor	12
I.4.8 Combined Savonius and Darrieus rotor.....	13
I.4.9 Sistan type wind mill	14
I.5. Types of support structures for curved- and straight-blades Darrieus VAWTs.	14
I.6. Horizontal axis turbines	15
I.7. Comparison among different turbine efficiency's	16
I.8. VAWT keys parameters	17
I.9. Dynamic stall	20
I.10. Types of stall	21
I.10.1. Static stall.....	21
I.10.2. Dynamic stall	23
I.10.3. Dynamic stall in a Darrieus turbine	25

I.11. General notes about the flow control	27
I.11.1. The challenges of controlling flows	28
I.11.2. Relations between the different objectives of control.....	29
I.11.3. Classification of flow control methods	29
I.12. Problematic of active control	31
I.12.1. Flow control by using moving wall	31
I.12.2. Flow control by suction and blowing.....	32
I.12.3. Thermal control.....	33
I.12.4. Flows control by using flapping wings	33
I.12.5. Flow control by flexible wing.....	35
I.12.6. Other types of active control.....	36
I.13. Problematic of passive control.....	36
I.13.1. Different types of passive actuators	36
I.13.2. Passive vortex generators.....	36
I.13.3. Adding solids	37
I.14. Conclusion	37

Chapter II: Numerical Methodology

II.1. Introduction	38
II.2. Turbulence modeling.....	39
II.2.1. DNS (Direct Numerical Simulation)	39
II.2.2. Statistical approaches (RANS)	39
II.2.3. Large Eddy Simulation LES.....	39
II.3. Historic review of numerical models employed for VAWT simulation	40
II.3.1. The realizable $k - \epsilon$ model.....	41
II.3.2. The Large Eddy Simulations model	42
II.4. Near-Wall treatments in ANSYS Fluent	42
II.5. Wall functions vs. Near-Wall model	43
II.6. Flow control by using backward flapping wings.....	43
II.6.1. Model description	45
II.6.2. Motion modeling	47
II.6.3. Computational domain and boundary condition.....	48

II.6.4. Meshing strategy.....	50
II.6.5. Dynamic update mesh strategy.....	52
II.7. Flow control by using flexible flapping wings.....	54
II.7.1. Problem description.....	54
II.7.2. Motion modeling.....	54
II.7.3. Meshing strategy.....	58
II.7.4. Dynamic update mesh strategy.....	59
II.8. Conclusion.....	59

Chapter III: Results and Discussion

III.1 Introduction.....	60
III.2. Simulation of the flow across a vertical axis wind turbine (rigid blade).....	61
III.3. Flow control by using flexible blades.....	65
III.3.1. Model validation.....	65
III.3.2. Mechanism of turbine performance improvement.....	66
III.3.3. Internal flexion versus external flexion.....	69
III.3.4. Output power.....	69
III.3.5. Airfoil shape effect.....	75
III.3.6. Effect of flexible coefficient n	79
III.3.7. Effect of flexible coefficient L_c	80
III.4. Flow control by flexible deformable blade with a time varying camber deformation (Tidal turbine).....	81
III.4.1. Mechanism of the VATT performance improvement.....	83
III.4.2. Output power.....	84
III.5. Flow control by using two backward flapping wings.....	88
III.5.1. The effect of the proposed device on the turbine performance.....	89
III.6. Comparison among flow control techniques.....	90
III.7. Conclusion.....	92
GENERAL CONCLUSIONS.....	94
BIBLIOGRAPHY.....	97

List of Figures

Chapter I: Literature review

Fig.I.1. Global renewable power capacity (REN21 2014)	4
Fig.I.2. Global cumulative capacity of wind energy (GWEC 2012)	5
Fig.I.3. Annual and cumulative growth in U.S. wind power capacity.....	6
Fig.I.4. Wind energy generation capacity by country (TECHNICA 2012)	6
Fig.I.5. Darrieus patent in 1931: (a) curved blades and (b) straight blades	7
Fig.I.6. Timeline of Darrieus VAWT development.....	8
Fig.I.7. Egg-beater type Darrieus wind turbine	9
Fig.I.8. (a) Straight bladed type Darrieus wind turbine (b) Variable geometry oval trajectory (VGOT) Darrieus turbine	9
Fig.I.9. Darrieus–Masgrows (two-tier) rotor	10
Fig.I.10. Crossflex wind turbine	11
Fig.I.11. Two leaf semi rotary VAWT	12
Fig.I.12. Savonius rotor	13
Fig.I.13. Combined Savonius and Darrieus rotor	14
Fig.I.14. Sistan type wind mill.....	14
Fig.I.15. Types of support structures for curved- and straight-blades Darrieus VAWTs.....	15
Fig.I.16. Major components in HAWT system.....	16
Fig.I.17. Comparison among different turbine efficiency's	16
Fig.I.18. 2D cross section from the turbine	17
Fig.I.19. Airfoil terminology	18
Fig.I.20. Drag and lift forces presentation.	19
Fig.I.21. Various parts of pressure distribution	21
Fig.I.22: (a) Attached flow (b) Leading-edge stall (c) Trailing-edge stall.....	22
Fig.I.23. Lift behavior for different stall types	23
Fig.I.24. Lift, moment, and drag coefficients under static and dynamic stall	24
Fig.I.25. Variation of AoA versus azimuthal positions	25
Fig.I.26. Visualization of dynamic stall at $\lambda = 2.14$, [36]	26
Fig.I.27. Flow visualization at four different positions, [37]	27

Fig.I.28. Schematic illustration of the dynamic stall for different λ , [37]	28
Fig.I.29. Engineering goals and corresponding flow changes	28
Fig.I.30. Interrelationships between the different control objectives	30
Fig.I.31. Classification of flow-control strategies	30
Fig.I.32. Various rotating cylinder configuration used to increase lift and delay stall of an airfoil	31
Fig.I.33. Tractor-trailer truck with rotating cylinders.....	32
Fig.I.34. Schematic of porous airfoil for suction.	32
Fig.I.35. An oscillating symmetric foil placed in the wake of a cylinder oscillating transversely.....	33
Fig.I.36. Schematic showing experimental set-up for a backward facing step flow	34
Fig.I.37. Effect of small flapping wing on laminar boundary layer over a flat plat	34
Fig.I.38. Flow separation control around a large stationary wing by mean of flapping wing.	34
Fig.I.39. Stall suppression due to flow entrainment	35
Fig.I.40. Cylinder–Undulation(flexible) foil system	35
Fig.I.41. Plunge and deflection motion of single flexible airfoil	36

Chapter II: Numerical Methodology

Fig.II.1. Subdivisions of the Near-Wall region	43
Fig.II.2. Near-Wall treatments in ANSYS Fluent	43
Fig.II.3. Photographs for the VATT models over one revolution.	44
Fig.II.4. Model geometrical characteristic.....	46
Fig.II.5. Schematic diagram for the instantaneous airfoil position.....	47
Fig.II.6. Illustration of the position axles of the two flapping foils in one revolution	47
Fig.II.7. Computational domain dimension and the boundary conditions	48
Fig.II.8. Diagram for unsteady time step.	49
Fig.II.9. a: The different meshing zones of the proposed model b: Zooming scale of the meshing around a blade and wings set	50
Fig.II.10. Technique of sliding mesh between zone2 and zone 3.....	51
Fig.II.11. Deforming mesh between zone2, zone 3 and zone 4.....	51
Fig.II.12. Zones created by non-periodic interface intersection.....	52
Fig.II.13. Two-dimensional grid interface.....	53

Fig.II.14. Illustration of the layering technique allowing the sliding of zone 3 in zone 2 (zone 3 is secured on the foil).	53
Fig.II.15. Dynamic layering method	53
Fig.II.16. Model geometrical characteristics (T: turbine revolution t: time)	56
Fig.II.17. Schematic diagram of the deforming turbine blade a) flexible trailing edge b) camber deformation	57
Fig.II.18. Flexible airfoil deformation for ($z_i=4$)	57
Fig.II.19. Flexure motion trajectory for $z_i=8$	57
Fig.II.20. Simulation domain zones.....	58
Fig.II.21. Zooming scale of the mesh around the flexible blade	58
Fig.II.22. Dynamic remeshing method.....	59

Chapter III: Results and Discussion

Fig.III.1. Flow field around blade in one revolution	61
Fig.III.2. Flow incidence α° versus the blade position θ° for several tip speed ratios λ	63
Fig.III.3. Instantaneous drag coefficients against the incidence angle α°	63
Fig.III.4. Instantaneous lift coefficients against the incidence angle α°	64
Fig.III.5. Downstream wakes contours at $\lambda = 1.4$	64
Fig.III.6. Pressure contours at $\lambda = 1.4$	64
Fig.III.7. Plunge and deflection motion of single flexible airfoil.	65
Fig.III.8. Validation of computational model, compared to publish results	66
Fig.III.9. Instantaneous momentum coefficient for several grids	66
Fig.III.10. Comparison of (a) instantaneous moment coefficients and (b) instantaneous blade lift and drag coefficients against time for different blade turbines.....	67
Fig.III.11. Comparison of blade surface pressure coefficient distributions at $\lambda = 1.4$ with $a_0/c=0.1$ $z_i=2$	68
Fig.III.12. Comparison of instantaneous vortex contours at $\lambda = 1.4$ with $a_0/c=0.1$ $z_i=2$	68
Fig.III.13. Comparison of downstream wakes contours at $\lambda = 1.4$ with $a_0/c=0.1$ $z_i=2$	68
Fig.III.14. Instantaneous momentum coefficient for different blade turbines	69
Fig.III.15. Comparison of instantaneous vortex contours at $\lambda = 1.4$ with $a_0/c=0.1$ $z_i=2$	69
Fig.III.16. (a) Instantaneous blade moment coefficient versus θ .(b) Instantaneous power coefficient .(c) Instantaneous lift coefficient .(d) Instantaneous drag coefficient	70

Fig.III.17. (a) Time-averaged power coefficient versus λ .(b) Time-averaged input power coefficient versus λ	71
Fig.III.18. Time-averaged efficiency coefficient versus λ	71
Fig.III.19. Comparison of instantaneous vortex contours at $\lambda = 1.4$ with $a_0/c=0.1$	72
Fig.III.20. (a) Instantaneous blade moment coefficient versus θ (b) Instantaneous power coefficient (c) Instantaneous lift coefficient (d) Instantaneous drag coefficient	73
Fig.III.21. (a) Time-averaged power coefficient versus λ .(b) Time-averaged input power coefficient versus λ	74
Fig.III.22. Time-averaged efficiency coefficient versus λ	74
Fig.III.23. Comparison of instantaneous vortex contours at $\lambda = 1.4$	75
Fig.III.23. Photographs for the flexible airfoils shapes at $\theta = 100^\circ$	75
Fig.III.24. Instantaneous power coefficients for different airfoils	76
Fig.III.25. Gain in power coefficients for different airfoils	77
Fig.III.26. Comparison among instantaneous vortex contours.	78
Fig.III.27. Pressure contour for different blade turbines	79
Fig.III.28. Effect of flexible coefficient n on the blade shape	79
Fig.III.29. Effect of flexible coefficient n on the (a) Instantaneous moment coefficients and (b) Instantaneous power coefficients (NACA0024).	80
Fig.III.30. Schematic diagram of the deforming turbine blade	80
Fig.III.31. Effect of flexible coefficient Lc on the (a) Instantaneous moment coefficients and (b) Instantaneous power coefficients (NACA0024, $\lambda = 0.7$)	81
Fig.III.32. Comparison between blade surface pressure distributions.....	82
Fig.III.33. Comparison of (a) Instantaneous moment coefficients and (b) Instantaneous blade lift and drag coefficients against time for different blade turbines.....	83
Fig.III.34. Downstream wakes contours for both cases (a) original and (b) flexible configuration	83
Fig.III.35. (a) Instantaneous blade moment coefficient versus θ .(b) Instantaneous power coefficient .(c) Instantaneous lift coefficient .(d) Instantaneous drag coefficient	84
Fig.III.36. a) Time-averaged power coefficient versus λ .(b) Time-averaged input power coefficient versus λ	85
Fig.III.37. Time-averaged efficiency coefficient versus λ	86
Fig.III.38. (a) Instantaneous blade moment coefficient versus θ .(b) Instantaneous power coefficient .(c) Instantaneous lift coefficient .(d) Instantaneous drag coefficient	86
Fig.III.39. (a) Time-averaged power coefficient versus λ .(b) Time-averaged input power coefficient versus λ	87
Fig.III.40. Time-averaged efficiency coefficient versus λ	87

Fig.III.41. (a) Two flapping wings associated to the main blade of the turbine. (b) Slotted blade with oscillating flap [30].	87
Fig.III.42. Instantaneous Z-Vorticity contours and the generated wakes for different azimuthal positions ($\lambda=2.2$, $z_i=40$)	88
Fig.III.43. The vortex tails extend in the downstream wake; in the right side without control, and in the left side with flapping wings.	88
Fig.III.44. Comparison between blade surface pressure distributions	90
Fig.III.45. (a) Instantaneous power coefficient .(b) Instantaneous lift coefficient .(c) Instantaneous drag coefficient	91

List of tables

Table II.1. Main geometrical features of the flapping foils model	37
Table II.2. Main geometrical features of the flexible turbine model	44
Table II.3. Dynamic mesh parameters	46

List of symbols

Indices:

∞ : Infinite

Symbols

C : Blade Cord (m)

C_l : Lift coefficient

C_d : Drag coefficient

C_s : Constant of Smagorinsky

c_w : Constant of WALE model

C_f : Friction coefficient

C_p : Pressure coefficient

f : Frequency (Hz)

z_i : Frequency controlled parameter relative to turbine diameters

Re : Reynolds number

R_{turb} : Reynolds turbulent number

St : Strouhal number

t : Time (s)

u : Velocity component along the x axis (m/s)

U_∞ : Incoming flow velocity (m/s)

v : Velocity component along the x axis (m/s)

ν : Viscosity (kg/m.s)

y^+ : Non dimensional wall distance

α : incidence Angle ($^\circ$)

Δt : Step time (s)

ρ : Fluid density (kg/m³)

δ_{ij} : Constraints

τ_{ij} : Turbulent Constraints

μ_T : Turbulent viscosity (m²/s)

LIST OF ABBREVIATION

AOA: Angle of attack;

B.L: Boundary layer;

DNS: Direct Numerical Simulation;

F.M: Flapping motion;

L.E: Leading edge;

LEV: Leading edge vortex;

LES: Large Eddy Simulation;

N.S: Navier-Stokes;

RANS: Reynolds Average Navier-Stokes;

T.E: Trailing edge;

TEV: Trailing edge vortex;

UDF: User Defined Function;

GENERAL INTRODUCTION

In recent years, the demand for energy over the world increases dramatically, which exhausts the available fossil energy sources. This imbalance has stimulated many countries to search for an alternative energy sources. In this framework, renewable energies are the most desired sources that can cover continuously the world's growing resource demands. They are considered also as environmentally friendly sources as compared to fossil energy sources.

Many countries aim to make renewable energies as the source of the largest portion of their energy requirements. Several of incentives are imposed to force the world moving toward clean and renewable energies.

The European Parliament climate and energy package law is employed since June 2009. This law involves firstly, that by the year 2020; at least 20% of the European Union's energy consumption should be provided by renewable resources. Secondly, the ratio of greenhouse gas emissions should be reduced at least by 20% from 1990 levels [1].

European Union leaders propose a chart to reduce the global greenhouse gas emitting, which consists in obliging the energy consuming countries to respect a given ratio of reduction in proportion to their gas emission ratio. In order to meet these environmental standards, research into renewable energy technologies must be followed.

Typically, the world resource reserves decline proportional to the energy demand, much research is devoted to finding practical energy alternatives.

Wind energy has appeared as one of the most used new energy sources, while other sources - except solar energy- are less investigated. Newly, the research moves toward the kinetic energy of water currents in oceans, due to the fact that it is environmentally benign. This source has been accepted as a renewable and clean energy. Additionally, contrasting many other renewable resources, tidal energy is also very foreseeable. The world extracts from this source approximately 3 *TW* with 1 *TW* in accessible areas for the installation of energy extracting devices [2].

Currently, the flow control is one of the major challenges in hydro/aerodynamics sector. Indeed, whether for automotive or aerospace applications, the goal is to develop engineering applications that satisfy many economic and technological constraints.

In this context, the issue is the ability to manipulate a flow to eliminate or minimize the negative effects such as drag and noise and to enhance the positive effects such as the lift or turbulence for increased mixing characteristic. For over a century, the dynamic stall phenomenon was intensely studied; in fact, it is responsible for the structural vibration and aero-acoustics noises which are harmful factors for many industrial applications. This flow separation caused by an adverse pressure gradient, or by a geometric rupture, is accompanied by a huge deterioration in the aerodynamic performance. To improve the performance of such applications, and approach the optimal operation condition, it is important to correctly predict the mechanisms that accompany this stall such as the transition of the flow and the turbulent agitation, to choose the appropriate flow control strategy.

Various methods are available to control the flow separation, they can be classified into two categories namely: passive methods which consist in performing a slight modification in the system geometry to manipulate the flow field without using an external energy and active methods consist in introducing, an amount of energy from the outside environment (generally in the form of momentum). Interesting active methods which are relevant to animal propulsion and maneuverability features are the Bio inspired flow control techniques, they have a grown interest in many areas, but there are no rules to determine their effects on a system other than a wide parametric study. In fact, the effectiveness of these techniques depends on many parameters such as: geometry, frequency and location. Their utilization systematically requires a large parametric study which doesn't ensures, however, that the optimal operation is reached.

In recent decades, the growth of computing capabilities has allowed the development of a new branch of numerical methods called the Computational Fluid Dynamics (CFD). This tool is used to develop and test new concepts, while avoiding the constraints of time and finance that are required in the experimental tests.

This thesis is divided into three chapters:

The thesis is initiated by a bibliographic review on the different types of vertical axis wind turbines. The review also draws a detailed analysis of the vertical axis wind turbine conception with its operating principle and the associated parameters. Then it recorded the various flow separation control techniques.

The second chapter is devoted to explain the turbulence modeling and numerical approaches used to solve the Navier-Stokes equations. General descriptions of the CFD methods and the suggested vertical axis wind turbines VAWT's models including their constituents and their dimensions are provided. Next, a discussion about the flapping-wings motion and their control parameters is carried out. Two approaches of flow control are investigated, flow control by using backward flapping wings and flow control by the means of flapping flexible wings.

The third chapter addresses firstly, the flow over a rigid vertical axis wind turbine, in order to understand the phenomena occurring during the turbine stall. This case is used as a comparison reference for the different results obtained in this study.

This chapter shows the results obtained accompanied with the necessary commentaries for their interpretations. It is divided into three parts. In the first, we interesting in the effect of a simple flexible blade on the performance of a VAWT. The conception is inspired from the vortex control mechanism utilized by the aero-aqua animals to improve their performance via the flexion of their fins. The second part is related also to flexible blades, in which a camber deformation is applied instead of a simple deflection. The third part proposes a dynamic control device which consists in the association to each turbine blade, a couple of flapping wings, in biplane configuration. Then a comparison among the three tested flow control techniques is carried out.

The thesis is finalized with an overall conclusion and recommended perspectives as an extension to the present work.

CH I. LITERATURE REVIEW

I.1. Introduction

This chapter proposes in the first section, a global vision about the technology of wind energy conversion including the different types of wind turbines. It also draws detailed examinations of the vertical axis wind turbine conception with its operating principle and the associated parameters. A bibliographic review on the different physical phenomena occurring during the turbine stall is delivered.

The second section provides a summary about the flow control techniques and their classification.

I.2. Renewable energies

Renewable energy sources involve natural phenomena that are inexhaustible such as sunlight, wind, tides and geothermal heat (Fig.I.1). Solar and wind power are the most used sources among the various sources of renewable energy. In addition to their environmentally friendly, the two kinds of alternative sources are expected to generate the most of the world's electricity within the next 50 years.

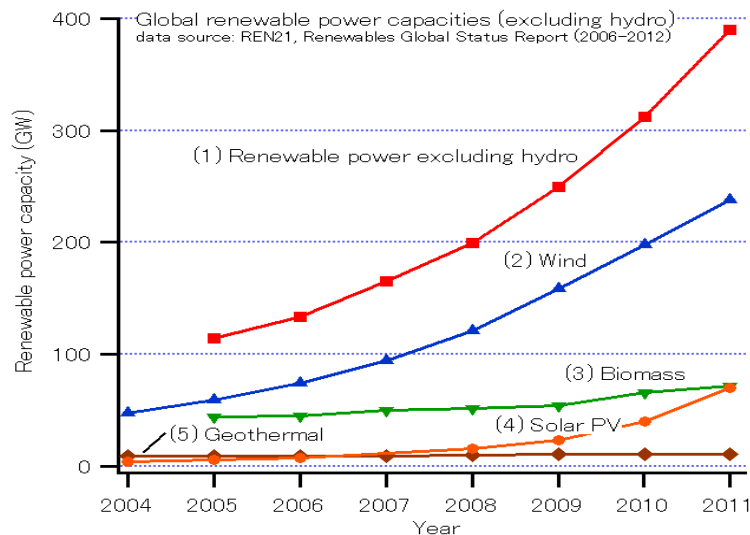


Fig.I.1.Global renewable power capacity excluding hydro energy [2]

I.2.1.Wind energy

Wind energy has the potential to cover the increasing power request of the entire world if it is exploited effectively. It will be the most common renewable energy source; due to its accessibility. As an environmentally friendly and clean source, wind is furthermore receiving

importance in energy policy. There are certain factors that obstruct the development of this technology like its lower efficiency and high installation cost. Nonetheless the high cost could be lowered if we move toward small scale turbines that can be constructed and installed easily anywhere.

I.2.2.Wind energy utilization

In reality, a small part of the world electricity consumption is currently provided by the wind sources. In fact, it is presently less than 4.5% of world electricity consumption [1].

Nevertheless, it still has a growing interest and its contribution in electricity generation increasing quickly but, it will still generate insufficient portions of world electricity requirements by 2030. Increasing concern about the lack of resources, and the inability to cover the increasing demand of energy, also the concern about the serious global climate change makes it imperative for the world to find viable energy alternatives. Extracting energy from certain of the renewable energies may not be practicable or sustainable, some are local and limited. So solar and wind are the only sources that can be advantageous.

The World and European Wind Energy Associations, outlined that the connected global wind capacity reached 158.9 Giga-watts by the end of 2010 (Fig.I.2), a portion of 3,000 MW is located offshore. World wind power generation capacity in 2011 reached 238.4 GW, which is 33% higher than the previous two years.

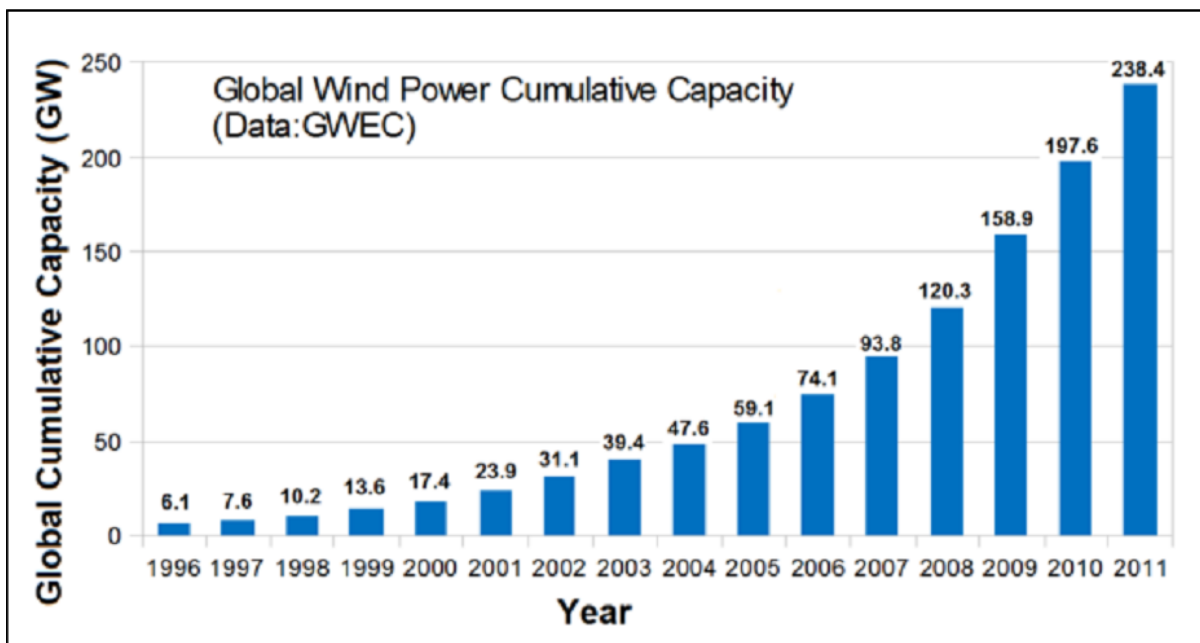


Fig.I.2 Global cumulative capacity of wind energy [3]

In United States of America, renewable energy sources provided about 12% of its total electricity generation in 2013. The hydroelectric power (30%) ranks first, followed by biomass (25%) and wind (19%) [3]. According to U.S. energy reports, US wind power generation capacity in 2005 was 2.5 GW; it had grown to 13 GW by 2012 (Fig.I.3).

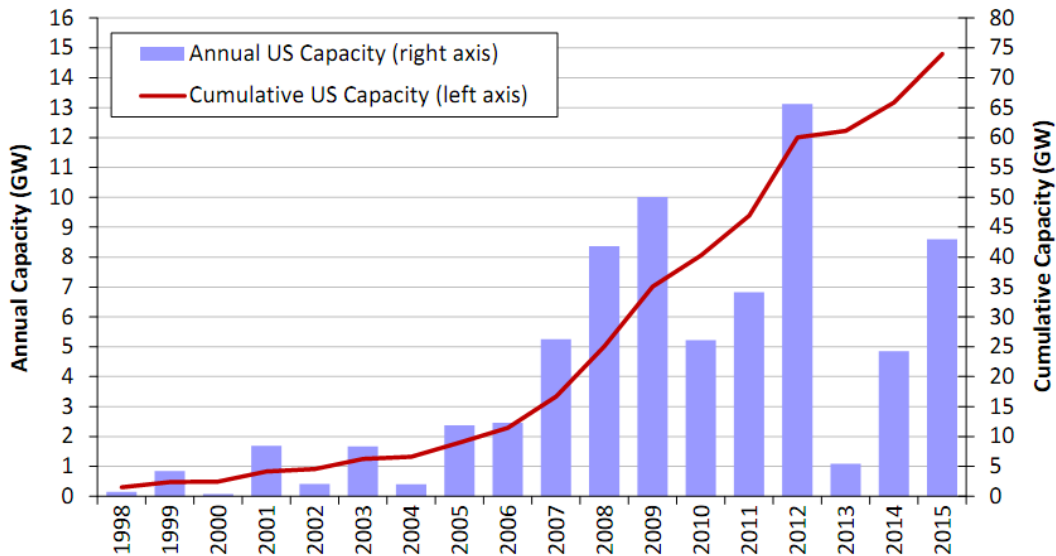


Fig.I.3. Annual and cumulative growth in U.S. wind power capacity [3]

Expected and Actual Installation of Wind Energy by U.S. Department of Energy (DOE), China has the highest capacity in wind energy generation (Fig.I.4), followed by the United States, Germany and Spain [3].

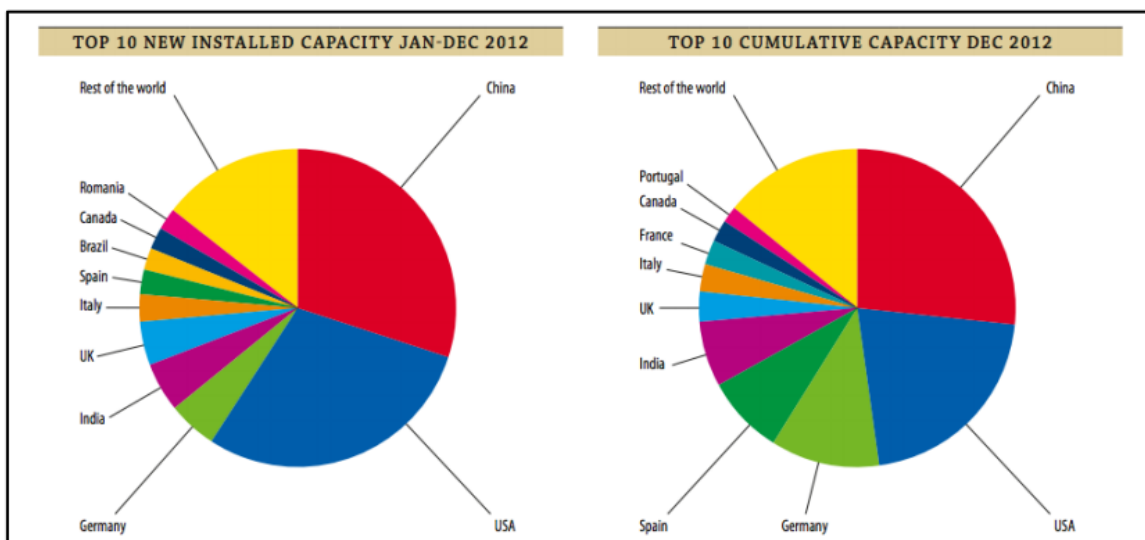


Fig.I.4 Wind energy generation capacity by country [3]

I.3. Vertical axis wind turbines (VAWT)

The first design was proposed in 1925 by the French engineer Darrieus and patented officially in 1931 [4]. It was considered as a promising concept for modern wind turbines. This type of turbines is composed of blades driven by the lifting forces. The axis of rotation is perpendicular to the incident flow (Fig. I.5). In Darrieus patent two configurations: curved and straight blades were exposed.

This type of turbines is less likely than the horizontal turbines type. The advantage of VAWT is the insensitivity to the flow direction. Which means it doesn't require the orientation according to the flow direction; another advantage is the possibility to stack several turbines on a common axis of rotation with the same generator. As for the HAWT, the rotational velocity is controlled according to the incoming flow velocity.

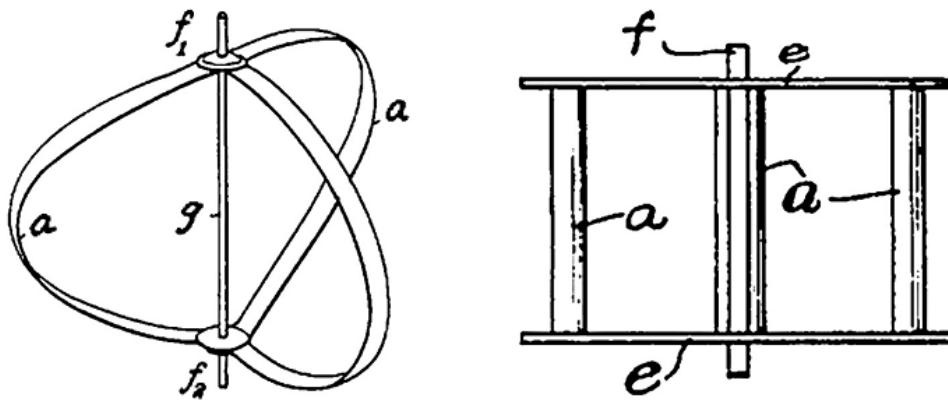


Fig.I.5. Darrieus patent in 1931: (a) curved blades and (b) straight blades. [5]

From the first concept proposed by Darrieus, several variations for both, the curved and straight-blades configurations have been developed as shown in Fig.I.6. There are several variations of the curved configuration such as guy-wired, fixed on tower and cantilevered versions and for the straight-blades one, there are: diamond, V/Y and delta (D). Details on the topic are available in the following sections.

I.4. Different types of VAWT

Several innovative vertical axis wind turbines designs were developed and succeeded in the use of aerodynamic lift. For the currently available designs, there are some problems that obstruct the optimum harvesting of energy, including low starting torque, low blade lift forces and low efficiency. This fact, still stimulates the engineers to coming up with many new and innovative designs to resolve these problems associated with VAWTs. A detailed review of VAWT configurations available till now is presented in this section.

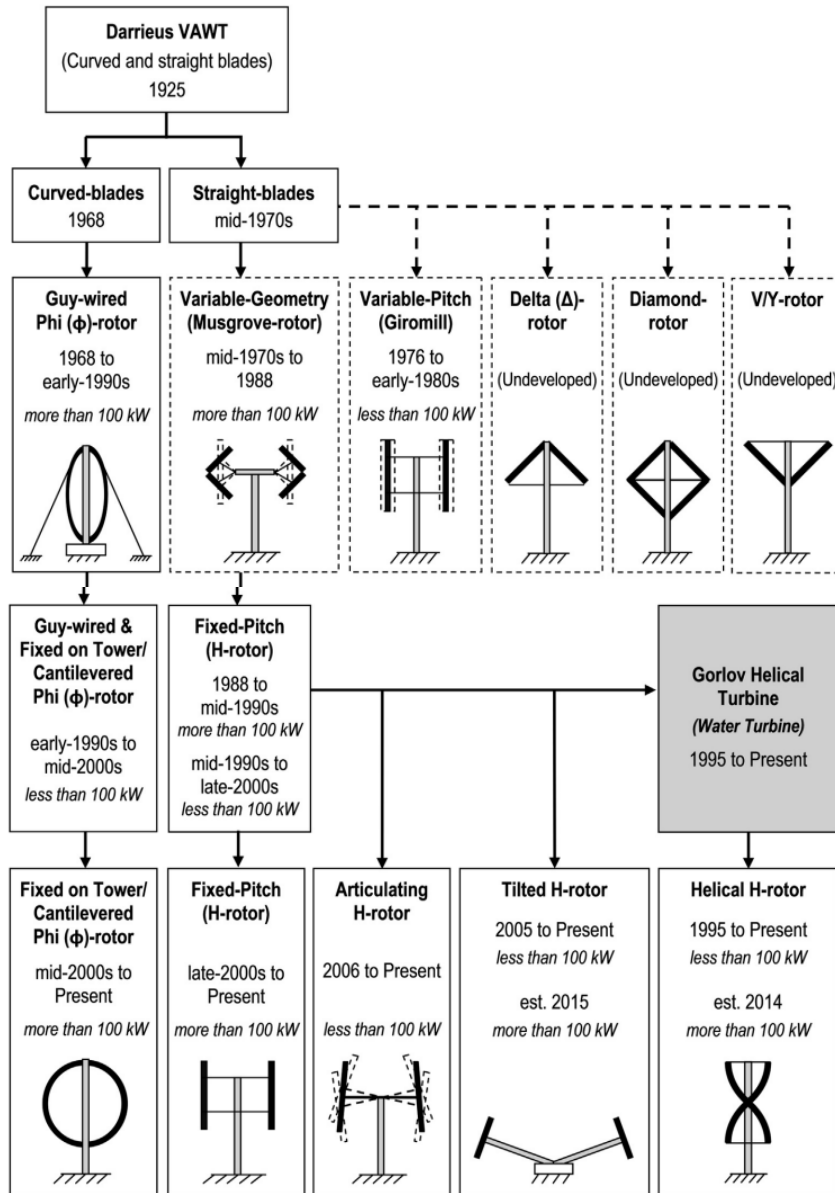


Fig.I.6. Timeline of Darrieus VAWT development [5]

I.4.1 Egg-beater type Darrieus wind turbine

This type is known by its blades that are set as arms of an egg-beater as depicted in Fig.I.7. The flow around the blades is basically unsteady. The egg-beater type geometry ensures a minimum bending stresses in the blades [5]. Due to its mechanical reliability and high coefficient of performance, commercial turbines of 3.8 MW have been realized in Canada [6]. This project is among the first investments to produce energy at large scale. However, the high costs of manufacturing such complex geometry of blades have limited the turbines production at commercial scale.

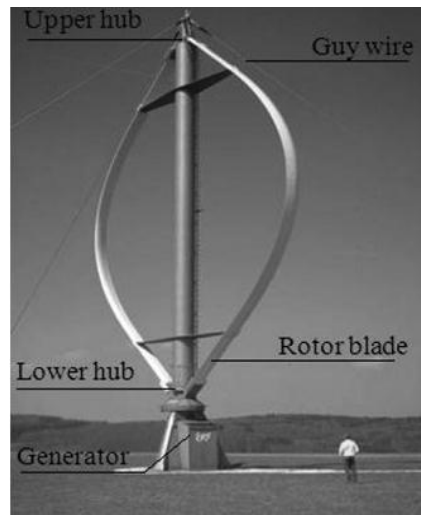


Fig.I.7. Egg-beater type Darrieus wind turbine [7].

I.4.2 Straight bladed type Darrieus wind turbine

These types of turbines have the highest values of efficiency as compared to other types of VAWTs .But suffer from problems of low starting torque. These types have straight blades having airfoil cross section, they are also known as Giromill wind turbines (see Fig.I.8(a)). From commercial point of view, the commercial VAWTs have a number of blades that increases from one to five. However, two and three bladed configurations are the most used. Two blades turbines are frequently known as H-rotor [8, 9].

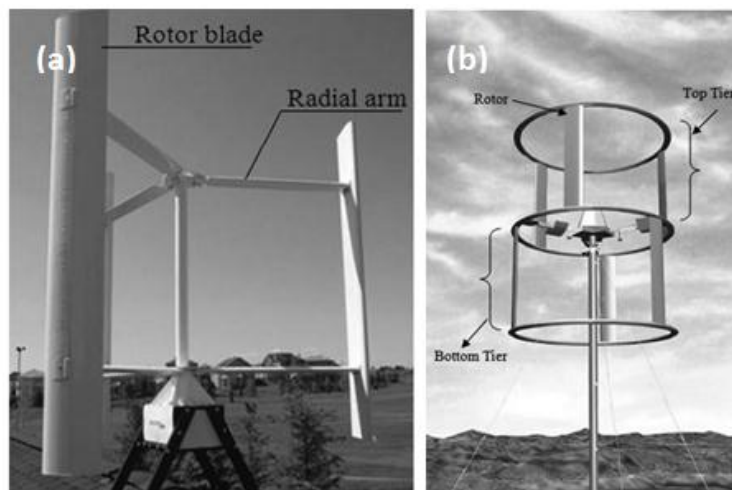


Fig.I.8. (a) Straight bladed type Darrieus wind turbine (b) Variable geometry oval trajectory (VGOT) Darrieus turbine [10, 11].

I.4.3 Variable geometry oval trajectory (VGOT) Darrieus turbine

Typically, Darrieus rotor is characterized by low tip speed ratios, which obstruct the use at very large scale. To cover this gap, Ponta et al. [12] proposed a model that can generate power at large scale. The proposed concept consists in blades that move on rails, on an elevated rail track instead of rotating around a central rotor. The blades have wheels fixed in the base and coupled with electrical systems to generate electricity. The innovative design ensures the generation of power at large scale through vertical axis wind turbines (see Fig.I.8(b)). It provides a high efficiency (about 57% for the optimum design configurations) and improves structural stability and eliminates the issues of low starting torque. Ponta et al. [12] suggested numerical models for the analysis of VGOT Darrieus turbine. To evaluate the performance of this configuration, three dimensionless constants known as: equivalent power coefficient, equivalent solidity coefficient and trajectory efficiency were introduced. The power coefficient (CP) is estimated for different number of blades 'N'. The results indicated that the turbine with higher number of blades ($N = 120-160$) has good efficiency at low tip speed ratio (~ 2) while at higher TSR, a number of blades between $N = 60$ and 80, provides improved efficiency.

I.4.4 Darrieus–Masgrowe (two-tier) rotor

This configuration was proposed by Gorelov and Krivospitsky [10]. It named Darrieus–Masgrowe rotor (Fig.I.9). The turbine consists of two tiers having two or three blades in each tier. The new configuration has the same mechanism of energy harvesting as other Darrieus rotors.



Fig.I.9. Darrieus–Masgrowe (two-tier) rotor [13]

By the same mechanism as a variable pitch rotor, the two-tier configuration enhances the turbine capability to self-start at wind velocity as low as 1.6–2 m/s with efficiency of 39–40% Gorelov and Krivospitsky [10] outlined that the turbine indicated self-start with blades having large width. Additional studies are necessary to verify the feasibility of this configuration for large scale applications.

I.4.5 Crossflex wind turbine

From point of view of architectural aesthetics, the use of all earlier configurations of VAWT is not appropriate. Moreover their use on high rise buildings is limited by the structural design requirements. Sharpe and Proven [14] offered a model named Crossflex wind turbine as “true building integrated wind turbine”. The previously familiarized concept of Darrieus wind turbine is used in an innovative configuration. The conventional Darrieus type turbine is fixed within a frame and several such units are typically combined together. Crossflex turbine installed on a building is shown in Fig.I.10. Sharpe and Proven [14] drawn that the efficiency of the turbine was improved by using “low inertial mass design”. The bending stresses also can be reduced by using flexible blades. The turbines are fixed to a strong support which leads to lower vibrations. As the case with other VAWTs, the turbine energy extraction efficiency is not affected by the wind directions. This simplicity allows the installation of these turbines at various locations on a building which leads to greater installed ability per building, for example, it can be fixed at all walls and corners.

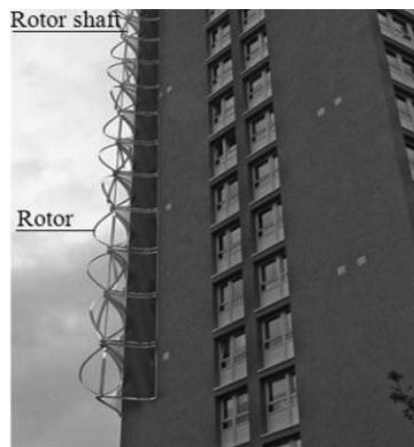


Fig.I.10. Crossflex wind turbine. [14]

This type of turbines has already been tested at Newberry tower in Glasgow, Scotland. Sharpe and Proven [14] drawn that this type of turbine is appropriate only in the areas where the wind velocity surpass 14 m/s. which suggest that the turbine can only be used in high rise building;

furthermore, this configuration is not applicable in wind farm arrangements due to low free stream velocity.

I.4.6 Two leaf semi rotary VAWT

Zhang et al. [15] proposed two leaf semi-rotary VAWT with two blades at an angle of 90° . An illustrative image is shown in Fig.I.11. This turbine is characterized by a higher wind energy extraction coefficient, the variable pitch blades improves the turbine self-starting capabilities. Advantages such as simple construction, ease of installation and maintenance make it more suitable for difficult terrain [15]. The turbine suffers from structural vibration of the blades of large sized models and at high wind speeds.

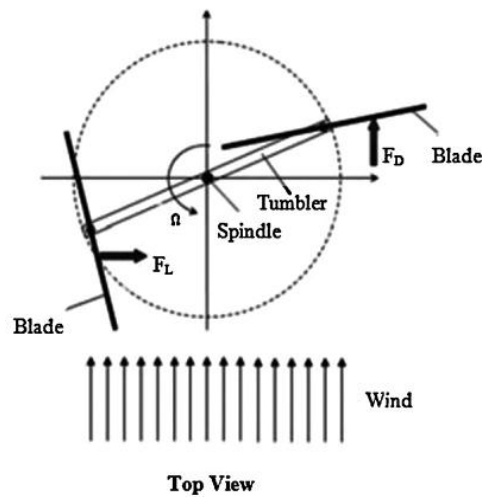


Fig.I.11. Two leaf semi rotary VAWT [15]

I.4.7 Savonius rotor

This type is classified in the drag driven turbines type, in which the movement is created by the drag force (Fig.I.12). A first technology based on the principle of the wheels of Grinder driven by water: the drag affecting the submerged blade is greater than that affecting the blade out of the water, which creates a torque and rotates the wheel. This principle is the oldest used one but it is not the most efficient to maximize the harvested energy.

In the case of Savonius turbines types, the rotation is created by two (or more) half cylindrical buckets slightly skewed. Because of its concave surface the drag affecting the bucket coming down the wind is greater than that affecting the bucket which rises, thus creating a torque. The rotation starts at low speed with a high torque that varies sinusoidal during the rotation. However, the performances of this type of machine are quite low in practice. Generally, these machines are not ideal for high power wind farms because the ratio of installed capacity and the useful area. The advantages of the Savonius turbine are: robustness, insensitivity to

orientation and self-starting at low incoming flow velocity compared to other ‘Lift type’ VAWTs [16]. The use of such type of turbines in commercial scale requires an efficient designs. Mohamed et al. [16] provided research that deals with the design optimization of Savonius rotor with the objective to commercialize this turbine type. They use an obstacle in a Savonius rotor to improve the efficiency of the rotor. The higher value of power coefficient was 0.3. Furthermore, the shape of the rotor was optimized and the power coefficient was rising about 30% in the total operating range [16]. The authors carried that the realizable $k-\epsilon$ model are in good agreement with the experimental results.

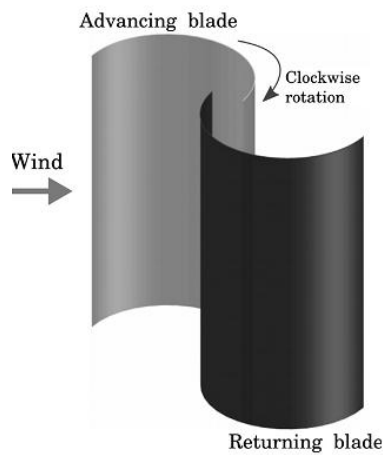


Fig.I.12. Savonius rotor [17]

I.4.8 Combined Savonius and Darrieus rotor

To take advantages of both Savonius and Darrieus rotor's, a new combined configuration is developed. Savonius rotor provides high value of starting torque while Darrieus rotor offers a low value. From efficiency stand point, Darrieus rotor is more effective than Savonius rotor [18]. Several authors have investigated the combined Savonius and Darrieus rotor (Gavalda et al. [18], Gupta and Biswas [19] and Debnath et al. [20]). It was shown that the power coefficient can surpass the barrier of 0.35 for different combination [20]. Furthermore, the new configuration (Fig.I.13) ensures a high torque coefficient which interpreted by the ability to self-start at low wind velocity. Further investigations are absolutely required to confirm the validity of these results for large scale commercial applications. The variation of power coefficient (CP) against tip speed ratio (TSR) was carried out by Debnath et al. [20]. It was detected that for $TSR > 0.36$ the CP was increased to 0.33. Wakui et al. [21] investigated the generator systems of this type of turbine through simulations and concluded that a custom system should be considered to ensemble each turbine configuration.

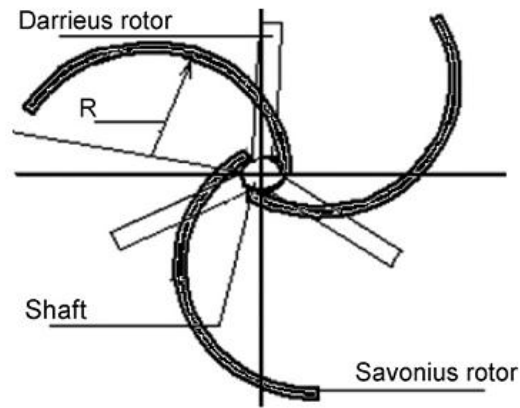


Fig.I.13. Combined Savonius and Darrieus rotor [18]

I.4.9 Sistan type wind mill

The Sistan wind turbine is a drag force driven turbine. Muller et al. [22] have studied the aerodynamic behavior of these turbines. An illustrative image of this model is shown in Fig.I.14. These turbines can easily building which increases the possibility of commercialization. Muller et al. [22] have improved the traditional turbine designs efficiency about 30% by adding disks at top and bottom of the rotor. Also, it is advised that an increase in the turbine blades from 4 to 6 can increase the efficiency by 6 to 7%. The ability to self-start is typically present in fact the turbine is a drag type wind turbine. Further research is necessary in the field to properly identify the optimum configurations for the turbine.

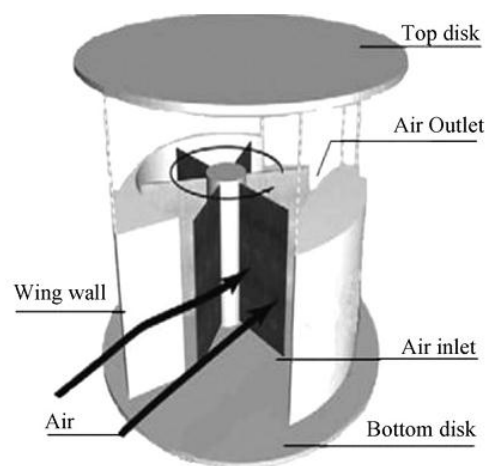


Fig.I.14. Sistan type wind mill [21]

I.5. Types of support structures for curved- and straight-blades Darrieus VAWTs.

Actually, there is no specific support structure for the vertical axis turbines. Nevertheless, curved-blades configuration with cable or guywires support has been intensely investigated in

the US and Canada. However, different forms of supports have been realized for both curved and straight blades VAWTs, as depicted in Fig.I.15. the four support types that are illustrated are appropriate for both straight and curved blades configurations.

Guy wires support (A) has been extensively used for phi-rotor. This support cannot be easily installed on top of the rotor tube in straight-blades turbine without extending the rotor tube .

Otherwise, for straight blades configuration ,a combination of cantilever support and guy wires (B) is already tested. Due to the negative contribution of wire tension which increases the axial load and the vibration, the Guy wires support has been considered as not preferable [23,24].Also the use of wires to fix the turbine requires large land area.

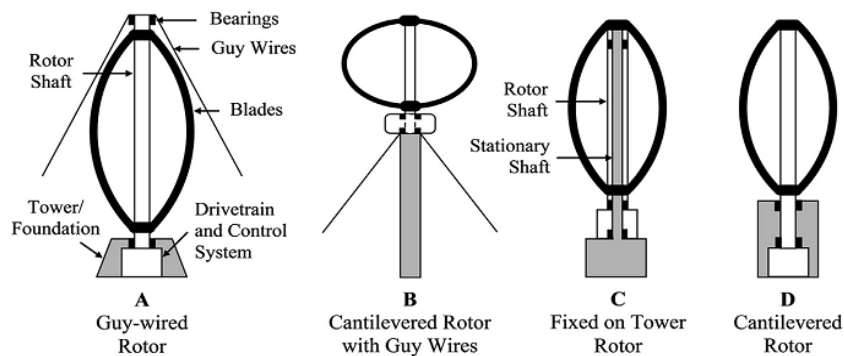


Fig.I.15. Types of support structures for curved- and straight-blades Darrieus VAWTs.[5]

In the third support type (c), the turbine blade is fixed on the tower which necessitates a specific type of generator, in fact the generator stator coils are mounted on the tower's stationary shaft, while generator rotor are fixed to the lower hub of the rotor shaft.

The Cantilevered-rotor (D) showed a great efficiency , compared to other types due to its resistivity to axial loads also to its simple manufacturing and maintenance. Among these four types, cantilevered-rotor is the most promossing model for the future of Darrieus VAWT.

I.6.Horizontal axis turbines

It is currently the most utilized turbines, it consist of helices in which their axis of rotation are parallel to the incident flow (Fig.I.16). These turbines are known also as axial flow turbines. The turbine must face the flow to achieve an optimal performance which requires a system of orientation to be positioned optimally when the current direction varying. The angular velocity of the blades is controlled to optimize the energy produced depending on the incoming flow velocity. An electric generator recovers directly the torque provided by the rotational axis of the turbine.

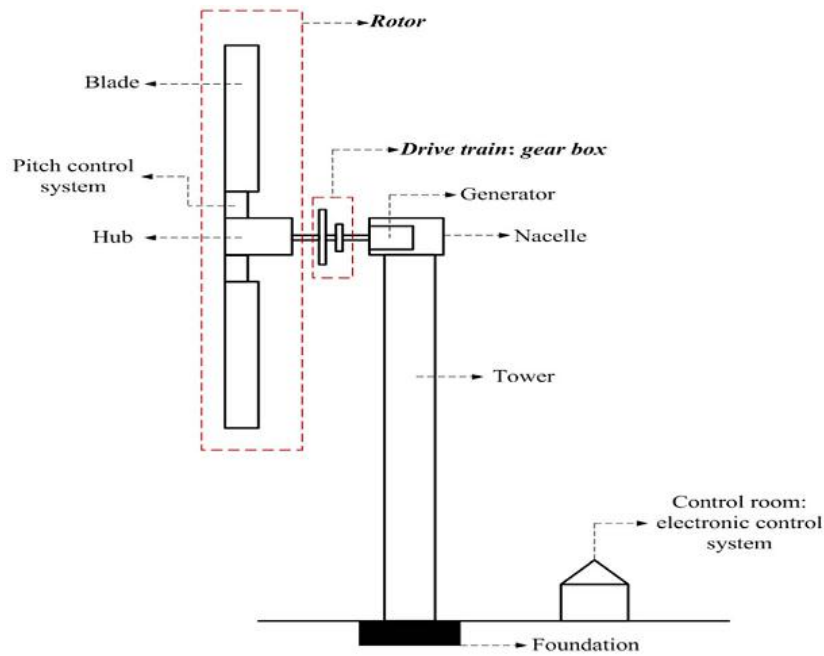


Fig.I.16. Components of HAWT system [25]

I.7. Comparison among different turbine efficiency's

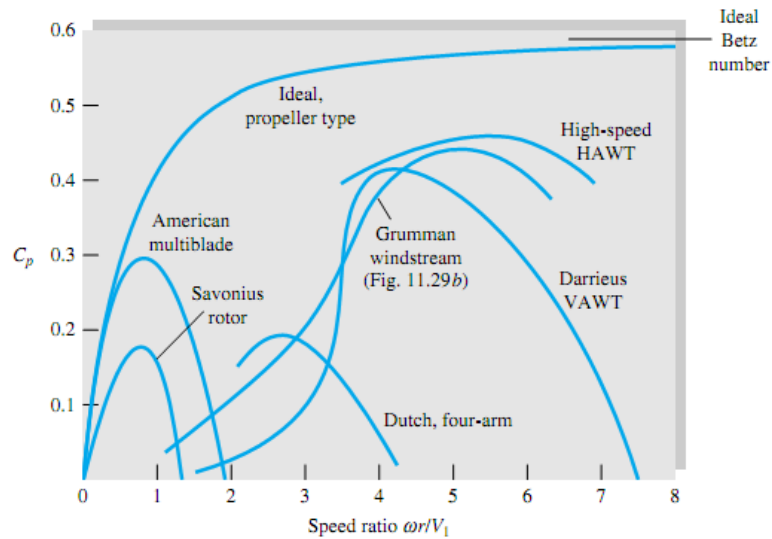


Fig.I.17. Comparison among different turbine efficiency's [26]

Fig.I.17 compares among the power coefficients of different types of wind turbines as a function of the tip speed ratio which is given as the ratio between the tangential velocity of the blade's tip and the wind velocity. Typically, the power coefficient explains why the HAWT are preferred for the electricity generation however; other parameters must be taken into account such as the building coast and the easy maintenance.

I.8.VAWT turbine parameters

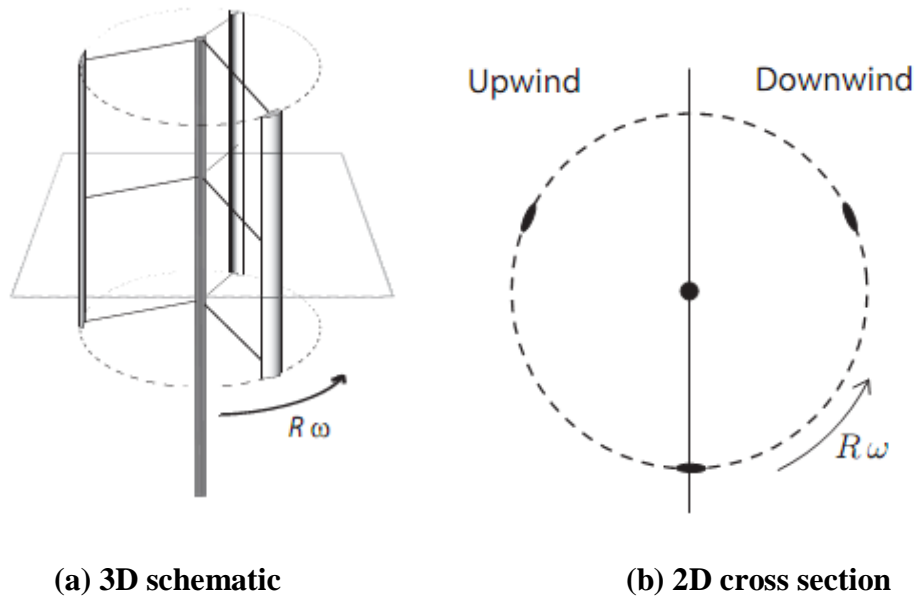


Fig.I.18. 2D cross section from the turbine

- **Tip speed ratio (λ)**

Several key points must be considered in the design of a wind turbine. The power coefficient is strongly dependent on the tip speed ratio, which is defined as the ratio between the tangential velocity of the blade's tip and the wind velocity, the flow regime is generally characterized by the tip speed ratio [26]:

$$\lambda = \frac{\omega R}{U} \quad \text{I.1}$$

Where R is the turbine radius, U represents the incoming wind velocity, ω is the turbine angular velocity

- **Reynolds number (Re):**

The Reynolds number is a non-dimensional number characterizes the ratio between the inertial and the viscous forces, it is given as:

$$Re = \frac{UL}{\nu} \quad \text{I.2}$$

With: L is the characteristic length and ν is the fluid cinematic viscosity.

For the VAWT we can distinct two Reynolds number relative to the turbine diameter

$$Re_D = \frac{UD}{\nu} \quad \text{I.3}$$

Or relative to the blade cord

$$Re_D = \frac{(\omega R)C}{\nu} = \frac{(U\lambda)C}{\nu} \quad I.4$$

- **The blade airfoil type**

The NACA 4-digit series are frequently used to create airfoils. In fact this type of airfoils has improved aerodynamic characteristics which are appropriate for the VAWT construction. For example they have a good stall characteristics and little roughness affect, relatively low drag and a high lift coefficient. A specific analytical equation is used to generate the camber (curvature) of the mean-line (geometric centerline) of the airfoil section and also the distribution of section thickness along the length of the airfoil.

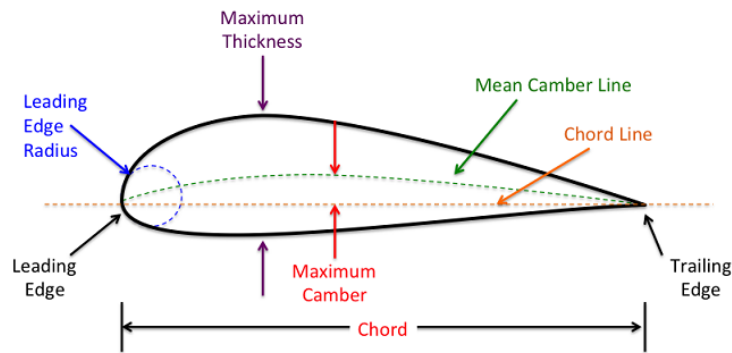


Fig.I.19. Airfoil terminology

- **Turbine solidity**

It is used to evaluate the effect of the mutual aerodynamic interactions that are due to the wakes produced by the blades. These interactions are a function of flow angle of attacks and solidity of the blades [27].

$$\sigma = \frac{nC}{2R} \quad I.5$$

- **Power coefficient (CP)**

It is well known that the available power is different from the useful power. For a VAWT having a height H, and a given number of blades, and subjected to a current of incoming wind of velocity U. Then the generated power P is [28, 29]:

$$P = \sum_i M_i \cdot \omega \quad I.6$$

Where ω is the turbine angular velocity and M_i is the blade torque relative to the turbine center.

The power coefficient CP is given by

$$CP = \frac{P}{1/2\rho U^3 D} \quad \text{I.7}$$

Where P is the generated power, ρ is the fluid density and D is the turbine diameter.

- **Moment coefficient (C_m)**

The blade's moment coefficient C_m is defined as

$$C_m = \frac{M}{1/2\rho ARU^2} \quad \text{I.8}$$

Where M present the rotor torque and A is the rotor swept area.

- **Drag and lift coefficient (CD , CL)**

Generally, the drag force is defined as the net aerodynamic force acting opposite to the flow direction and the lift force as the force that is perpendicular to the oncoming flow direction.

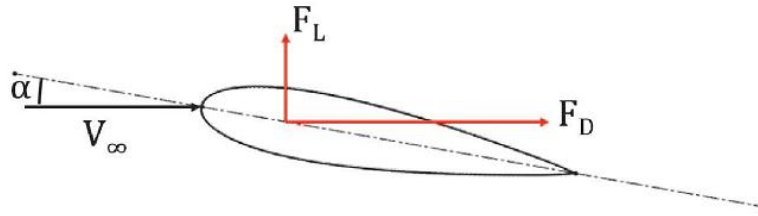


Fig.I.20. Drag and lift forces presentation.

For a vertical axis wind turbine, the lift and drag coefficients are computed respectively according to:

$$CL = C_y[\cos(\theta + \alpha)] - C_x[\sin(\theta + \alpha)] \quad \text{I.9}$$

And

$$CD = C_y[\sin(\theta + \alpha)] + C_x[\cos(\theta + \alpha)] \quad \text{I.10}$$

Where C_x and C_y are given as:

$$C_x = \frac{F_x}{1/2\rho cW^2} \quad \text{I.11}$$

And

$$C_y = \frac{F_y}{1/2\rho cW^2} \quad \text{I.12}$$

Where F_x and F_y are the forces acting along the x and y direction respectively.

The flow incidence angle α is given by

$$\alpha = \tan^{-1}\left(\frac{\sin\theta}{\cos\theta+\lambda}\right) \quad \text{I.13}$$

Where λ is the tip speed ratio.

And W is the relative wind speed given by[27]:

$$W = U\sqrt{1 + 2\lambda\cos\theta + \lambda^2} \quad \text{I.14}$$

For an actively deformable blade, the power input is computed by integrating the pressure and the viscous forces on the foil surface [30].

$$\text{Power input} = \frac{1}{T} \int_0^T \oint F(x, t) \cdot \frac{\partial h(x, t)}{\partial t} dl dt + \frac{1}{T} \int_0^T \oint F(y, t) \cdot \frac{\partial h(y, t)}{\partial t} dl dt \quad \text{I.15}$$

Where $F(x, t)$ and $F(y, t)$ are the forces components acting on the foil surface respectively in x and y directions, and dl is the elementary length along the blade surface.

The turbine efficiency is defined as:

$$\eta = \frac{CP}{CPI} \quad \text{I.16}$$

Where CPI represents the power input coefficient given as:

$$CPI = \frac{\text{Power input}}{1/2\rho U^3 c} \quad \text{I.17}$$

I.9. Dynamic stall

In order to understand clearly the mechanism of dynamic stall and before an introduction to static stall a short recall about the aerodynamic performance of airfoil sections will be providing firstly in the following section. The aerodynamic performance of an airfoil can be studied by evaluating the lift forces which is due to the difference in pressure between the upper and lower surfaces (Fig.I.21).

The pressure distribution is usually expressed in terms of pressure coefficient:

$$Cp = \frac{P - P_\infty}{1/2\rho U_\infty^2} \quad \text{I.18}$$

Cp is the ratio of the difference between local static pressure and free stream static pressure, and the free stream dynamic pressure.

The C_p starts from about 1.0 at the stagnation point near the leading edge and it increases quickly on both the upper and lower surfaces. Finally it recovers to a small positive value of C_p near the trailing edge. The pressure distribution can be divided into various parts which are :

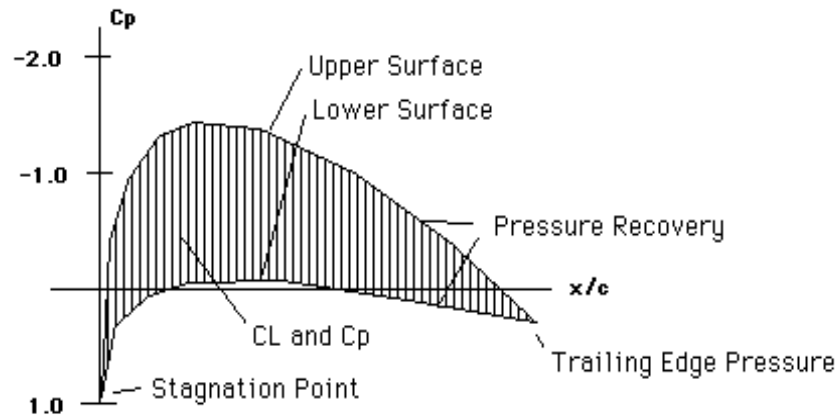


Fig.I.21. Various parts of pressure distribution

1. Upper surface: where a negative pressure occurs along the airfoil surface. **2** Lower surface: it carries a positive pressure generally, but some suctions (negative C_p) on the lower surface are present near the mid chord for particular airfoil types. **3.** Pressure recovery: the pressure increases from its minimum value to the value at the trailing edge. This area is also namely the region of adverse pressure gradient. The adverse pressure gradient is the mean raison of boundary layer separation, if the gradient is too high. **4.** Trailing edge pressure: it is affected by the airfoil thickness near the trailing edge. For thick airfoils the pressure is generally slightly positive.

I.10. Types of stall

I.10.1. Static stall

Crimi [31] carried a short introduction for static stall. The static stall phenomenon can be divided into three forms of stall: trailing edge stall, leading edge stall and thin airfoil stall. A grouping of leading and trailing edge stall is also probable. Fig. I.22 displays the flow over an airfoil in different situations. In Fig.I.22 (a) the flow is completely attached to the airfoil and no separation occurs. There is only a small laminar separation bubble near the leading edge that can form at a low incidence angle (α). Due to its small dimensions this bubble has a minor effect on the pressure distribution.

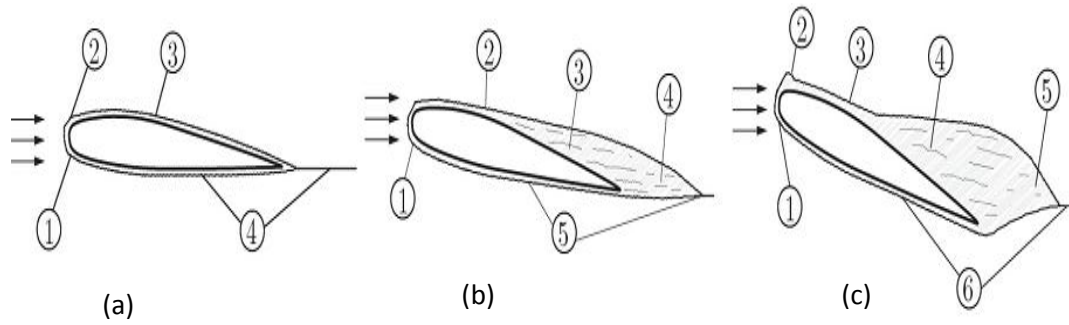


Fig.I.22: (a) Attached flow (b) Leading-edge stall (c) Trailing-edge stall [31]

At the transition point (3) the boundary layer will move toward the turbulent status, nevertheless it will re-attach to the airfoil due to an increase in energy. Typically, a vortical wake (4) will be formed. When the flow angle of attack increases, the leading edge bubble moves towards the leading edge and grows in size until its final explosion, this behavior known as leading-edge stall. It consequences a full separation interpreted by a sudden loss in lift (Fig.I.23). Finally a turbulent region (4), a straight wake (5), and shear layer are recorded.

The trailing edge stall (Fig.I.22 (b)) is a combination of the aforementioned attached flow, and the leading-edge stall mechanism. A laminar separation bubble is formed in the laminar flow case. At the transition point (2), the flow will reattach when the boundary layer became turbulent.

At a certain moment (3) the turbulent boundary layer will detached from the airfoil surface and therefore a turbulent shear layer will be formed (4), where outside this layer, the flow is considered always as a potential flow which is characterized by an irrotational velocity field. Point (5) displays the pressure recovery region and point (6) shows the formation of vortical wake.

The thin-airfoil stall is another form of stall that occurs only in thin airfoils this stall is described by a laminar separation bubble bursting at very low AoA. Similar to leading edge stall mechanism, this bubble will not move forward before bursting, but will grow progressively before the boundary layer separation. The lift is less steep, and the separation occurs earlier than in leading edge stall state.

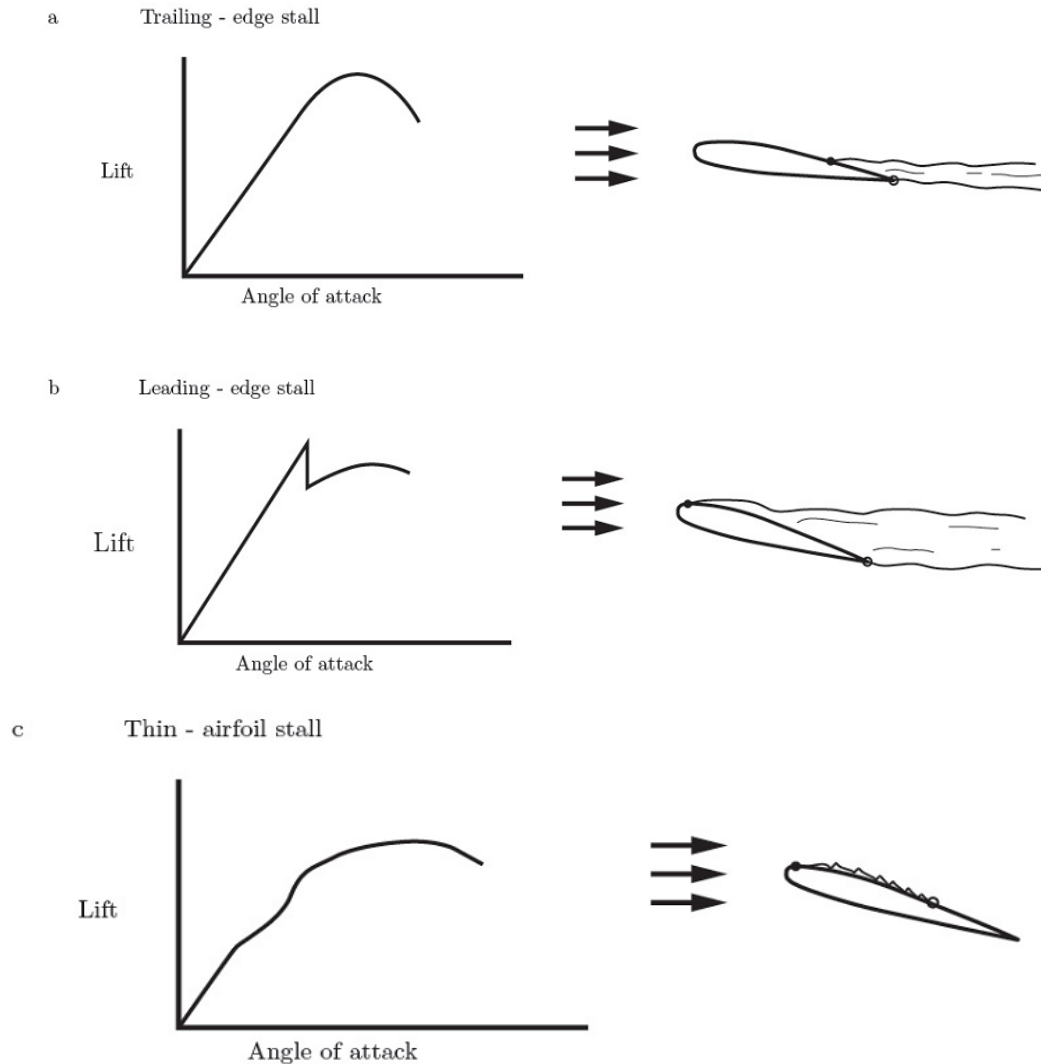


Fig.I.23. Lift behavior for different stall types [31]

I.10.2. Dynamic stall

The difference between static and dynamic stall is that the dynamic will occur on airfoils that are subjected to unsteady conditions. According to Larsen et al. [32] the first step of dynamic stall phenomenon is the development of a leading edge separation bubble. In this case two types of boundary layer separation can occur simultaneously which will also result in two different lift curves. The first type is that the boundary layer will reattach due to the turbulent layer behind the bubble. The second one is that the flow will separate completely at the bubble without attached to the suction surface.

With increasing AoA, the leading-edge vortex will keep growing linearly; simultaneously a suction zone will be created. Due to this suction zone, the lift will keep on increasing. At a

given point, the vortex will detach from the leading edge, and it will be transferred downstream the airfoil with a speed of approximately equal or slightly less than the incoming flow velocity. The lift is still growing as long as the vortex is staying near the suction surface.

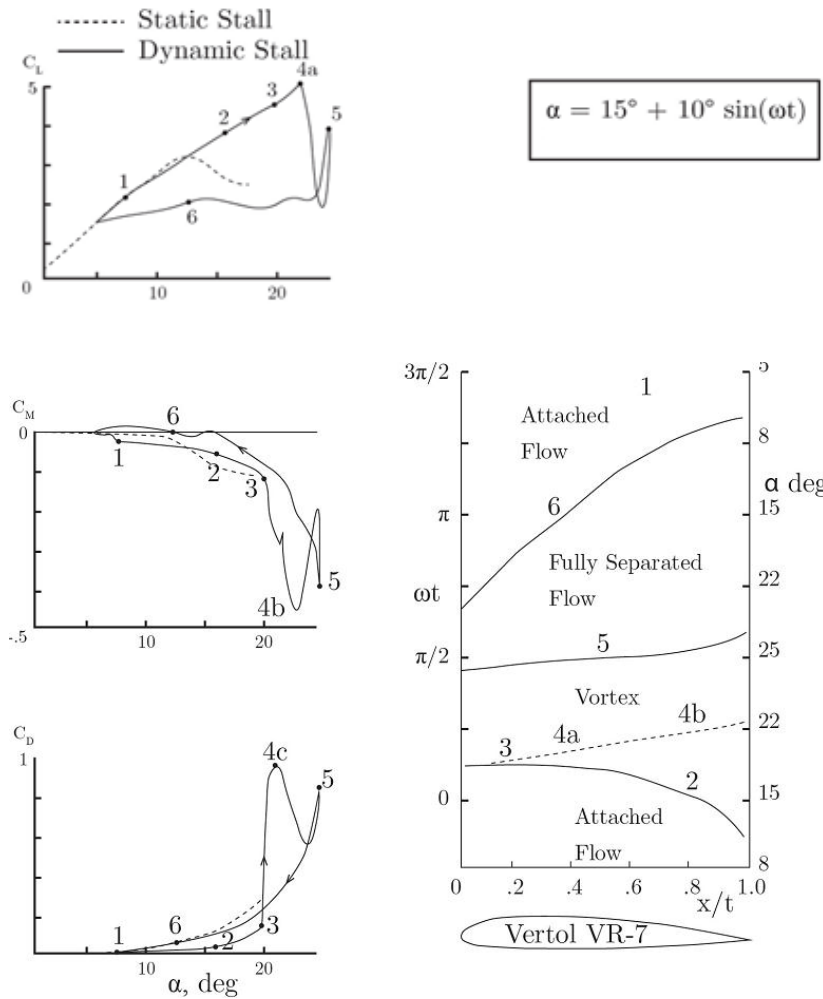


Fig.I.24. Lift, moment and drag coefficients under static and dynamic stall [33]

During the decreasing AoA's the flow will re-attach again from the leading edge. While for very low values of AoA's, the separation point will slowly move backwards, and the separation zone continuous in decreasing until a full attached flow state. During this process of re-attachment, the lift generated by the airfoil will be lower than that in the static case for the same AoAs.

Fig.I.24 depicts the lift, drag and moment curve of an airfoil in dynamic stall. It represents a summary of the unsteady aerodynamics that discussed previously. Between point 1 and 2 an attached flow is recorded on the airfoil. The lift surpasses the static polar. The leading edge

vortex appears at point 2, and grows until point 3. This vortex contributes in a linear increase of lift, and consequently induces a larger drag and moment on the airfoil.

At point 3 the vortex will separate and move downstream. The large suction zone that formed provides increasing lift. The drag and moment curves show big changes at this point. Due to the vortex moving along the airfoil the moment curve drops extremely, and the drag coefficient will increase radically.

At point 4 the leading edge vortex reaches the trailing edge, and the lift decreases; however the moment coefficient slightly increases again. At point 5 the trailing edge vortex formation can be registered where the lift will increase a little for a second time, and the moment coefficient drops again. A flow re-attachment happens at point 6. McCroskey [33] outlined that an airfoil having a relatively sharpened leading edge, is more likely to control dynamic stall. This can form a leading-edge vortex, which will ultimately improve lift as shown in Fig.I.24.

I.10.3. Dynamic stall in Darrieus turbines

Dynamic stall occurs often on VAWT due to its rotary configuration. This is the results of several causes: the variation of AoA over one rotation, the flow curvature and the operating range of tip speed ratio TSR.

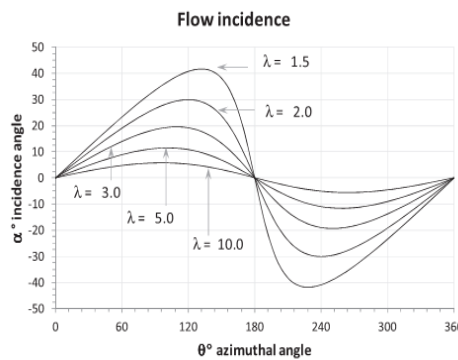


Fig.I.25. Variation of AoA versus azimuthal positions [27]

The AoA is determined by the rotational speed and the free stream velocity resulting in an induced flow behavior.

Fig.I.25 shows the variation of AoA at azimuthal positions varying from 0 to 360°. This plot was made for a turbine with different TSR [27]. As explained previously, cyclic AoA's cause a dynamic stall especially in the regions between 0-180°.The figure shows that the 12° value which is the frequently the value of the static stall is never reached for TSR > 5. This value is

a typical nominal tip speed ratio for a VAWT wind turbine, showing that only a slight stall regime can occur.

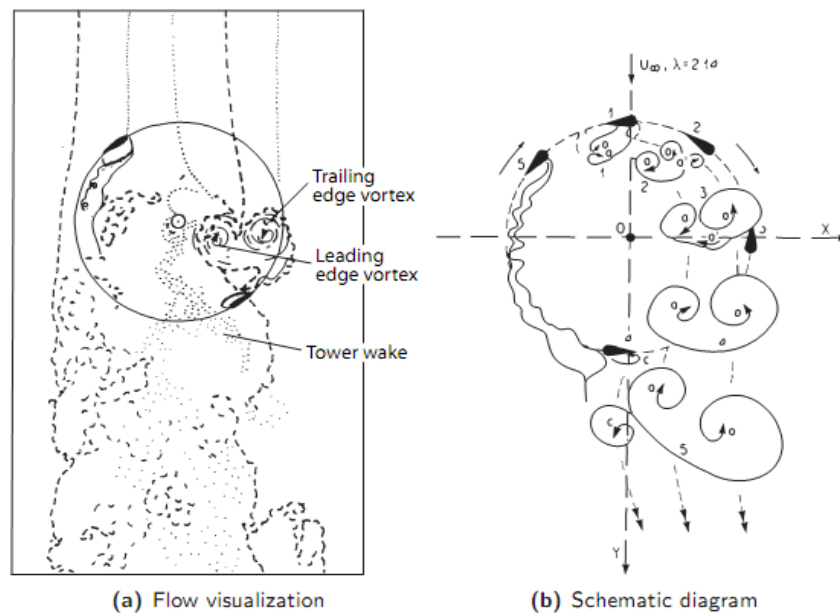


Fig.I.26. Visualization of dynamic stall at $\lambda = 2.14$ [33]

As it is mentioned previously, the Darrieus type wind turbine is particularly subjected to dynamic stall, due to the large change in angle of incidence, especially at low tip speed ratios. When the blades achieve a complete round, the blades in the downstream part of the turbine are influenced by the wake resulting from the upstream blades. The understanding of the mechanism by which dynamic stall and the resulting wake influence the turbine efficiency is therefore important. By using a water channel, Brochier et al [34] performed visualizations of the dynamic stall for the VAWT, visualizations were carried by means of Laser Doppler velocimetry (LDV) and hydrogen bubbles at a Reynolds number of 10,000 and tip speed ratios varying from 1 to 8 on a Darrieus turbine having two NACA 0018 blades. The results for $\lambda = 2.14$ are depicted in Fig.I.26. A counter clockwise vortex is formed at the leading edge of the blade. Another vortex, turning in the counter clockwise direction, initiates from the trailing edge. This shedding forms the illustrating counter rotating vortices, that move downstream to interact with the second blade. The same behavior is shown by measurements made in a water channel using particle image velocimetry by Fujisawa and Shibuya, [35] on a one NACA 0018 blade Darrieus turbine. The flow pattern is depicted in Fig.I.27. and Fig.I.28. The shedding vortices are clearly visible. Two types of stall vortices are recovered. The first one is formed at small blade angles and grows in the wake. The second one is formed at large blade angles and will follow the blade trajectory. As the angles of incidence are larger at

lower tip speed ratios, the dynamic stall is more acute. As it is illustrated in the figure, large vortices are detached which produce a deep stall. At higher tip speed ratios, the dynamic stall will become ineffective. Even if dynamic stall will improve the performance of the turbine, it has certain negative influence. Such as noise, aero-elastic vibrations and blade fatigue. Both investigations show a large irregularity in the flow properties inside the turbine. The blades interact with the wake in only a part of the cycle. In this part they will experience extremely turbulent flow.

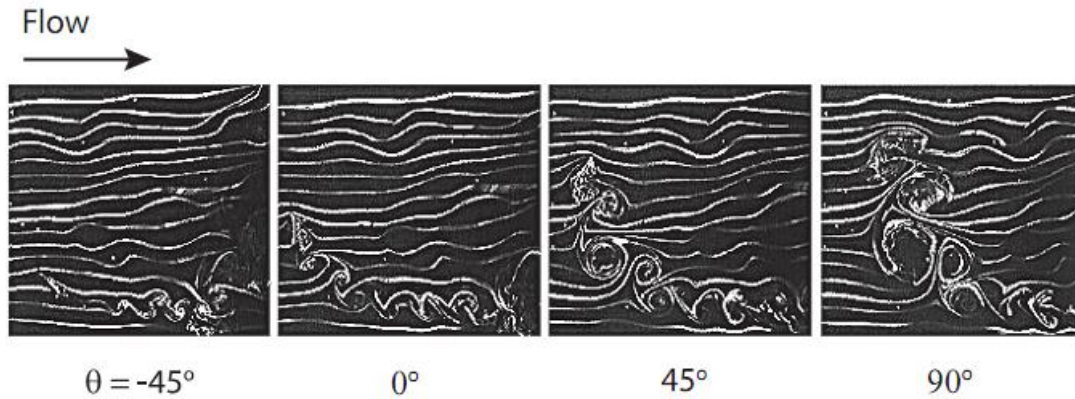


Fig.I.27. Flow visualization at four different positions, [35]

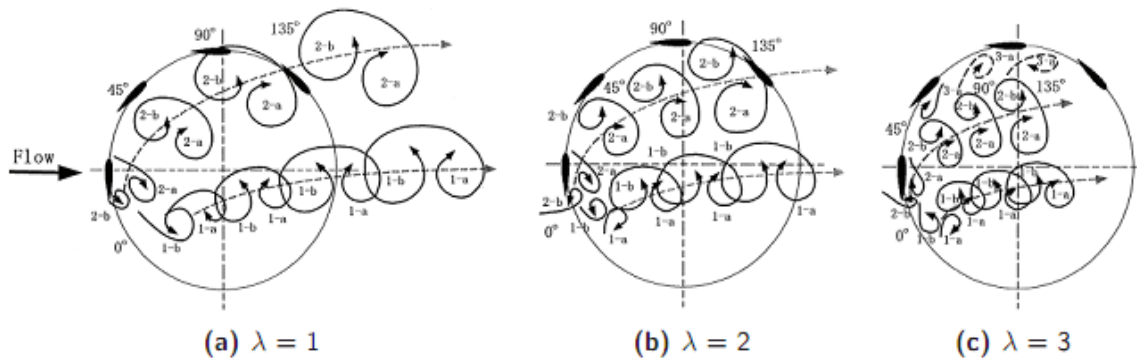


Fig.I.28. Schematic illustration of the dynamic stall for different λ , [35]

I.11. General notes about the flow control

Controlling a flow means all operations that involve modifying the properties of the flow to bring it to a desired state. Such action is usually applied near the wall which can be an addition of fluid mass, energy or momentum. Currently, it is the newest subject in fluid mechanics research. The interests in producing systems that operate in controlled flow are multiple. The control strategy is determined by the chosen objective. The control may be used

to reduce the wall friction, delay the transition, increase the mixing for heat and mass transfer and reduce noise or vibration.

I.11.1.The challenges of controlling flows

For both the civilian and military sectors, manipulating the flows has many goals. In the civilian sector, the issues are essentially economic. A 10% reduction in drag of a civilian aircraft causes a reduction in fuel consumption of 50 million liters during the aircraft life cycle. McLean et al [36] outlined that the use of synthetic jets to control the flow over a Boeing 737-700 would reduce its weight of 2.87% and the operating costs about of 0.74%.

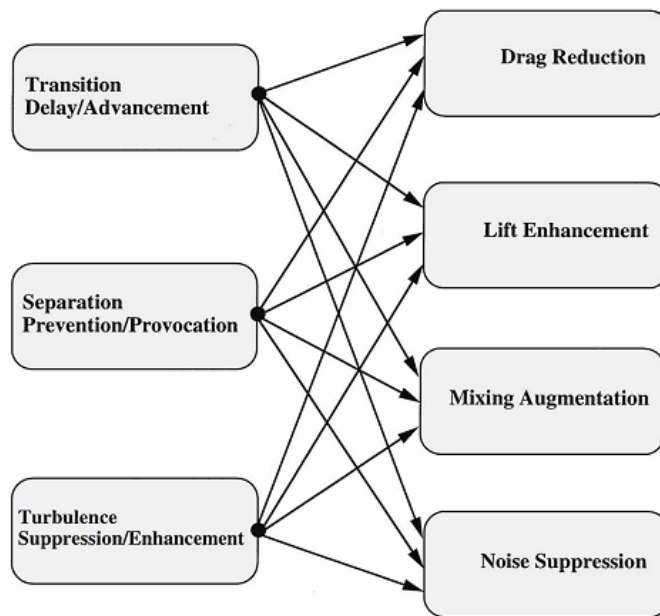


Fig.I.29. Engineering goals and corresponding flow changes [38]

Gomes, Crowther and Wood [37] estimated the electrical power needed for the flow control on an Airbus A321. In the case of a control that would replace the slots of the leading edge with synthetic jets, the electric power consumed at the takeoff would 200kW for 1653 actuators for each wing, which represents 70% of the electrical power available from the auxiliary generator of power. In the case of actuators placed on the trailing edge flaps in order to improve their performance, the consumed electric power is 70 kW for 213 actuators by wing, which represents 30% of the generator power. These numbers show that for the current state, the power needed for a control with synthetic jet is acceptable and it is already compatible with the use on an airliner. The challenges are also environmental, the guidelines delivered by the European Commission on pollution and noise around airports are becoming

more severe. A drag reduction is associated with a reduction in consumption which reduced emissions. In the military field, the challenges are more technological and focused on performance: it is for example included the reduction in landing and takeoff distances but the speed of execution is the main objective.

I.11.2. Relations between the different objectives of control

A partial representation of the interrelationships between the different control objectives is shown in Fig.I.30. The flow around an airplane wing can illustrate precisely this idea of interrelations goals. Indeed, when the boundary layer becomes turbulent, it resists separation and therefore the lift increases significantly. Nevertheless, for a laminar flow the drag due to the friction is lower than that of the turbulent cases [38]. A delay of the transition results in a reduction of the wall friction and induced noise. The laminar boundary layer can resist only small negative pressure gradients in terms of separation. Therefore, a reduction of the lift is necessarily accompanied by an increase in the shaping drag.

I.11.3. Classifications of flow control methods

There exist many classifications for flow-control methods. One is based on the location of the actuator; if it is applied at the wall or away from it. Among the control strategies that locate at the wall: rigid-wall motion and heating or cooling the wall surface [38]. The use of control mechanisms located away from the wall can also be useful. Among these control strategies: acoustic waves that bombing the shear layer from the outside, also there is a method based on handling the free stream turbulence levels. The flow-control methods can also be classified based on the energy consumption or the input power. As shown in the schematic in Fig.I.31, a control device can be passive, requiring no auxiliary power and no control loop, or active, requiring energy expenditure. As for the action of passive devices, some prefer to use the term flow management rather than flow control, reserving the latter terminology for dynamic processes [38]. Active control requires a control loop and is further divided into predetermined or reactive categories. Predetermined control includes the application of steady or unsteady energy input without regard to the particular state of the flow. The control loop in this case is open, as shown in Fig.I.31 and no sensors are required. Because no sensed information is being fed forward, this open control loop is not a feed forward one [38].

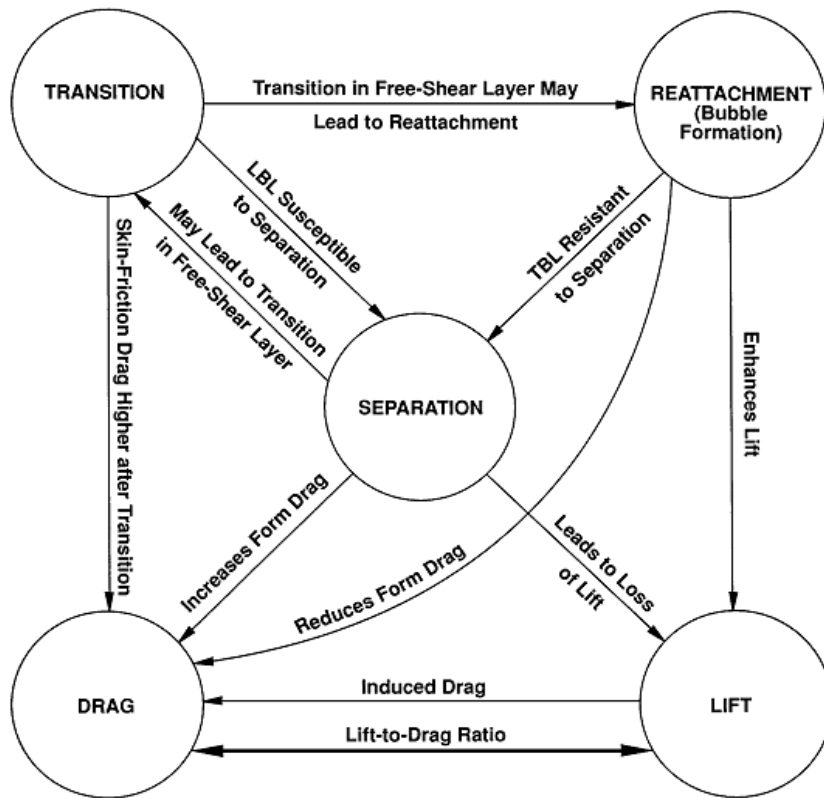


Fig.I.30. Interrelationships between the different control objectives [38]

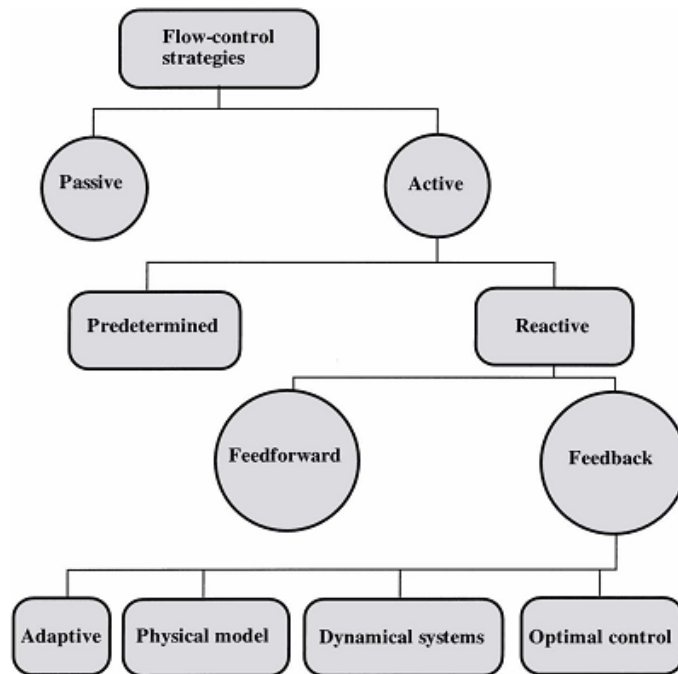


Fig.I.31. Classification of flow-control strategies [38]

This point is often misunderstood in the literature and results in predetermined control being confused with reactive, feed forward control.

Reactive control is a special class of active control in which the control input is continuously adjusted based on measurements of some kind. The control loop in this case can either be an open feed forward one or a closed feedback loop. Classical control theory deals, for the most part, with reactive control.

I.12. Problematic of active control

An active control technique means that an amount of energy often in the form of a momentum is introduced from the external environment to the flow to change its natural evolution towards a desirable state. This effect allows in particular delaying the boundary layer separation. The added energy may have multiple sources which can be electrical, mechanical or thermal source.

I.12.1. Flow control by using moving wall

The concept of this technique is to provide, an amount of momentum that is necessary for the flow control by using moving or deforming walls. So, the operation of this control mechanism depends essentially on the nature, amplitude and on the frequency of the moving wall. A small vibration allows manipulating the developing instabilities in the boundary layer and thereby changes the flow overall structures.

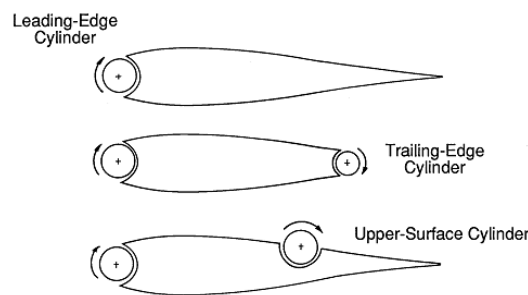


Fig.I.32. Various rotating cylinder configuration used to increase lift and delay stall of an airfoil [38]

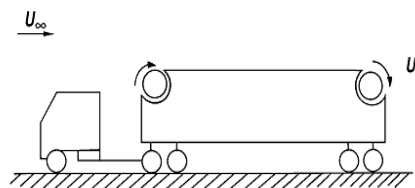


Fig.I.33. Tractor-trailer truck with rotating cylinders [38]

Many studies have examined the cylinder movable walls. The separation of the boundary layer is delayed, and could even be deleted in the side region of the cylinder if the wall motion is done in the same direction as the incident flow.

Modi et al [39] have shown the efficiency of this technique for reducing the drag of a wing profile and delay the separation around a truck profile. The work of Ericsson [40] highlighted a 200% increase in lift and a decrease in the stall angle by placing of rotating cylinders at the trailing edge and the leading edge of a profile (Fig.I.32). The motion of the wall produces another effect which is the producing of a parietal shear layer that can make the boundary layer more resistant to the adverse pressure gradient and thus delay the separation.

I.12.2. Flow control by suction and blowing

Typically, Blow or draw a boundary layer can cause a change in the flow. The principle of blowing is to add the momentum directly in the boundary layer to delay the separation. This can also be achieved by an auxiliary blowing system, such as a compressor or by a slit in the leading edge level. The suction of the boundary layer eliminates the layer in which the flow is already slowed down before it begins separated. This action causes a strong diversion of the flow towards the wall and can regenerate a new boundary layer which is more resistant to adverse pressure gradient.

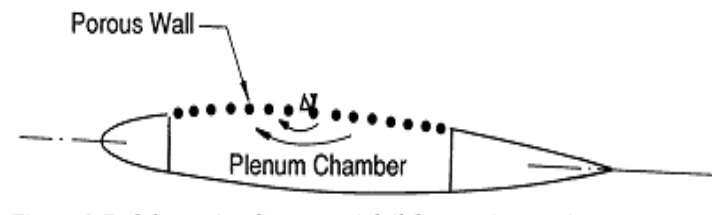


Fig.I.34. Schematic of porous airfoil for suction [38].

I.12.3. Thermal control

The separation of the boundary layer can be manipulated by thermal actuators which animate the area near the wall by an amount of heat sufficient to change the density if the fluid is a gas or the viscosity if it is a liquid. This effect compensates the near-wall boundary layer with a sufficient momentum to make it more resistant to separation. The work of Cassel [41] has shown that this type of control has desirable effects from aerodynamic performance

standpoint. However, its application is not evident due to the large amount of energy to be supplied.

I.12.4. Flows control by using flapping wings

Gopalkrishnan et al. [42] have used this strategy to control the flow at the backward of a circular cylinder for Reynolds numbers between 500 and 20000. Three basic interaction modes have been identified when the profile performs a flapping and a pitching oscillation at a frequency close to the cylinder's Strouhal number, Under certain optimal flapping and flow conditions, these interactions can lead to the phenomenon of reverse Karman's Street.

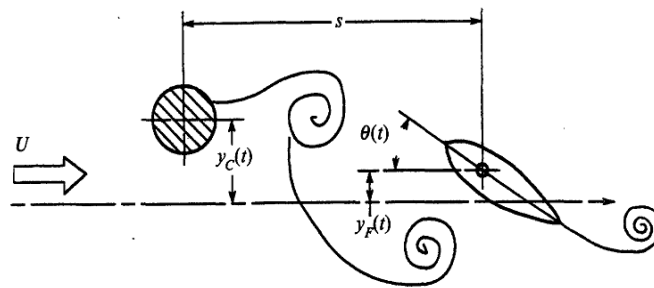


Fig.I.35. An oscillating symmetric foil placed in the wake of a cylinder oscillating transversely [42].

Lai et al. [43] carried out an experimental study by using small flapping wing in plunging motion to control the separating shear layer in two-dimensional backward. Results show that when the foil is close to the separation region, the detached shear layer can effectively controlled, which reducing the reattachment length about 70%.

Jones [44] has described in deep investigation the effect of flapping wings on the flow separation control. A small oscillating foil is attached to the trailing edge of a cusped stationary airfoil. Results show that the flow separation can effectively controlled when the foil starts its flapping movement, and under specific conditions the separation zone disappears completely.

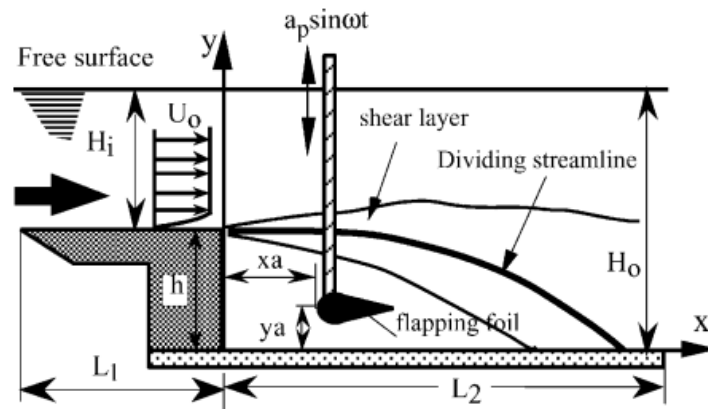


Fig.I.36. Schematic showing experimental set-up for a backward facing step flow[43]

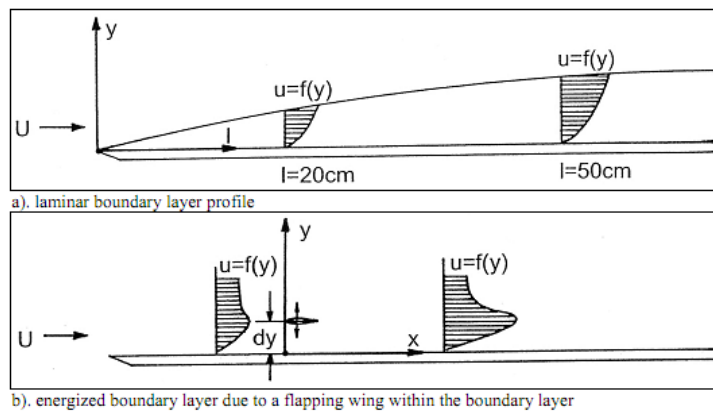


Fig.I.37. Effect of small flapping wing on laminar boundary layer over a flat plat [44].

To understand more this fact, he mounted a small oscillating foil close to the trailing edge of a large cusped stationary airfoil (this geometry is specially chosen like that to ensure the detachment of the boundary layer).

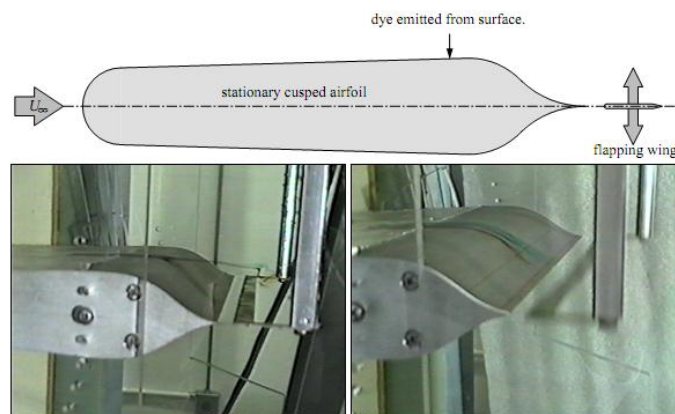


Fig.I.38. Flow separation control around a large stationary wing by mean of flapping wing

[44]

When the small profile is maintained fixe the boundary layer separation is well observed (left part in Fig.I.39). This separation zone become small when the small profile begins its flapping movement (right part in Fig.I.39) and it can also yield to its total suppression under specific conditions of flapping frequency and amplitude [44].

After constructed the model showed in Fig.I.39, Jones et al [44] performed experimental tests on this design, and concluded that the flapping-wings motion suppresses stall on the stationary wing.

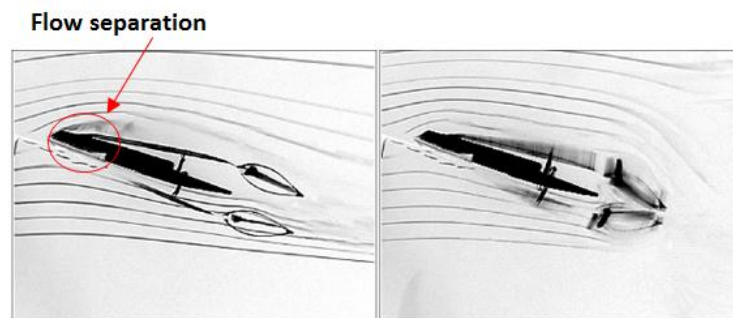


Fig.I.39. Stall suppression due to flow entrainment [44].

I.12.5. Flow control by flexible wing

Xiao et al. [45] have used an undulation NACA0012 foil to control the flow around a D-section cylinder. Results show that the drag force reduced about 57.4% as compared to the cylinder without control.

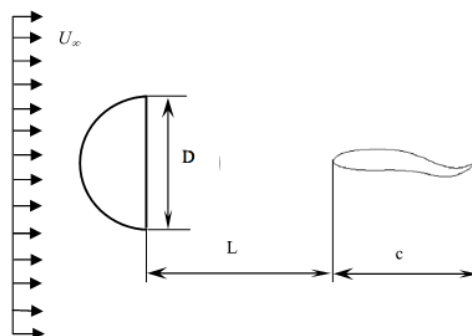


Fig.I.40. Cylinder–Undulation(flexible) foil system [45]

A flexible wing in a plunging motion was studied computationally by Miao et al. [46] . In their investigation, for various Reynolds numbers and reduced frequencies, a systematic parametric study is performed on the effect of chord-wise flexure amplitude in unsteady aerodynamic characteristics; the propulsive efficiency is enhanced for a flapping airfoil with

flexure amplitude of 0.3 of the chord length. The study also examine the propulsive efficiency and thrust under various Reynolds numbers and reduced frequency conditions. The results show that the propulsive efficiency has a strong correlation with the reduced frequency. the highest propulsive efficiency reached at a Strouhal number St of 0.255.

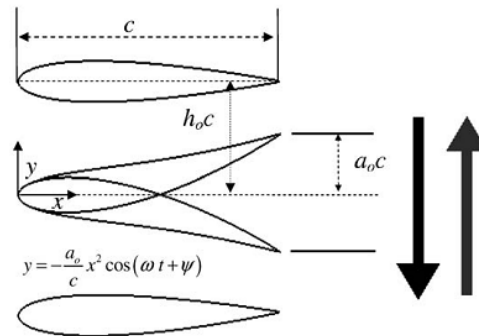


Fig.I.41. Plunge and deflection motion of single flexible airfoil [46]

I.12.6. Other types of active control

Several other techniques and methods have been extensively tested for experimental control. Include sound control that requires the use of sound waves will interact with the boundary layer. Control by heating parietal films, so as to locally modify the viscosity of the fluid. Also ones can cite the cavitation control and chemical reaction technologies. It is also possible to inject at the wall another fluid that has different viscous properties and create a local viscosity gradient [38].

I.13. Problematic of passive control

Passive method consists in performing a slight modification of the geometry of the system to change the flow field without the need to an external energy.

I.13.1. Different types of passive actuators

In Turbulent regime, the boundary layer is more resistant to separation than in laminar regime. Thus, the mechanisms used for passive control are designed to force the transition at the boundary layer. Therefore, geometric changes that take the form of rough serrated, grooved or rounded are placed upstream the separation zone in order to generate disturbances that causing the desired transition.

I.13.2. Passive vortex generators

The role of the vortex generators, placed in the transverse direction of the flow is to support the interaction between large vortex structures in order to increase the mixing and thus the

transfer between the rich zone on kinetic energy and the immobile fluid near the wall. This type of control is currently used in aviation and in automotive aerodynamics.

I.13.3. Adding solids

This type of actuator consist to mount mechanical systems, such as fins or slot placed at the leading edge or trailing edge of a wing, to direct the flow towards the immobile fluid area [38] to add a momentum that is necessary for the control

I.14. Conclusion

In the first chapter, the bibliographic study allows defining the different types of vertical axis wind turbines. Furthermore, a detailed analysis of the vertical axis wind turbine conception with its operating principle and the associated parameters is carried out.

In the second part, general concepts on the flows control are presented. It is apparent that the control strategies depend on the nature of the flow. The active control requires an external supply of energy in order to manipulate the flow field, the passive control, however, doesn't require any input power from the external environment.

CH II: NUMERICAL METHODOLOGY

II.1. Introduction

In this chapter, general descriptions of the CFD methods and the suggested vertical axis wind turbines VAWT's models including their constituents and their dimensions are provided. Next, a discussion about the flapping-wings motion and their control parameters is carried out. As it is mentioned in the general introduction two approaches of flow control are investigated, flow control by using backward flapping wings and flow control by the means of flapping flexible wings.

The CFD methods of all flows types can now be considered as a real "numerical experiences" if they made carefully. The advantage of "numerical methods" is that all physical quantities related to the flow such as velocity field, pressure field, constraints, etc. are immediately available at any point in the flow. In an experiment, obtaining these quantities at any point of the field is often impossible or very difficult. The Computational Fluid Dynamics (CFD) methods have the advantage of implementing the general equations that govern such flow with the minimal of assumptions. They especially solve nonlinear, unsteady and compressible equations. The discretization of the Navier-Stokes and the mass conservation equations is made on quadrilateral or triangular elements, depending on the complexity of the geometry. It leads to a system of coupled non-linear equations. This system can be solved iteratively.

Before performing any calculation in the CFD software's, it is needed to know some basic theoretical concepts. These concepts concern the definition of the main equations governing the flow and modeling the theory of turbulence.

The equations that governing the flow are the Navier-Stokes and continuity equations which are written for an incompressible Newtonian fluid [47] as:

$$\frac{\partial u_i}{\partial t} + u_j \frac{\partial (u_i)}{\partial x_j} = -\frac{1}{\rho} \frac{\partial p}{\partial x_i} + \frac{\partial}{\partial x_j} \left(\nu \frac{\partial u_i}{\partial x_j} \right) \quad \text{II.1}$$

$$\frac{\partial u_i}{\partial x_i} = 0 \quad \text{II.2}$$

With $u_- = (U, V, W)$ is the velocity vector, t is the time, p is the pressure, ρ is the density and ν is the kinematic viscosity of the fluid.

Several methods such as the method of finite element and finite volumes are recommended to solve the Navier-Stokes and continuity equations. The finite volume method is currently the basis of several advanced commercial calculation codes in the field of fluids mechanics and heat transfer, such as CFX, FLUENT and STAR-CD.

For the flow in turbulent regime, several modeling schemes are available to model and solve the above equations: direct numerical simulation (DNS), the large eddy simulation (LES) and the statistical Reynolds average simulation (RANS). The capacity of the computers, the complexity of the geometry of the models and the degree of accuracy are the factors that will guide us to choose the appropriate schemes.

II.2. Turbulence modeling

II.2.1. DNS (Direct Numerical Simulation)

The equations governing the flow are a mathematical representation of the fundamental physical features. The most accurate approach for the simulation of turbulence is to solve all equations without any turbulence modeling. The direct numerical simulation is a method that solves the Navier-Stokes equations without making any hypothesis on turbulence properties. It provides an access to all the flow physical information. The limitation of this method is the necessity to generate a mesh, at least, as thin as the smallest vortex appears in the flow. It requires, therefore, a large storage memory [47].

II.2.2. Statistical approaches (RANS)

In this approach, the variables describing the motion are decomposed in a statistical average value and fluctuations around this average. In a first methodology, the mean motion is considered stationary and all the fluctuating movements are considered as random. Averaging the Navies-Stokes equations leads to a system of equations for the mean motion. The approach URANS 'Unsteady Reynolds Averaged Navies Stokes is the most widely used method. This approach often leads, in the case of separated flows, to low predictions of the flow proprieties due to the of correction of length scales of turbulent motion used for these models [47].

II.2.3. Large Eddy Simulation LES

The approach LES (Large Eddy Simulation) is a compromise between the two previous methods. With this method, only the large vortices are calculated and the small scale vortices

are modeled by a Sub-Grid Scale Model. This method provides a finer physics because large flow structures are more energetic. This method requires fewer resources than the DNS approach but much more than the RANS method. The LES method provides access to more information about the unsteady flow behavior. The interest of this method is first linked to a large reduction in resources requirements compared to DNS and also to the additional information provided relative to the RANS approach.

Another method that can be classified in the Large Eddy Simulation group is the Detached Eddy Simulation (DES) which is a hybrid method, consists of combining a RANS method for boundary layers regions and a LES method in the outer regions.

II.3. Historic review of numerical models employed for VAWT simulation

Due to the flow nature over rotating blades, the modeling of the unsteady component of the flow requires a time accurate model; also the large amount of the shedding vortices suggests that the model should be sensitive to the numerical dissipation. Typically, the performance of a VAWT is obstructs by the mutual aerodynamic interactions between the blades, which are due to the wakes generated by the blades. This means that the flow inside the whole rotor diameter must be modeled properly; in order to avoid numerical dissipation. The spatial resolution of the grid must be fine not only in the region near the blade wall but over the entire rotor. Moreover, the correct use of a turbulence model and near-wall model is essential for the best prediction of lift and drag forces which are sensible to the variation of flow angle of attack. Previous investigations have resorted to RANS models; due to the best prediction of lift and drag forces.

For a single-bladed NACA0015 VAWT, Simão Ferreira et al. [48] carried out a comparison between two URANS models (Spalarte-Allmaras and $k-\epsilon$) and the LES and DES models with experimental vorticity visualizations. Authors outlined that the DES model can predict better the experimental results as compared to the other models. However it should be noted that the lift and drag forces found with this model are very close to those obtained with the RANS models. This suggests that the use of RANS models is very hopeful for the VAWT modeling. The listed researchers have resorted to these models (Hansen et al [49], Allet et al [50], Paraschivoiu et al [51], Paraschivoiu et al [52] and Paraschivoiu [53]))

Iida et al. [54] utilized both LES model and momentum model to simulate the flow over a three straight bladed NACA 0018 VAWT. For tip speed ratio equal or higher than 3, the

power coefficients found with the two models are very close. The LES model described accurately the flow structures interactions, leading to power coefficients close to the experimental ones. Chao Li et al [55] investigated the practicability and the precision of three different CFD approaches, namely 2D URANS, 2.5D URANS and 2.5D large eddy simulations (LES). The 2.5D model contrasts with a full 3D model in which only a certain length of blades is modeled with periodic boundaries at the two extremities of the domain. Among the three tested methods, 2.5D LES generated the best agreement with the experimental results.

II.3.1. The realizable $k - \varepsilon$ model

The realizable $k - \varepsilon$ turbulence model has been developed by Shih et al [56] it contains a new transport equation which accounts the turbulent dissipation rate. In the standard $k - \varepsilon$ model, the model coefficient has a constant value; however, in the realizable $k - \varepsilon$ model the coefficient is expressed in terms of the turbulence properties, this comportment consistent with the kind of the turbulence. The transport equations for k and ε in the realizable $k - \varepsilon$ model are:

$$\frac{\partial}{\partial t}(\rho k) + \frac{\partial}{\partial x_i}(\rho k u_j) = \frac{\partial}{\partial x_i} \left[\left(\mu + \frac{\mu_t}{\sigma_k} \right) \frac{\partial k}{\partial x_j} \right] + G_k + G_b - \rho \varepsilon - Y_M + S_k \quad \text{II.3}$$

and

$$\frac{\partial}{\partial t}(\rho \varepsilon) + \frac{\partial}{\partial x_j}(\rho \varepsilon u_j) = \frac{\partial}{\partial x_j} \left[\left(\mu + \frac{\mu_t}{\sigma_\varepsilon} \right) \frac{\partial \varepsilon}{\partial x_j} \right] + \rho C_{1\varepsilon} S_\varepsilon - \rho C_{2\varepsilon} \frac{\varepsilon^2}{k + \sqrt{v\varepsilon}} + C_{1\varepsilon} \frac{\varepsilon}{k} C_{3\varepsilon} G_b + S_\varepsilon \quad \text{II.4}$$

Where

$$C_1 = \max \left[0.43, \frac{\eta}{\eta + 5} \right] \quad \text{II.5}$$

And

$$\eta = S \frac{k}{\varepsilon} \quad \text{II.6}$$

In these equations, k is the turbulent kinetic energy and ε is the dissipation rate of the kinetic energy. G_k is the generation of turbulence kinetic energy due to the velocity gradients. G_b is the generation of turbulence kinetic energy due to buoyancy. Y_M is the fluctuating dilatation contribution to the overall dissipation rate. S_k and S_ε are user-defined source terms. σ_k and σ_ε are the turbulent Prandtl numbers for k and ε respectively. μ_t is the turbulent viscosity. $C_{1\varepsilon}$, $C_{2\varepsilon}$ and $C_{3\varepsilon}$ are the constant parameters of the model. The Realizable $k - \varepsilon$ model usually shows better results for swirling and separating flows compared to the standard $k - \varepsilon$ model.

II.3.2. The Large Eddy Simulations model

- LES subgrid-scale models

The Wall Adapting Local Eddy-Viscosity model is based on Smagorinsky approach. This new formulation makes it possible to take into account the turbulent areas where the vorticity is higher than the deformation ration and to give a good approximation to the subgrid-scale turbulent viscosity. Nicoud and Ducros [57] estimated the subgrid-scale turbulent viscosity as:

$$\mu_t = \rho L_s^2 \frac{(S_{ij}^d S_{ij}^d)^{3/2}}{(\overline{S_{ij} S_{ij}})^{5/2} + (S_{ij}^d S_{ij}^d)^{5/2}} \quad \text{II.7}$$

$\overline{S_{ij}}$ is the rate-of-strain tensor for the resolved scale given by:

$$\overline{S_{ij}} = \left(\frac{\partial \overline{u_i}}{\partial x_j} + \frac{\partial \overline{u_j}}{\partial x_i} \right) \quad \text{II.8}$$

L_s is the mixing length for subgrid-scales defined as:

$$L_s = \min(\kappa d, C_w V^{1/3}) \quad \text{II.9}$$

S_{ij}^d are computed using:

$$S_{ij}^d = \frac{1}{2} (\overline{g_{ij}^2} + \overline{g_{ji}^2}) - \frac{1}{3} \delta_{ij} \overline{g_{kk}^2}, \quad \text{II.10}$$

$$\text{Where } \overline{g_{ij}} = \frac{\partial \overline{u_i}}{\partial x_j} \quad \text{II.11}$$

Where κ is the von Karman constant, d is the distance to the closest wall, $C_w = 0.325$ is the WALE constant and it has been found to yield satisfactory results for a wide range of flow.

II.4. Near-Wall treatments in ANSYS Fluent

Typically, the presence of walls influences turbulent flows. The tangential velocity fluctuations are reduced in the region close to the wall, due to viscous damping, while kinematic blocking reduces the normal fluctuations [58]. When we move toward the outer part of the near-wall region, however, the turbulence is quickly increased by the creation of turbulence kinetic energy due to the large gradients in mean velocity. The near-wall modeling affects deeply the accurateness of numerical solutions, due to the fact that walls are the main source of mean vorticity and turbulence. Generally, the solution variables have large gradient in the near-wall region where the momentum and other scalars occur to be more dynamically.

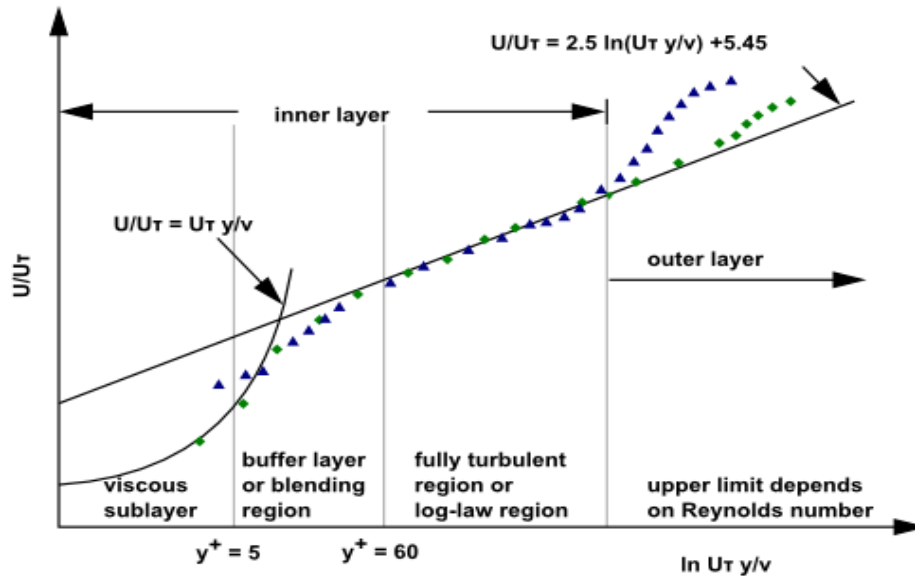


Fig.II.1.Subdivisions of the Near-Wall region [58]

Consequently, precise modeling of the flow in the near-wall region controls successfully the solution of the wall turbulent flows. Several investigations have shown that the near-wall region can be subdivided into three layers. The nearest layer, called the “viscous sublayer”, the flow is almost laminar and the viscosity governs momentum and heat or mass transfer. In the outer layer, called the fully-turbulent layer, turbulence shows an influencing role. The last region called buffer layer it located between the viscous sub layer and the fully turbulent layer where the molecular viscosity and turbulence have the same effects. Fig.II.1 illustrates these subdivisions of the near-wall region.

II.5.Wall functions versus near-wall model

Conventionally, there are two approaches to resolve the near-wall region. In the first one, the regions of viscous sub layer and buffer layer are not resolved. As a replacement, semi-empirical formulas called “wall functions” are used to connect the two previous regions and the fully-turbulent region. The use of wall functions avoids the requirement to modify the turbulence models due to the presence of the wall. In the second approach, the turbulence models are modified to allow the viscosity-affected region to be resolved with a finer mesh at the wall, including the viscous sub layer. These two approaches are shown schematically in Fig.II.2.

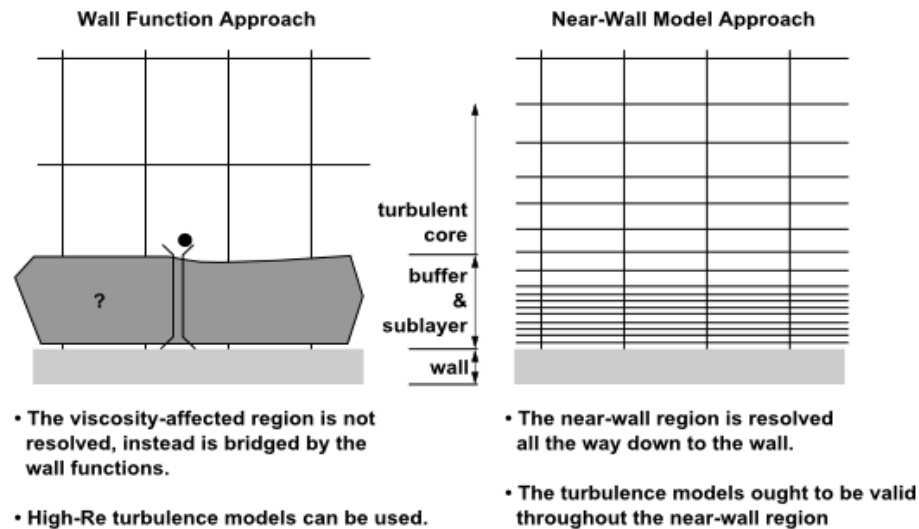


Fig.II.2.Near-Wall treatments in ANSYS Fluent [58]

The foremost scarcity of all wall functions is that the numerical results worsen under refinement of the grid in the wall normal direction y^+ values less than 15 will progressively result in absolute errors in wall shear stress and wall heat transfer. ANSYS Fluent has taken in charge to provide more advanced wall formulations that need a regular mesh refinement without a worsening of the results. Those wall formulations are the default for all ω -equation-based turbulence models. For the ε -equation-based models, the Menter-Lechner and Enhanced Wall Treatment (EWT) are used. Also for the Spalart-Allmaras model y^+ insensitive wall treatment is used and it permits to use this model independent of the near-wall y^+ resolution. If the resolution of the boundary layer is sufficient, accurate numerical results for the wall boundary layer will be obtained.

The minimum number of cells to cover a boundary layer accurately is around 10, but value of 20 is required. Another method to improve the boundary layer modeling is the increase in mesh refinement in the wall-normal direction. Typically the supplementary increase in mesh refinement means additional computing costs.

For unstructured meshes, it is preferable to generate layers near the wall with 10–20 or more layers for an accurate modeling of the flow near the wall boundary layers. The thickness of the layer should be calculated to ensure that around 15 or more nodes are essentially covering the boundary layer. This can be verified after a solution is obtained, by analyzing the turbulent viscosity, which has a maximum in the middle of the boundary layer – this maximum gives an indication of the thickness of the boundary layer (twice the location of the maximum gives the

boundary layer edge). It is essential that the prism layer is thicker than the boundary layer as otherwise there is a danger that the prism layer confines the growth of the boundary layer [58].

- **Recommendations:**

- For the ε -equation, use Menter-Lechner (ML- ε) or Enhanced Wall Treatment (EWT- ε)
- If wall functions are favored with the - ε equation, use scalable wall functions
- For the ω -equation based models, use the default y^+ -insensitive wall treatment - ω equation
- For the Spalart-Allmaras model, use the default - y^+ insensitive wall treatment.

- **Wall Functions**

Wall functions are a set of semi-empirical formulas and the solution variables at the near-wall cells and the corresponding quantities on the wall. The wall functions comprise

- law-of-the-wall for the mean velocity and temperature (or other scalars)
- formulae for the near-wall turbulent quantities [58]

Depending on the choice of turbulent model, ANSYS Fluent offers the following choices of wall-function approaches:

- Standard Wall Functions
- Scalable Wall Functions
- Non-Equilibrium Wall Functions
- User-Defined Wall Functions

II.6. Flow control by using backward flapping wings

II.6.1. Model description

The developed model consists of a three-bladed Darrieus VAWT, at each blade of NACA0021 profile, is associated a pair of after-positioned NACA0010 profile flapping wings (Fig.II.3).The main geometrical features of the considered rotor are summarized in Table 1.

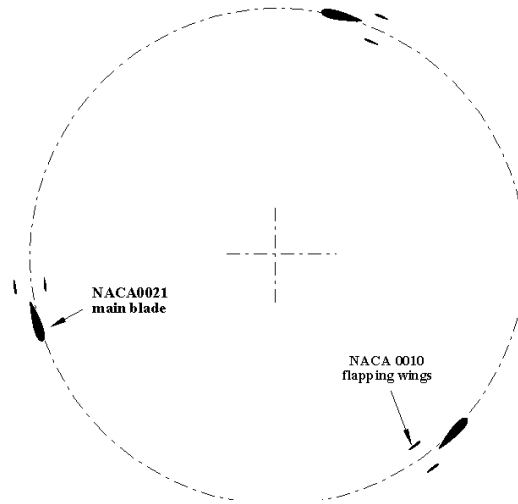


Fig.II.3. Photographs for the VATT models over one revolution.

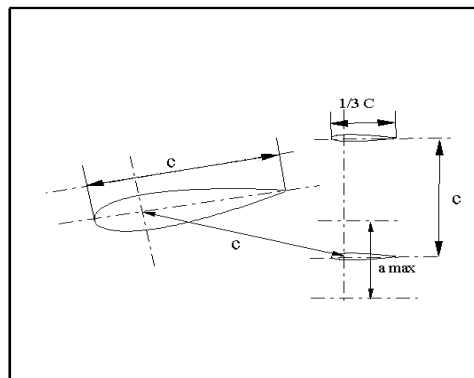


Fig.II.4. Model geometrical characteristic

Table II.1 Main geometrical features of the flapping foils model

D_{rotor} [mm]	1030
H_{rotor} [mm]	1(2Dsimulation)
Number of Principal blade (N)	2
Number of Flapping wing (N0)	6
Principal blade profile	NACA0021
Flapping wing blade profile	NACA0010
Principal blade cord C [mm]	85.8
Flapping wing cord C0	$C/3$
Spoke-blade connection	$0.25C$
Distance between flapping wing in neuter position	$1.5C$

II.6.2. Motion modeling

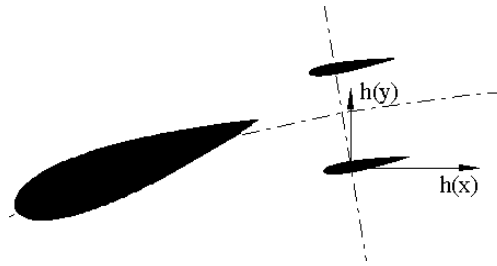


Fig.II.5. Schematic diagram for the instantaneous airfoil position

Typically for a VAWT, the blade experiences a rotating motion. Rotating motion is governed by the following equation:

$$\theta_t(t) = \theta_0 \sin\left(\omega t - \frac{\pi}{2}\right) \quad \text{II.12}$$

Where $\theta_t(t)$ is the instantaneous rotating angle. θ_0 is the blade initial azimuthal angle. The flapping motion of the backward wings is governed by the following laws:

$$h(x) = (R + a_0 \sin(zi t))^2 \cos(t) \quad \text{II.13}$$

$$h(y) = (R + a_0 \sin(zi t))^2 \sin(t) \quad \text{II.14}$$

$$\theta = cst \quad \text{II.15}$$

The system of equations represents a circle-sinusoid in cartesian system where $h(x)$ is the instantaneous airfoil position along the x axis, $h(y)$ is the instantaneous foil position along the y axis, θ is the instantaneous angular position relative to flapping foil center, a_0 the maximal amplitude of the flapping movement, R is the radius of the middle circle, $Zi = 2\pi f$ is the pulsation and represents also -relative to the middle cercle- the number of periods of sinusoids, t is the time. The flapping wings are fixed on the $c/4$ position, which yield to two degree of freedom a circular translation and a rotary oscillating around the neutral position.

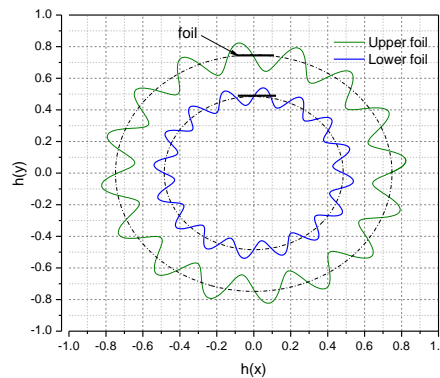


Fig.II.6. Illustration of the position axes of the two flapping foils in one revolution

II.6.3. Computational domain and boundary condition

The employed grid quality and the extent of the computational domain play an important role in the accuracy of the CFD simulation results. The problem is even more critical when the technique of dynamic mesh is used, this is attributed to the fact that the evaluation of the aerodynamic forces generated by an oscillating wing is obtained by integrating the pressure on a mobile walls.

The computational analysis type 2D or 3D is a key parameter to consider. T. Maître et al [27] outlined that 2D analysis was sufficient and able to predict the real 3D flow in the turbine. The two works of Nabavi et al [59] showed that higher blade aspect ratio $H/C = 10$ and lower chord ratio $C/R = 0.1$ to 0.2 leads to both lower 3D and unsteady effects. Authors have been proved that 2D simulations better represent the experiments. In order to allow a full development of the wake, the employed far-field is extended 37 rotor diameters upwind and 60 rotor diameters downwind (practically the same grid dimensions used by Castelli et al. [60]).

The stationary wall boundary is selected –no slip condition– for all solid boundaries. To ensure the continuity in the flow field between the fluid domains, the interface condition has been adopted. For the external borders of the fluid domain, the corresponding boundaries conditions are:

- **Outflow condition** imposed in the outlet border, which is a Newman condition, used for modeling the flow where the details about the flow velocity and pressure are not known and the outlet flow is supposed to be a fully developed flow.

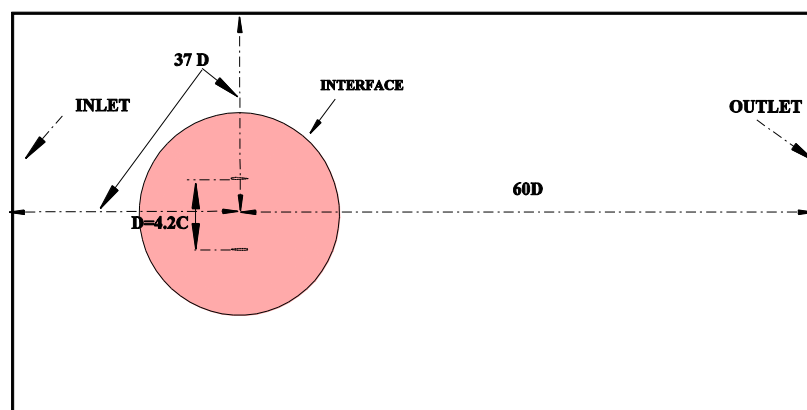


Fig.II.7. Computational domain dimension and the boundary conditions

- **Velocity inlet condition:** imposed in the inflow boundaries (Inlet, Upper and Lower borders): is a Dirichlet condition and it consists of specifying the velocity for those borders by one of the available ways in ANSYS.

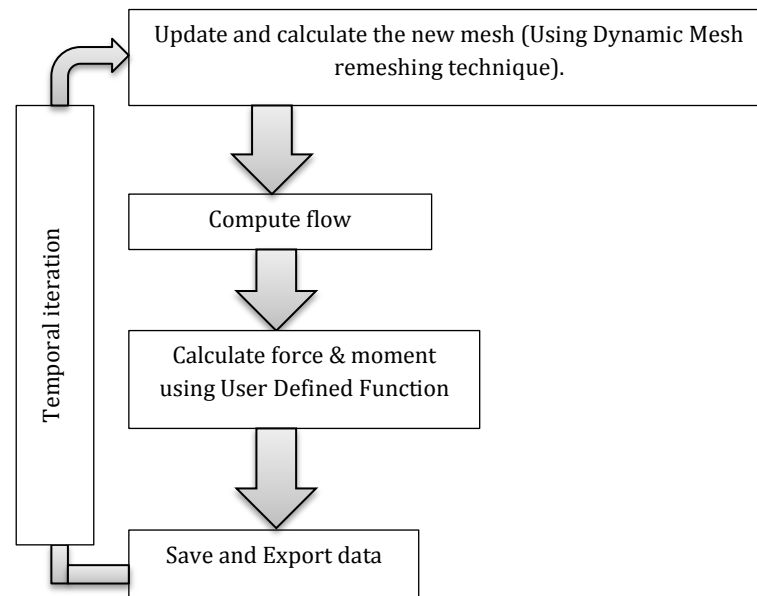


Fig.II.8. Diagram for unsteady time step.

The numerical simulation is carried out using Ansys-Fluent 15.0. The SIMPLE algorithm is used for the pressure-velocity coupling. The 3rd order MUSCL convective scheme (Monotone Upstream-Centered Schemes for Conservation Laws) is used for all transport equations discretization. It improves the spatial precision by reducing the numerical diffusion. Within a temporal iteration a User Defined Function (UDF) is adopted to control the dynamic mesh and to compute the instantaneous forces and moment for the flexible turbine blades. (Fig.II.8)

II.6.4. Meshing strategy

The adopted meshing strategy resides in the dividing of the calculation domain in five zones as it is illustrated in Fig.II.9 (a) and (b). The zone 1 contains the blade-foils sets, and is animated by a rotation motion. The zone 3 contains the flapping foils (Fig.II.9 (b)) and is meshed with triangular cells. Zone 3 is secured on the foil; this fact allows keeping the same undeforming fine mesh in the area surrounding the airfoil. The zone 3 slides inside the Zone 2. This sliding is performed through both the sliding mesh strategy and a layering technique Figs.II.10 and II.11. The entire (zone 1-3), slides in the zone 4 which is kept immobile. The equations governing the synchronized flapping motion are integrated in the User Defined

Function (UDF) in order to govern the generation and the progress of the meshing in different zones.

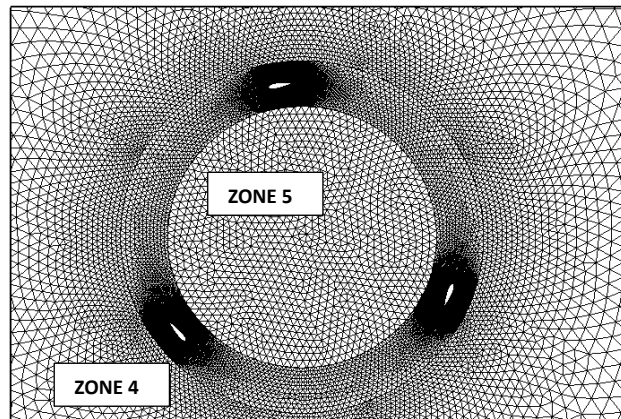
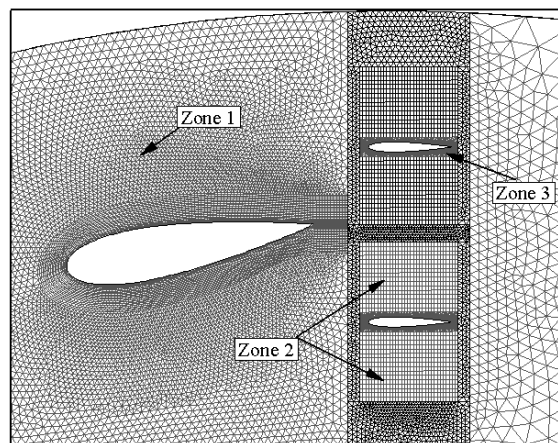


Fig.II.9. a: The different meshing zones of the proposed model



b: Zooming scale of the meshing around a blade and wings set .

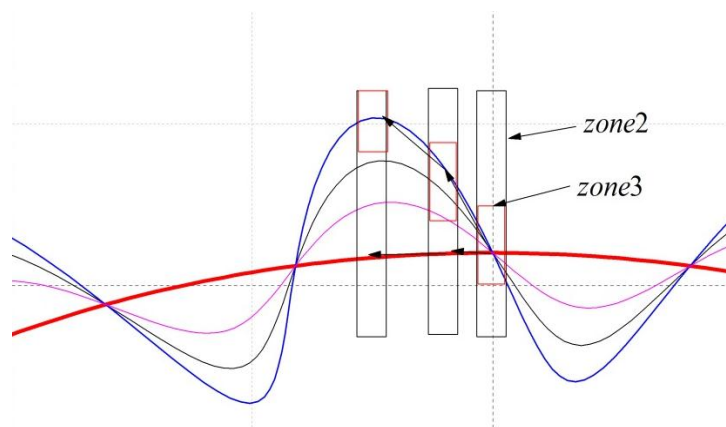


Fig.II.10. Technique of sliding mesh between zone2 and zone 3

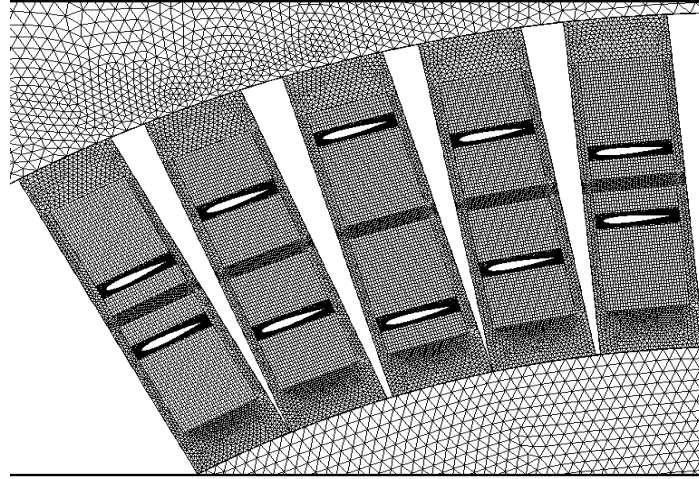


Fig.II.11. Deforming mesh between zone2, zone 3 and zone 4

To confirm that the employed grid near the wall is sufficiently fine and capable to detect all phenomena that occur near the wall, the dimensionless wall value is employed which is defined as:

$$y^+ = \frac{u_\tau \cdot y}{\nu} \quad \text{II.16}$$

where y is the distance from the wall at cell center and ν is the kinematic viscosity ($1 \times 10^{-6} \text{ m}^2/\text{s}$ for water). $u_\tau = \sqrt{\tau_w / \rho}$ is the friction velocity. $\tau_w = \mu \partial u / \partial n$ is the wall shear stress defined by the normal velocity gradient at wall.

The same mesh refinement showed by Amet et al [61] is followed .For a similar Reynolds number, using a k-w model Amet et al [61] simulated the flow around a vertical axis water turbine. The airfoils are surrounded with a finer mesh in which y^+ at the wall adjacent cell is chosen around 1, corresponding to a cell size of $25 \mu \text{ m}$.

II.6.5. Dynamic updating mesh strategy

- **Sliding mesh technique**

The sliding mesh technique lets adjacent grids to slide relative to one another. So, the grid faces do not need to be associated on the grid interface. This state requires a technique of computing the flux across the two non-conformal interface zones of each grid interface. To calculate the flux, the intersection between the interface zones is determined at each new time step. [58] The resulting intersection produces one interior zone (a zone with fluid cells on both sides) and one or more periodic zones. If the problem is not periodic, the intersection

produces one interior zone and a pair of wall zones (which will be empty if the two interface zones intersect entirely), as shown in Fig.II.12. The number of faces in these intersection zones will vary as the interface zones move relative to one another. Principally, fluxes through the grid interface are calculated using the faces resulting from the intersection of the two interface zones, rather than from the interface zone faces themselves.

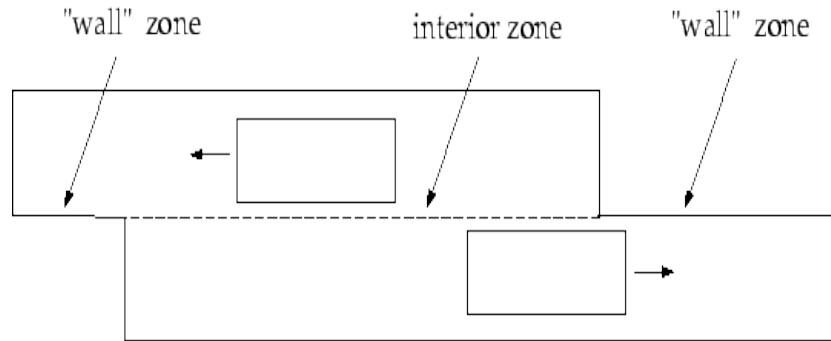


Fig.II.12. Zones created by Non-Periodic interface intersection [58].

In the example shown in Fig.II.13, the interface zones are composed of faces A-B and B-C, and faces D-E and E-F. The faces a-d, d-b, b-e, etc are generated by the intersection of these zones. Faces produced in the region where the two cell zones overlap (d-b, b-e, and e-c) are grouped to form an interior zone, while the remaining faces (a-d and c-f) are paired up to form a periodic zone. To compute the flux across the interface into cell IV, for example, face D-E is ignored and faces d-b and b-e are used instead, carrying information into cell IV from cells I and III, respectively.

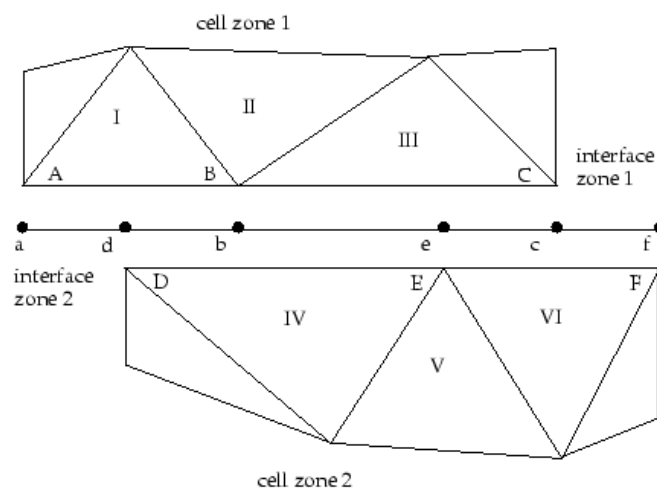


Fig.II.13. Two-dimensional grid interface [58]

- **Layering method**

The dynamic mesh strategy used in this part is the Dynamic Layering Method available in ANSYS FLUENT 15.0, which consists of adding or removing layers of cells adjacent to the moving boundary, based on its height [58].

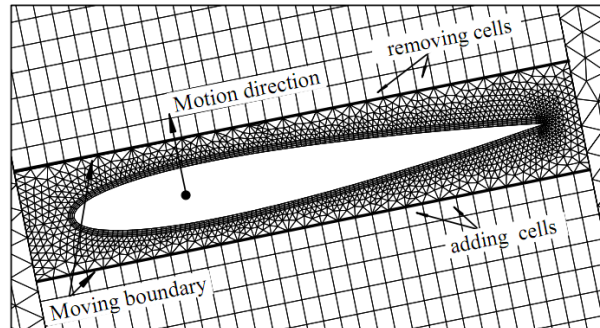


Fig.II.14. Illustration of the layering technique allowing the sliding of zone 3 in zone 2 (zone 3 is secured on the foil).

The dynamic mesh model in ANSYS FLUENT 15.0 allows us to specify an ideal layer height on each moving boundary. The layer of cells adjacent to the moving boundary (layer j in Fig II.15) is divided or merged with the layer of next cells (layer i) based on the height (h) of the cells in layer j .

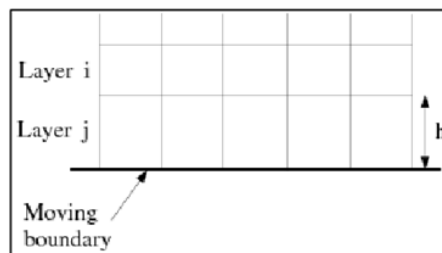


Fig.II.15. Dynamic layering method.

Once the ideal layer height (h) is specified, during the motion of the boundary FLUENT proceeds in one of those two manners: If the cells in layer j are expanding, the cell heights are allowed to increase until

$$h_{min} > (1 + a)h_{ideal} \quad \text{II.17}$$

Where h is the minimum cell height of the layer j , a is the layer split factor. When this condition is reached, the cells are splitting based on either the cell height-based or the cell ratio-based.

If the cells in layer j are compressed, the cell heights are allowed to compress until

$$h_{min} < a h_{ideal} \quad \text{II.18}$$

Where a is the layer collapse factor.

II.7. Flow control by using flexible flapping wings

II.7.1. Problem description

The proposed device consists of a vertical axis wind turbine VAWT with a NACA 0010 flexible airfoil (Fig.II.16, 17, 18).The flapping frequency is controlled relatively to the turbine axis by the number of periods of sinusoids Zi (Fig.II.19). The frequency is chosen to be close to the reduced frequency of the rotor frequency of the blades. The investigation encompasses the amplitude a_0/c from 0.1 to 0.5 and the flapping frequency parameter Zi from 2 to 4. The turbine operates at different angular velocities, for a constant incoming flow velocity of 3 m/s. The main geometrical features of the tested rotor are summarized in Table 1.

Table II.2. Main geometrical features of the flexible turbine model

D_{rotor} [mm]	440
H_{rotor} [mm]	1(2Dsimulation)
Number of blade (N)	2
Principal blade profile	NACA0010
Principal blade cord C [mm]	50
Incoming flow velocity m/s	3m/s

II.7.2. Motion modeling

For the flexure motion, the profile of the flexible airfoil is given by the following equations:

Along the x axis

$$y(t) = -\frac{a_0}{c}(x(y_f, t) - l_c)^2(\sin(\omega t + \varphi)) \quad \text{II.19}$$

And along the y axis

$$x(t) = -\frac{a_0}{c}(y(x_f, t) - l_c)^2(\sin(\omega t + \varphi)) \quad \text{II.20}$$

Where a_0 denotes the flexure amplitude and φ denotes the phase angle. $x(y_f, t)$ is the instantaneous airfoil position along the x axis, $y(x_f, t)$ is the instantaneous foil position along the y axis, and t is the time .

x_f and y_f are the local coordinates of airfoil relative to the pitching axis.

Typically for a flexible VAWT, the blade experiences a rotating motion in addition to its flexure motion. Rotating motion is governed by the following equation:

$$\theta_t(t) = \theta_0 \sin\left(\omega t - \frac{\pi}{2}\right) \quad \text{II.21}$$

Where $\theta_t(t)$ is the instantaneous rotating angle. θ_0 is the blade initial azimuthal angle
Relative to the turbine center, the instantaneous deflections of the airfoil along the x and y axes are defined by:

$$x(y_f, t) = a_t(y) \sin(\omega t + \varphi) \quad \text{II.22}$$

$$y(x_f, t) = a_t(x) \sin(\omega t + \varphi) \quad \text{II.23}$$

Where $x(y_f, t)$ is the instantaneous airfoil position along the x axis. $y(x_f, t)$ is the instantaneous airfoil position along the y axis. x_f and y_f are the local coordinates of airfoil relative to the pitching axis. $a_t(x)$ and $a_t(y)$ are the deflection amplitudes along the x axis and the y axis respectively.

For a blade with flexible trailing edge, the deflection amplitudes are then given by:

$$a_t(x) = -(c - l_c) * \left(\frac{x}{(c-l_c)} - R * \cos(\theta_t)\right)^n * a_0 \quad \text{II.24}$$

$$a_t(y) = -(c - l_c) * \left(\frac{y}{(c-l_c)} - R * \sin(\theta_t)\right)^n * a_0 \quad \text{II.25}$$

Where a_0 denotes the foil displacement at the trailing edge as shown in figure 2 , φ denotes the phase angle, R the turbine radius, c the blade chord, l_c the pitching center and n the flexibility coefficient.

For a blade with camber deformation, the deflection amplitudes are then given by:

For $x > R * \cos(\theta_t)$:

$$a_t(x) = -l_c * \left(\frac{x}{l_c} - R * \cos(\theta_t)\right)^n * \sin(zi(t)) \quad \text{II.26}$$

$$a_t(y) = -l_c * \left(\frac{y}{l_c} - R * \sin(\theta_t)\right)^n * \sin(zi(t)) \quad \text{II.27}$$

And for $x < R * \cos(\theta_t)$:

$$a_t(x) = -(c - l_c) * \left(\frac{x}{(c-l_c)} - R * \cos(\theta_t) \right)^n * a_0 \quad \text{II.28}$$

$$a_t(y) = -(c - l_c) * \left(\frac{y}{(c-l_c)} - R * \sin(\theta_t) \right)^n * a_0 \quad \text{II.29}$$

The dynamic Remeshing technique has been used; the selected parameters are summarized in Table II.3.

Table II.3 dynamic mesh parameters

Minimum length scale	0.0001
Maximum length scale	0.0005
Maximum cell skewnesse	0.67
Size remeshing interval	6
Spring constant factor	0.3
Boundary node relaxation	1
Convergence tolerance	0.001

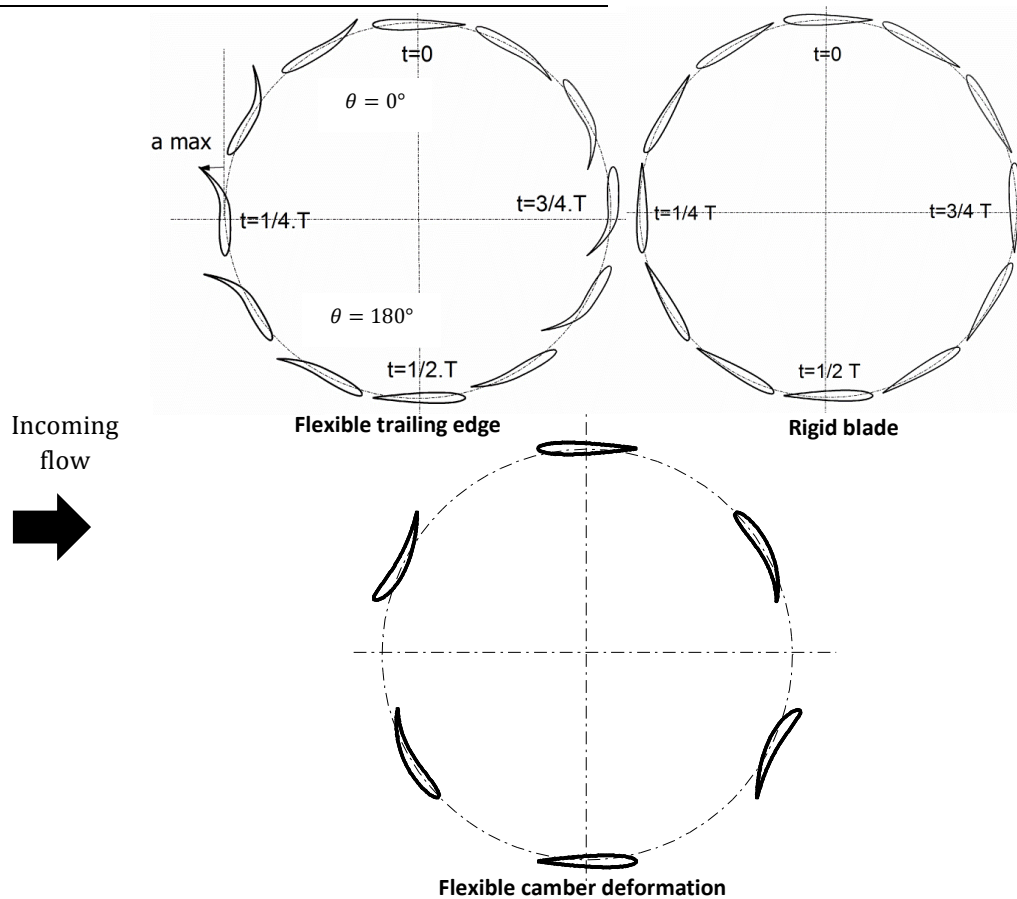


Fig.II.16. Model geometrical characteristics (T: turbine revolution t: time)

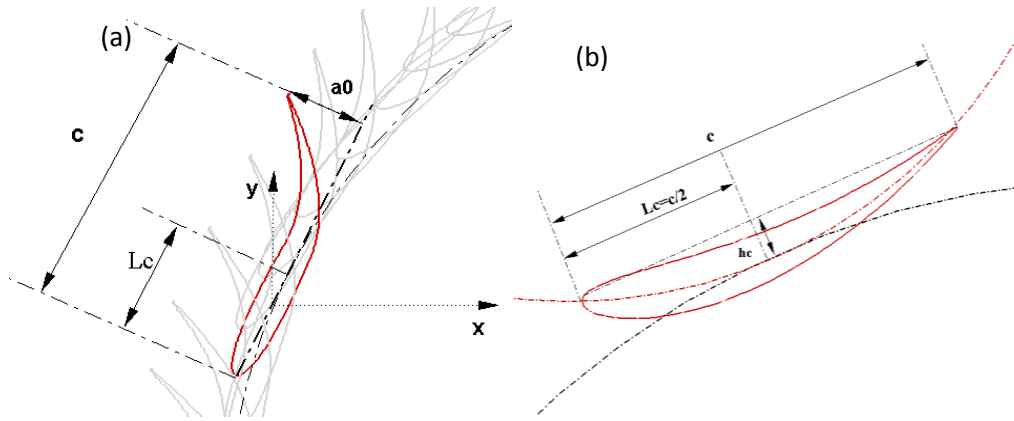


Fig.II.17. Schematic diagram of the deforming turbine blade (a) flexible trailing edge (b) camber deformation

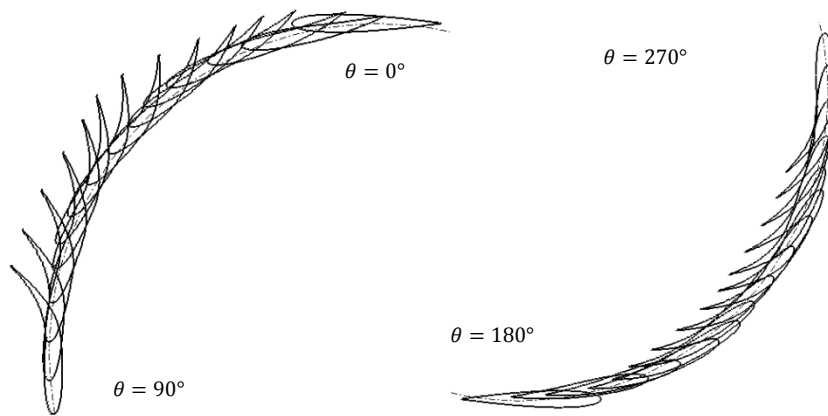


Fig.II.18. Flexible airfoil deformation for (zi=4)

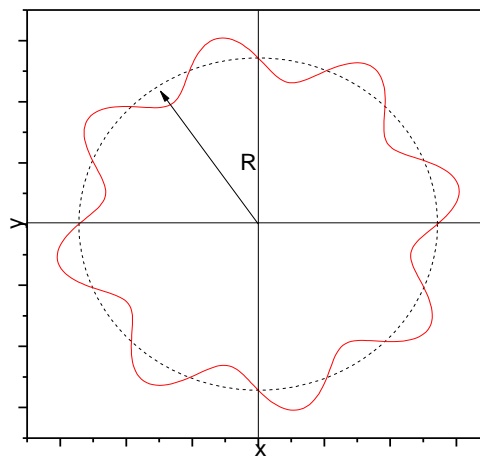


Fig.II.19. Flexure motion trajectory for zi=8

II.7.3. Meshing strategy

The adopted meshing strategy resides in the dividing of the calculation domain in two zones as illustrate in **Fig.II.20**. The zone 2 contains the blade-foils sets, and is animated by a rotation motion. The zone 1 is a fixed zone meshed with a triangular cell. The zone 2 slides inside the Zone 1.

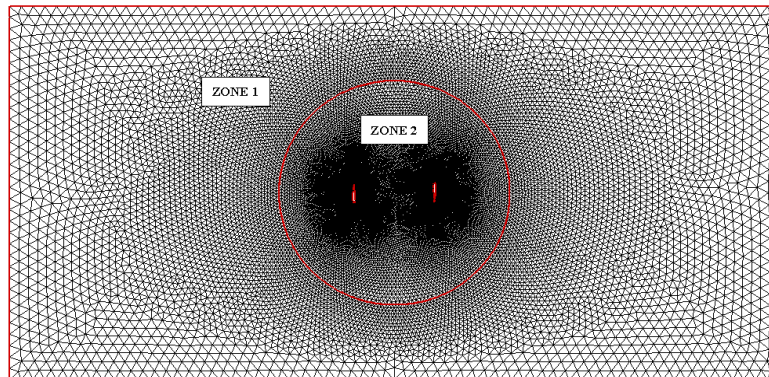


Fig.II.20. Simulation domaine zones

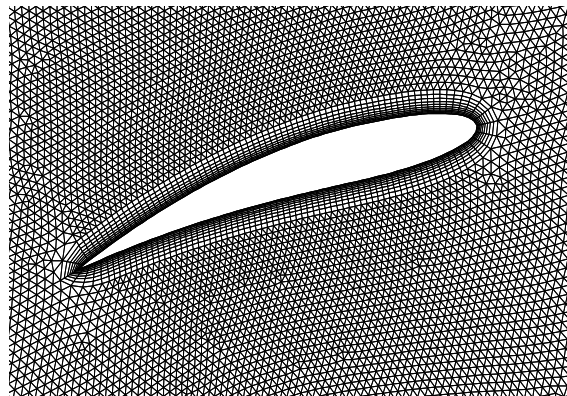


Fig.II.21. Zooming scale of the mesh around the flexible blade

II.7.4. Dynamic updating mesh strategy

- **Spring-Based smoothing**

For spring-based smoothing, the edges between any two mesh nodes are idealized as a network of interconnected springs [58]. The initial spacing of the edges before any boundary motion constitutes the equilibrium state of the mesh. A displacement at a given boundary node will generate a force proportional to the displacement along all the springs connected to the node.

- **Re-meshing method**

On zones with a triangular or tetrahedral mesh, the spring-based smoothing method (described in Spring-Based Smoothing) is normally used. When the boundary displacement is large compared to the local cell sizes, the cell quality can deteriorate or the cells can become degenerate. This will invalidate the mesh (e.g., result in negative cell volumes) and consequently, will lead to convergence problems when the solution is updated to the next time step. To circumvent this problem, ANSYS FLUENT agglomerates cells that violate the skewness or size criteria and locally remeshes the agglomerated cells or faces. If the new cells or faces satisfy the skewness criterion, the mesh is locally updated with the new cells (with the solution interpolated from the old cells). Otherwise, the new cells are discarded.

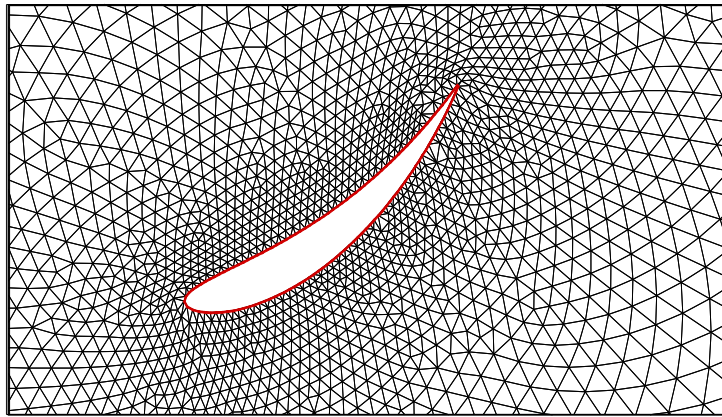


Fig.II.22. Dynamic re-meshing method

II.8. Conclusion

In this chapter, the suggested models to control the flow over vertical axis wind turbines VAWT's are exposed. Then, we present both the flexible and the backward flapping-wings motions. The two dynamic mesh strategy's that used in the present study are showing. The layering method consists of adding or removing layers of cells adjacent to the moving boundary, based on its height. In Re-meshing method the edges between any two mesh nodes are idealized as a network of interconnected springs. A displacement at a given boundary node will generate a force proportional to the displacement along all the springs connected to the node.

CH.III. RESULTS AND DISCUSSION

III.1 Introduction

To produce clean and renewable energies, wind and tidal flows were the most used sources. Till now this field is dominated by the rotary machines. Due to its simple design and its easy installations, the vertical axis wind turbine (VAWT) is one of the most promising devices. However, its efficiency still relatively low compared to horizontal axis turbines.

Ordinarily, the conventional VAWT has a rigid blade, this simple design resulting in low energy extracting efficiency due to the stall that occurs at a large flow angle of attack. This fact has stimulated and encouraged the researchers to make improvements and to develop new control methods to bring closer their efficiency nearly to the one of the horizontal axis turbines. Evaluating from the fluid analysis perspectives, the dynamic stall is responsible, not only of the efficiency's dropping, but also responsible in structural vibrations and acoustic noises. To cover this gap, a set of flow's control techniques have been developed in which they can be classified in; passive control techniques or active control techniques.

In this chapter, firstly, a rigid blade vertical axis turbine (original turbine) is simulated.

Secondly, an actively deformable flexible blade is studied. Different forms of flexible blades are investigated which are:

- A blade with flexible trailing edge
- A blade with camber deformation

Also, vertical axis wind turbine having two backward flapping wings is considered.

III.2. Simulation of the flow across a vertical axis wind turbine (rigid blade)

Firstly, the case without control is presented to highlight the natural phenomena that occur during the rotation of the turbine especially the dynamic stall phenomena. The investigation is carried as a two-dimensional (2D) simulation, several authors [27],[61] were shown that a two-dimensional simulation is able to properly predict the performance of the machine when providing some simulation criteria (fine mesh, the appropriate turbulence model).

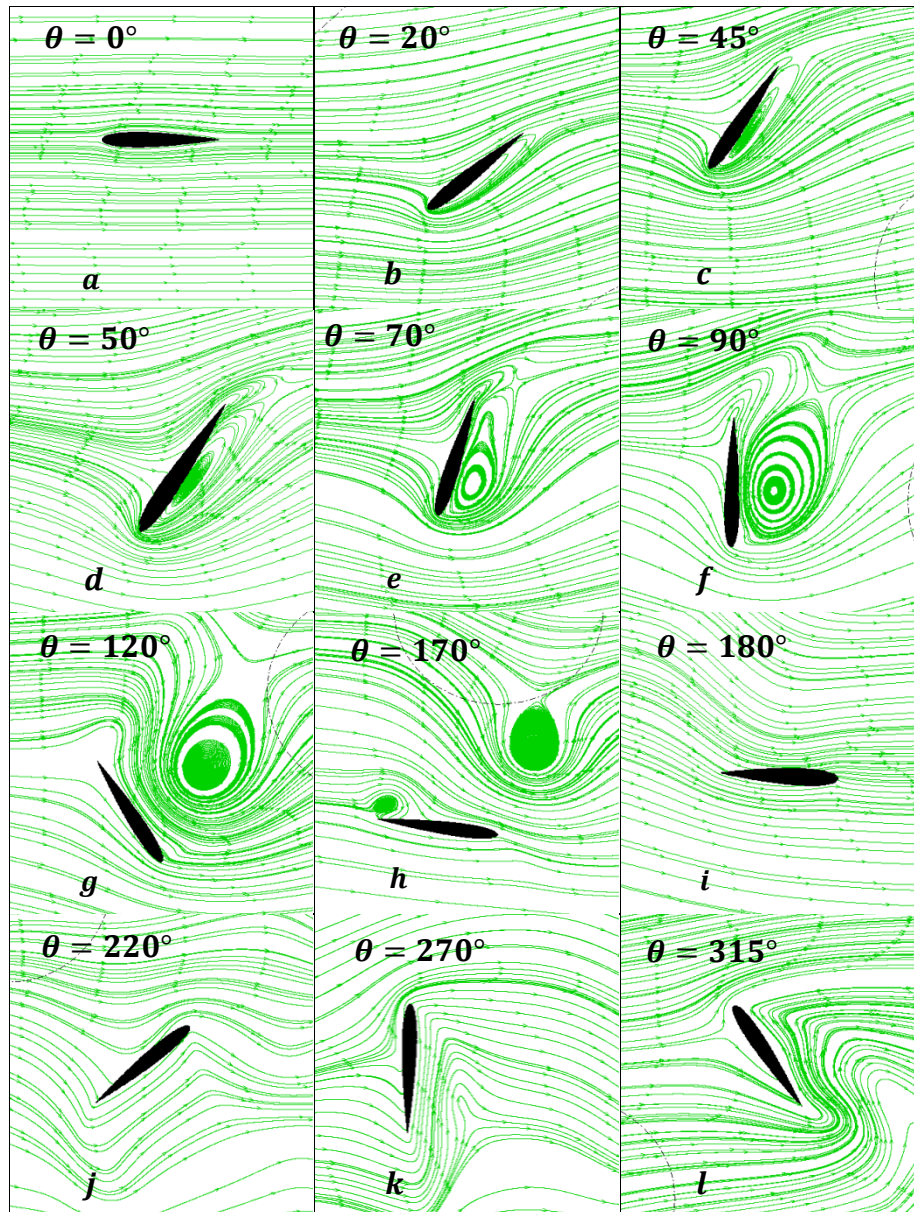


Fig.III.1 Flow field around a VAWT blade in one revolution.

To understand the mechanism by which the turbine harvest energy and how do the interactions between the blades and the incoming flow affect the turbine performance, general descriptions of the fluid structures interactions and the main vortices trajectories inside the turbine are represented as a function of the blade azimuthal position.

In general, large vortices of the size of the blade have been detected during the rotation of the turbine. From Fig.III.1 it can be seen an attached flow at azimuth position $\theta = 0^\circ$. When the effective incidence angle increases with azimuth angle (Fig.III.2) typically the flow begins to separate at the trailing edge for an azimuth position $\theta = 20^\circ$. Then the separation point travels toward the leading edge forming a recirculation zone at suction surface and the blade is in a mild stall. Once the azimuth angle passes 30 degrees, the vortex grows rapidly with the increase of azimuth angle, and the lift coefficient increases proportionally to the angle of attack during this development (Fig.III.4).

For an azimuth position between $\theta = 30^\circ$ and $\theta = 60^\circ$, the detached vortex keeps growing and interacts with a new growing vortex at the trailing edge, leading to an important energy dissipation, which affects the lift coefficient that grows nonlinearly. When the blade moves toward an azimuth angle $\theta = 70^\circ$, the vortex growth up and begins to leave the blade surface and the blade be in a deep stall, which drops suddenly the lift coefficient. The peak of the lift coefficient is registered at $\theta = 70^\circ$. At $\theta = 90^\circ$, a secondary vortex is formed at the trailing edge, which contributes positively in the increase of the aerodynamic forces during the down-stroke motion. From Fig.III.2, for all values of tip speed ratio λ , the incidence angle develops symmetrically relative to a given azimuth angle. So increasing the azimuth angle, the angle of attack begins to decrease after $\theta > 120^\circ$. For this angle, the induced vortex sheds from the blade suction surface and transferred in the near wake, then, the flow becomes attached when the blade comes to azimuth angle of 180 degrees.

At the downstream, the depression conveyed from the pressure side of blade to the suction side (Fig.III.6) and the angle of attack began to increase ($\theta > 220^\circ$) see Fig.III.2. Therefore a reversed flow occurs at the trailing edge, which increases significantly the drag force (Fig. III.3). The peak of the drag coefficient in the down-stroke motion is about 50% of that in the up-stroke motion. This behavior is attributed to the fact that the performance of a VAWT turbine rotor is exposed to common aerodynamic interaction between the blades. The common aerodynamic interactions are due to the wakes produced by the blades (Fig. III.5). Which is a function of air flow incident and solidity of the turbine.

From Fig.III.1, it can be determined that the blade has practiced four stages: attached flow, minor stall, deep stall, and reattached flow. The trailing edge flow separation creates mild or minor stall, and the entire shedding of the leading edge vortex entered the blade in a deep stall and the lift coefficient reaches its peak value.

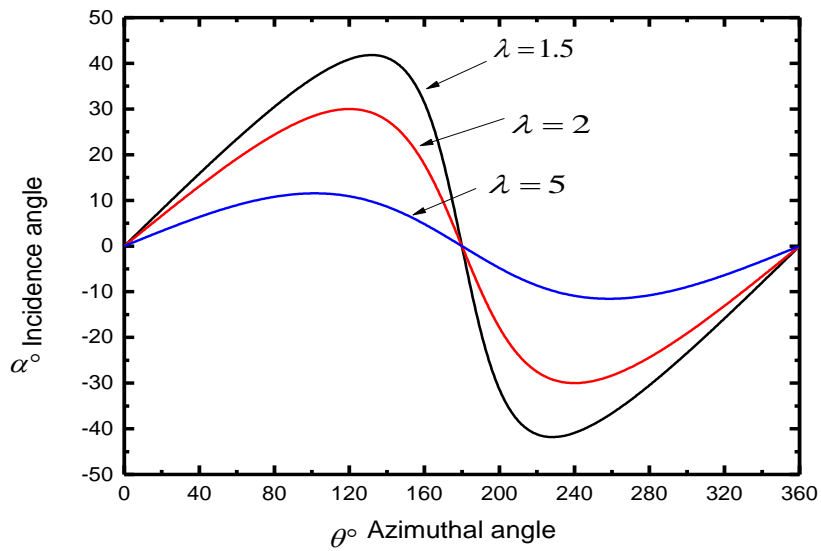


Fig.III.2. Flow incidence α° versus the blade position θ° for several tip speed ratios λ .

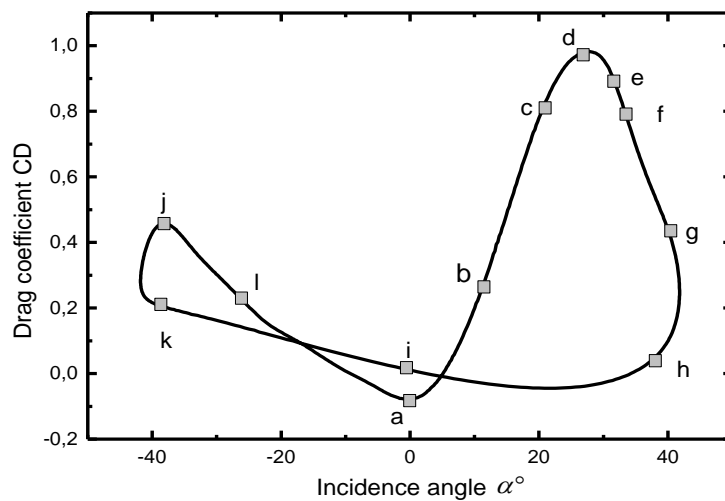


Fig.III.3. Instantaneous drag coefficient against the incidence angle α° .

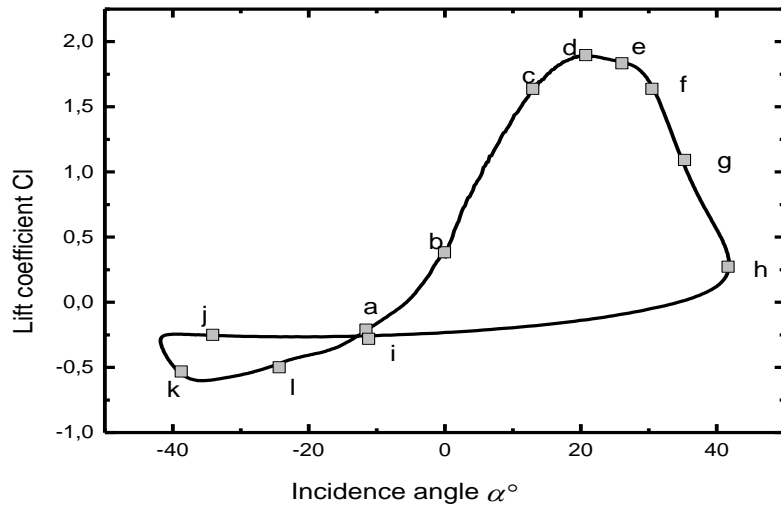


Fig.III.4. Instantaneous lift coefficient against the incidence angle α° .

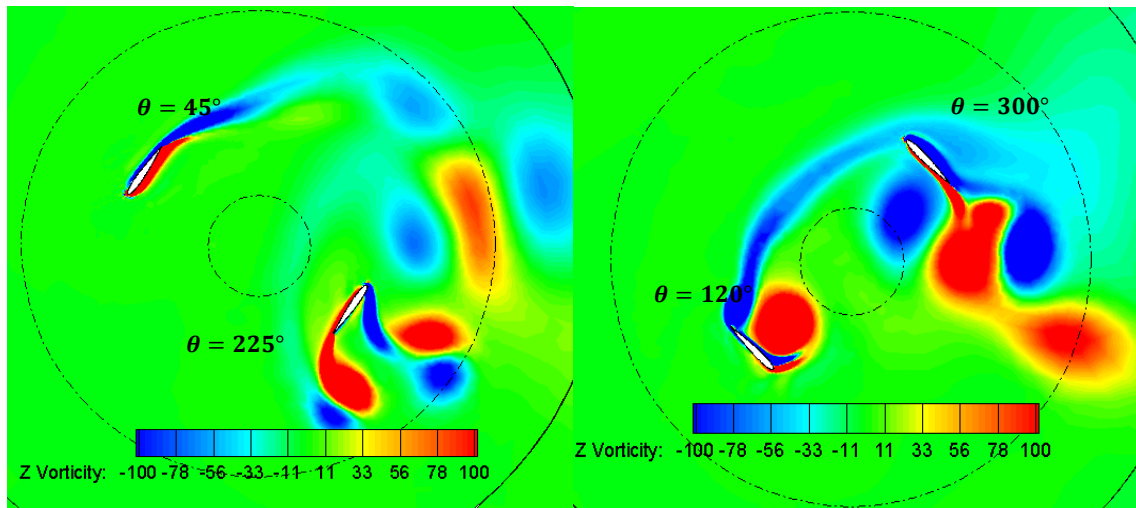


Fig.III.5. Downstream wakes contours at $\lambda = 1.4$.

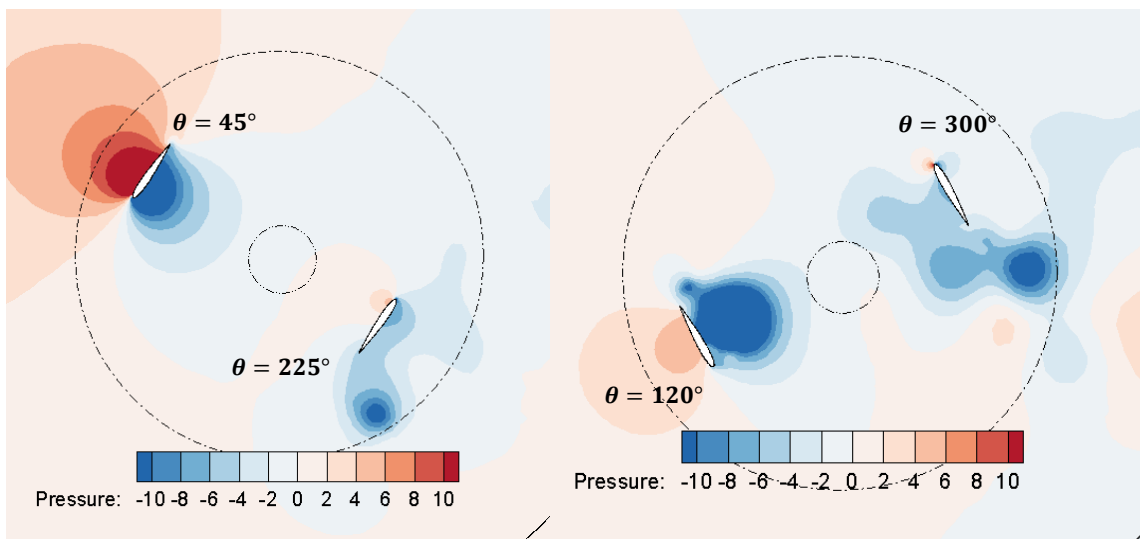


Fig.III.6. Pressure contours at $\lambda = 1.4$.

III.3. Flow control by using flexible blades

In this section, the effect of a blade with flexible trailing edge on the VAWT performance is examined. The mechanism is inspired from the vortex control mechanism, utilized by certain aero-/aqua- animals to improve their propulsion performance via their fins. The flexible blade is designed to move regularly around a fixed axis aiming to control the flow near the blade boundary layer and the vortex interaction between blades.

III.3.1. Model validation

To validate the model under study, a flexible wing in plunging motion studied by Miao et al. [46] is simulated (Fig.III.7). In their investigation, for various Reynolds numbers and reduced frequencies, a systematic parametric study is performed on the effect of chord-wise flexure amplitude on unsteady aerodynamic characteristics of single flexible airfoil in plunge motion. Fig.III.8 shows the variation of instantaneous drag coefficient for a reduced frequency $\frac{2\pi fc}{U_\infty} = k = 2$, non-dimensional plunge amplitude $h_0 = 0.4$, and Reynolds number $Re = 10^4$. Results show that a negative drag is observable. This thrust force that is locally generated in the near wake corresponds to a reverse Kármán vortex street as it is frequently observed in fish-like locomotion and flapping wing flight. It is obvious that the results obtained with the current solver compare well with those of Miao et al [46]. Therefore, it can be concluded that the current solver can be used for the present investigation.

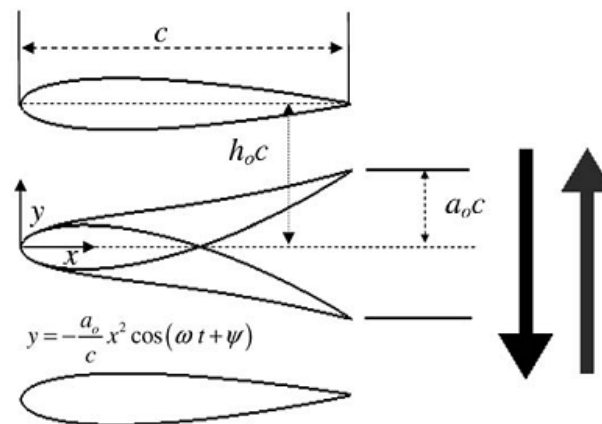


Fig.III.7. Plunge and deflection motion of single flexible airfoil [46].

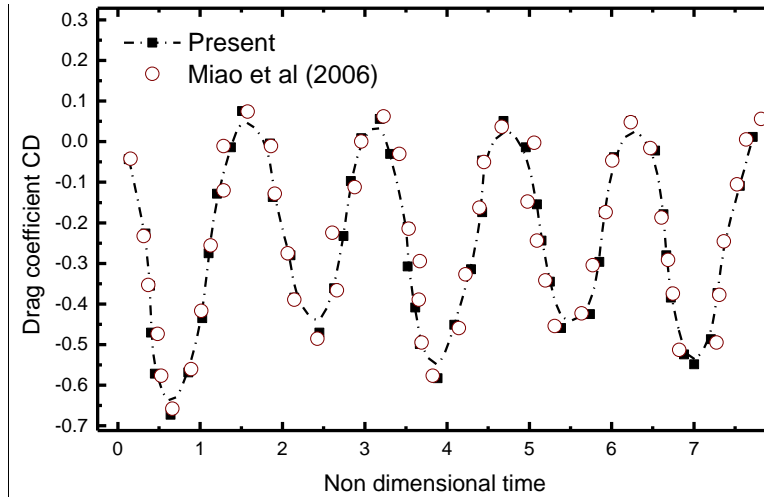


Fig.III.8. Validation of computational model, compared to publish results.

For best prediction of the turbine blade instantaneous momentum coefficient, the mesh size dependence test (Fig.III.9) is performed for several grids of increasing density ranging from about 80,000 up to 160,000 cells. The test confirms that a grid that contains about 142,000 cells can predict accurately the momentum coefficient and the fluid fields, this grid is used for all simulation following cases. After a time-step size test, a constant time-step equal to 10^{-4} s is considered.

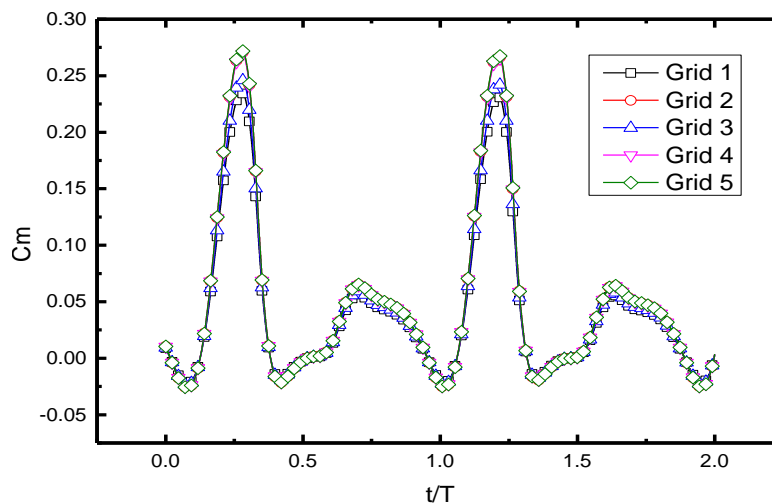


Fig.III.9. Instantaneous momentum coefficient for several grids

III.3.2. Mechanism of turbine performance improvement

It is well known that the flexibility of flapping wings can obviously provide an improved energy extraction performance which can never be achieved with rigid wings.

To examine the mechanism by which the flexible wings influence the turbine performance a comparison between rigid blade turbine and flexible blade turbine in term of instantaneous blade lift coefficient, torque coefficient and pressure distribution is carried out. Fig.III.10 (a)

and (b) show respectively the instantaneous moment coefficients and the instantaneous blade lift and drag coefficients against time. As can be seen the flexible blade generates a larger lift and drag coefficients against time. As can be seen the flexible blade generates a larger lift and momentum than the rigid ones. The lift peak increases from 1.85(rigid) to 3 (flexible) and momentum peak from 0.25 (rigid) to 0.4 (flexible). This behavior is attributed to the mechanism of leading/trailing edge vortices stability and shedding (Nakata [62], Liu et al [63]). It is generally accepted that a wing with a flexible trailing edge can boost the size and the strength of leading edge vortex (LEV). When the LEV growth a suction zone is simultaneously formed which typically increases the pressure difference between the foil upper and lower surfaces. Thus, the power extraction efficiency can be improved by increasing the peaks of lift and moment coefficients.

Fig.III.11. displays the pressure contours for the rigid and the flexible blade at two azimuthal position $\theta = 45^\circ$ and $\theta = 240^\circ$. As can be seen a significant pressure difference between original and controlled turbines occurs near the leading edge. In which the largest negative value is displayed by the flexible controlled turbine, this is attributed to the boosting of the size and strength of LEV (Fig.III.12) which ensures a source of suction zones that can effectively improve lift and momentum forces. Note that the blade lift force is due to the difference in pressure between the blade's upper and lower surface. For all lift-type turbines the enhancement of the blade lift force means an augmentation of the turbine torque and therefore, an improvement of energy extraction performance.

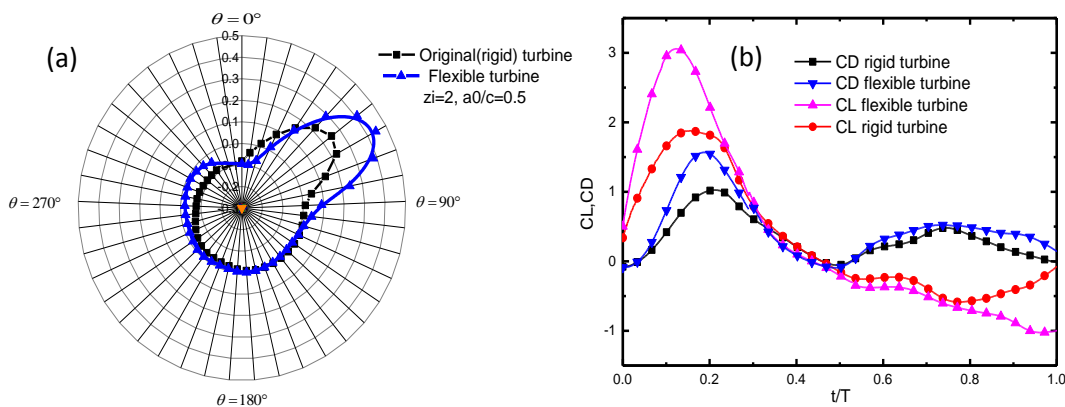


Fig.III.10. Comparison of (a) instantaneous moment coefficients and (b) instantaneous blade lift and drag coefficients against time for different blade turbines.

Fig.III.13 illustrates the downstream wakes contours for both cases; original and flexible configurations. It is seen that for the original turbine large vortices appear in the downstream wake and by consequence the generated wakes by previous blade interfere with the next one,

which compromises the turbine efficiency. However, for the controlled turbine, the flapping flexible foils prevent the development of large vortices by giving rise to small size vortices in their wake.

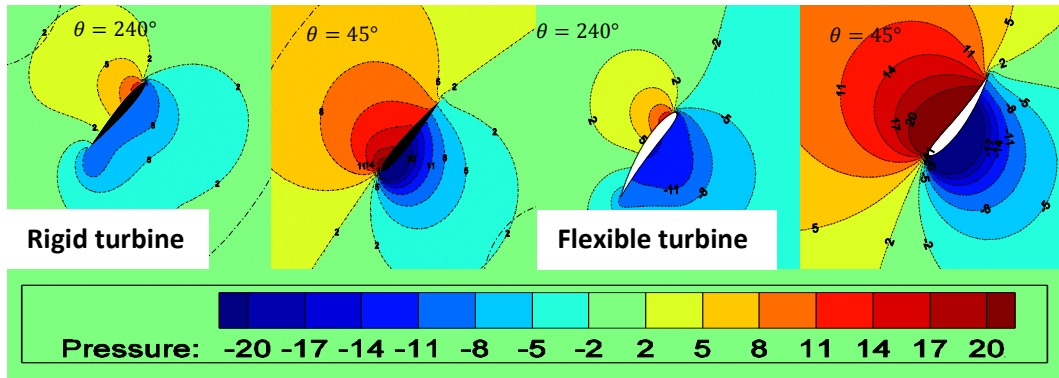


Fig.III.11. Comparison of blade surface pressure coefficient distributions at $\lambda = 1.4$ with $a_0/c=0.1$ $z_i=2$.

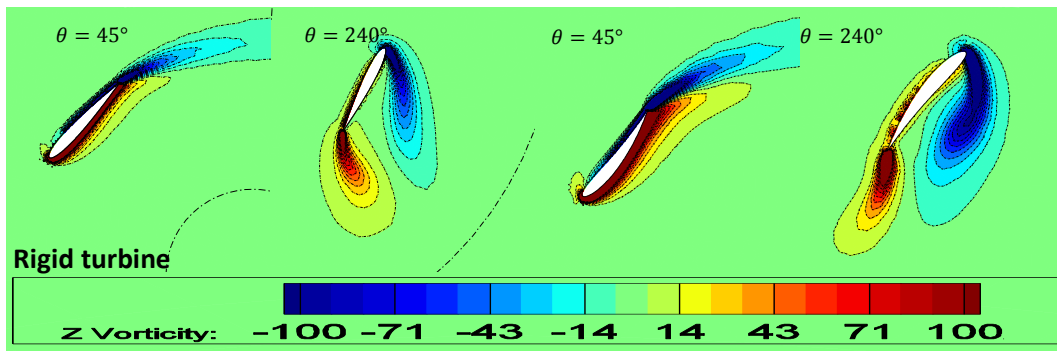


Fig.III.12. Comparison of instantaneous vortex contours at $\lambda = 1.4$ with $a_0/c=0.1$ $z_i=4$.

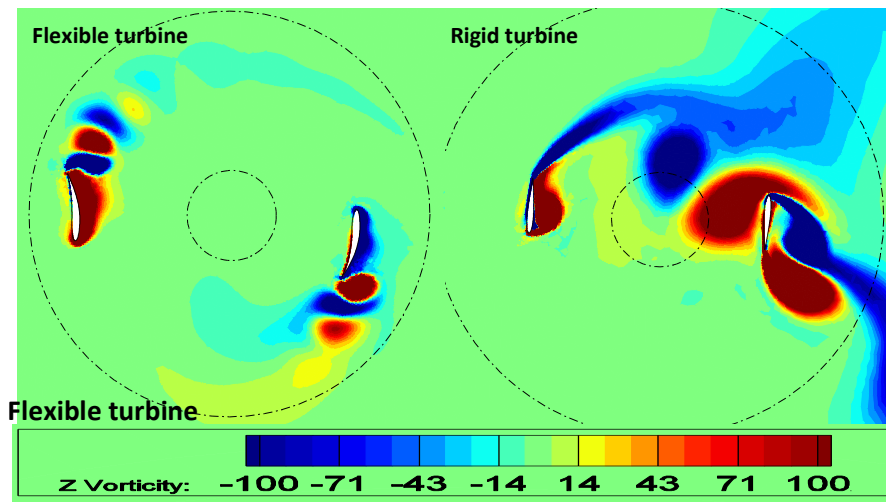


Fig.III.13. Comparison of downstream wakes contours at $\lambda = 1.4$ with $a_0/c=0.1$ $z_i=4$.

III.3.3. Deflection phase effect:

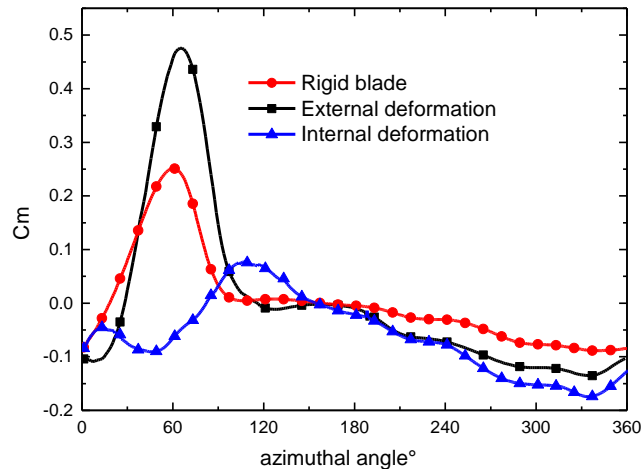


Fig.III.14. Instantaneous momentum coefficient for different blade turbines.

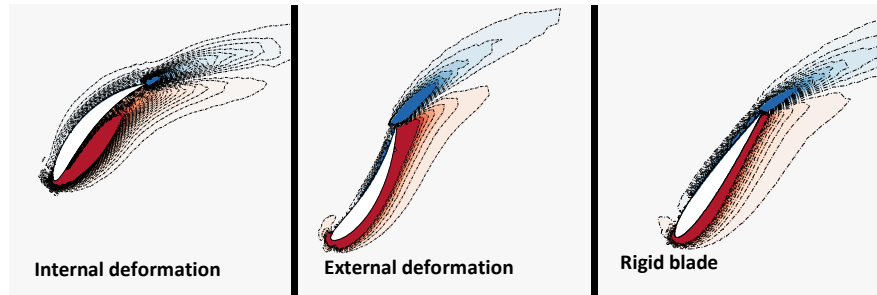


Fig.III.15. Comparison of instantaneous vortex contours at $\lambda = 1.4$ with $a_0/c=0.1$ $z_i=2$.

As it is mentioned previously, the boosting of the size and strength of LEV ensures a source of suction zones that can effectively improve lift and momentum forces. Typically an internal deformation generates a smaller LEV and therefore a smaller suction zone than rigid blade (Fig.III.15), which affects negatively the turbine performance. For the comparison among three turbines tested. It is seen that, the turbine blade with external deformation reaches a maximum momentum coefficient among three turbines (Fig.III.14). This is attributed to the change in the flow angle of attack. Examination of the vortices contour associated with the internal deformation case indicates that a vortex sheds without attached to the blade suction surface, which leads to a deep stall interpreted by a drop in the torque coefficient (Fig.III.14). After a preliminary comparison between original and controlled turbine, a systematic parametric study is further conducted.

III.3.4. Output power

The examination of the effect of varying flapping frequency and flexure amplitude on energy extraction efficiency is carried out for a frequency controlled parameters ranging between

$z_i = 2$ and 8 , and a plunging amplitudes of $a_0/c = 0.1$ to 0.5 , for a tip speed ratio between 0.6 and 1.9 .

• **Oscillating frequency effect**

The effect of oscillating frequency on the time distribution of moment coefficient C_m , power coefficient C_P , lift coefficient C_L and drag coefficient C_D is shown in Figures.III.16 (a) to (c). As it can be seen from this figures, for all tested cases the peak moment coefficient is registered at the first quarter of the turbine, which means that the most of energy is harvested between azimuthal coordinates 0° and 90° . Excepting the case $z_i = 8$, all controlled cases create a higher moment peaks with a clear contrast in the case $z_i = 4$. for the case $z_i = 8$, the C_L, C_D and C_P curves display multiple peaks with a smaller amplitudes due to the mechanism of vortex shedding caused by the blade deformation. For the other flexible turbine cases, all curves have the same trends as those of rigid blade case. However, a higher peak is registered for the flexible turbines. For the case $z_i = 2$ The peak C_P increases from 2.5 to 4.2 , the C_L, C_D and C_m peaks increase respectively from 1.8 to 3 , 1 to 1.6 and 0.25 to 0.4 . This behavior is attributed to the control of LEV strength as compared to rigid blade.

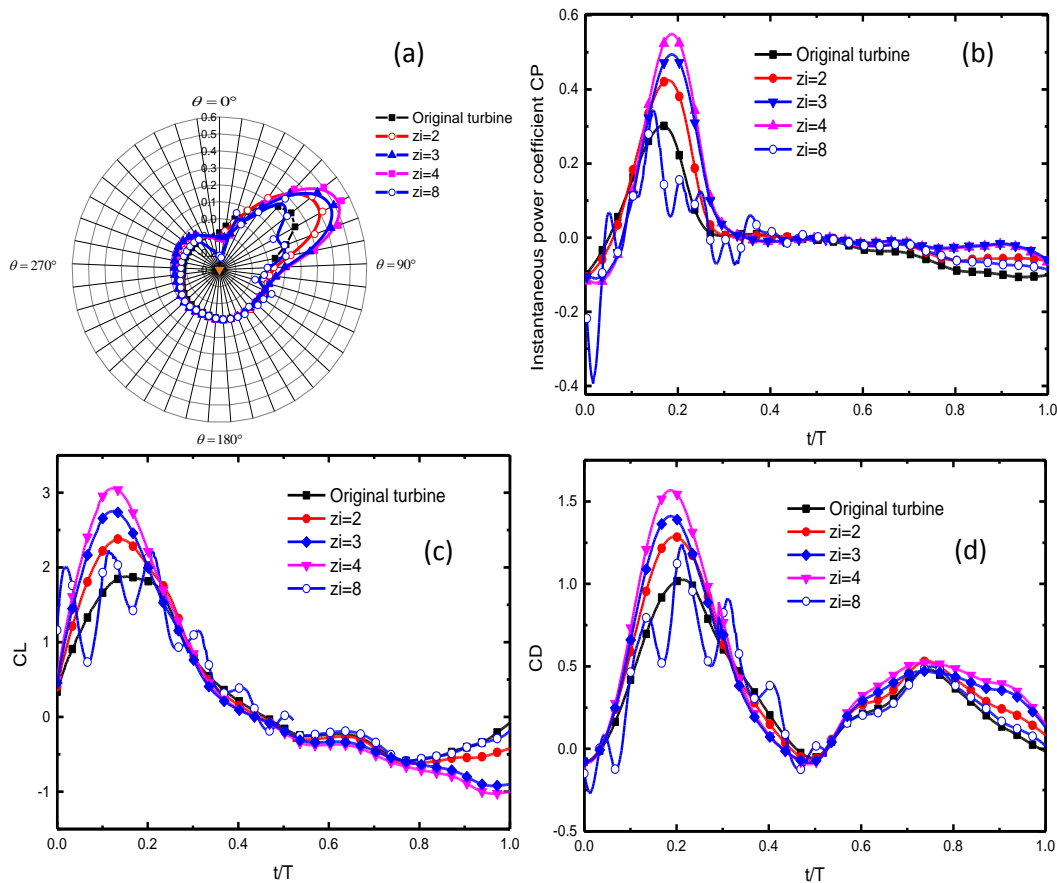


Fig.III.16.(a) Instantaneous blade moment coefficient versus θ .(b) Instantaneous power coefficient .(c) Instantaneous lift coefficient .(d) Instantaneous drag coefficient.

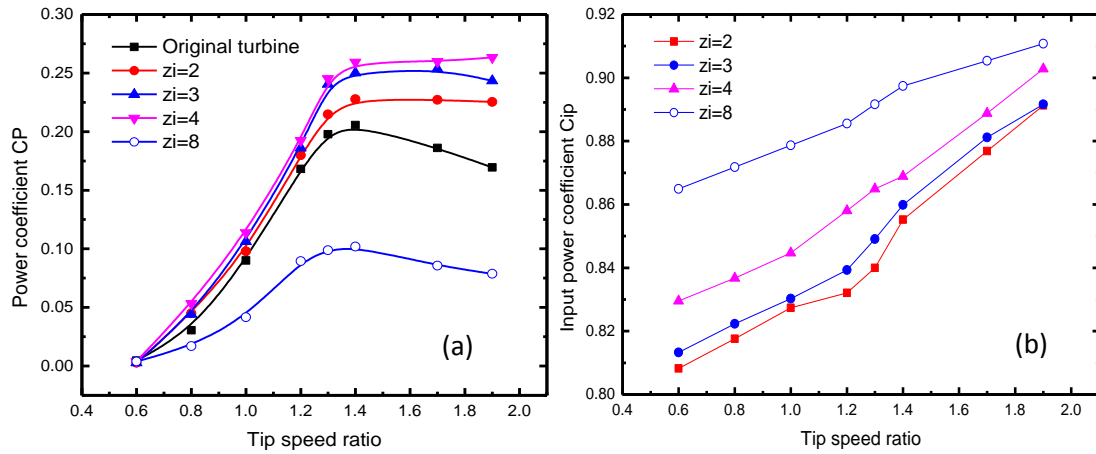


Fig.III.17.(a) Time-averaged power coefficient versus λ .(b) Time-averaged input power coefficient versus λ

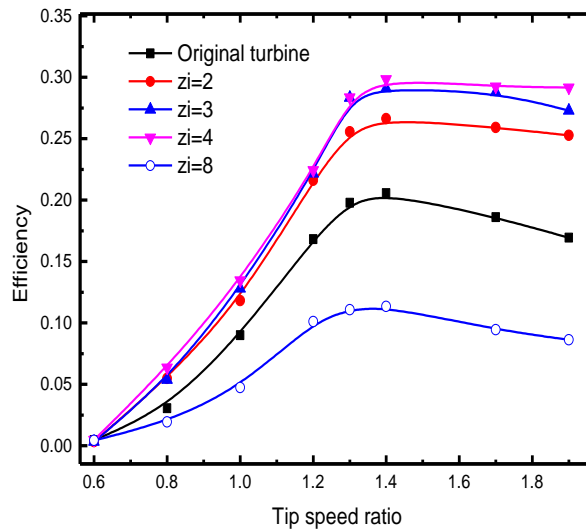


Fig.III.18.Time-averaged efficiency coefficient versus λ .

The effect of varying flapping frequency on the mean power coefficient is shown in Fig.III.17 (a). Taking a closer look at power coefficient curves, it can draw the common features: for low tip speed ratio $\lambda < 1.2$, the power coefficient CP is represented by a quasi-linear evolution until a critical point which represents Cp_{max} , and next it decays with the further increasing of tip speed ratio. For all $\lambda > 1.2$, the foil oscillating with $z_i = 4$ produces much higher CP . The maximum power coefficient is 0.2764 which is about 38.2% times that of original turbine.

It can be found that with this strategy of control a wider range of high power coefficient is feasible. For the turbine efficiency improvement, the use of high flexure frequency $z_i=8$ performs worse than that of rigid blade. A drop of about 50 % in the output power coefficient is registered. This behavior is due to the change in the flexion direction that has been

discussed in the section III.3.3. This indicates that this case is not useful as compared to the conventional rigid turbine. Typically, the efficiency improvement is obstructed by an increase in input power. Fig.III.17 (b) displays the variation of the average input power coefficient with tip speed ratio for different cases. It can be noted that the input power coefficient tends to increase with the rise of tip speed ratio values for all cases. Fig.III.18 shows that the efficiency curves have the same behavior as that of power coefficient. To check the effect of flapping frequency on the flow structures interactions, Fig.III.19 depicts a comparison of instantaneous vortex contours for the case $z_i=16$ and $z_i=4$ (note that the case $z_i=16$ is not offered in the previous results, it is a case that simulated only to show the flow structures interaction).

For the case $z_i=16$ it is seen that the large vortices that is frequently obtained in the rigid blade turbine are breakdown due to the high flexure motion, which weakens the mutual interaction between blades. In spite of this advantage, this case has a lower efficiency due to the fact that the blade experience a suddenly change in the direction of deformation which causes a serious loss in pressure and therefore a loss in the lift and momentum forces.

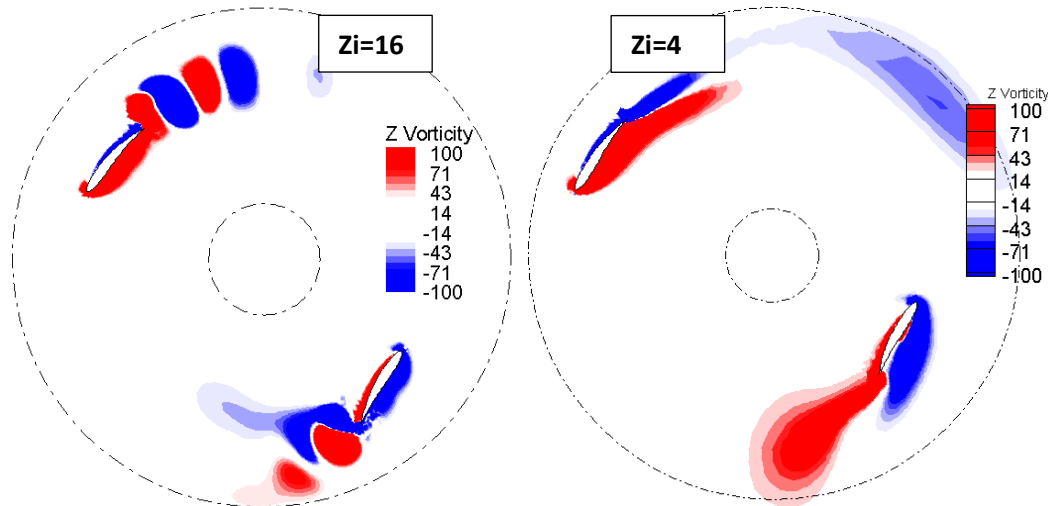


Fig.III.19. Comparison of instantaneous vortex contours at $\lambda = 1.4$ with $a_0/c=0.1$.

- **Oscillating amplitude effect**

For a frequency controlled parameter $z_i = 4$, the effect of oscillating amplitude is considered. It is seen that a similar trends as those of rigid blade are registered for the quantities C_m , C_P , C_L and C_D (Fig.III.20). The maximum instantaneous C_m coefficient is 0.41 which is about 64% times that of the original (rigid) turbine. Taking a look to the instantaneous power coefficient shown in Fig.III.20 (b), an increase of 40% C_P , as compared to the original

turbine, is possible with both oscillating amplitudes $a_0/c = 0.5$ and $a_0/c = 0.3$. This behavior is attributed to the fact that for a frequency controlled parameter $z_i = 2$, the maximum flexure amplitude is achieved at the second quarter of the turbine, which is a region of post stall. Thus the entire enlargement of the LEV is done but delayed. And the increase of flexure amplitude from $a_0/c = 0.3$ to $a_0/c = 0.5$ is not sufficient for the turbine improvement. To achieve a best performance, large oscillating amplitude must be chosen with which the LEV is effectively controlled.

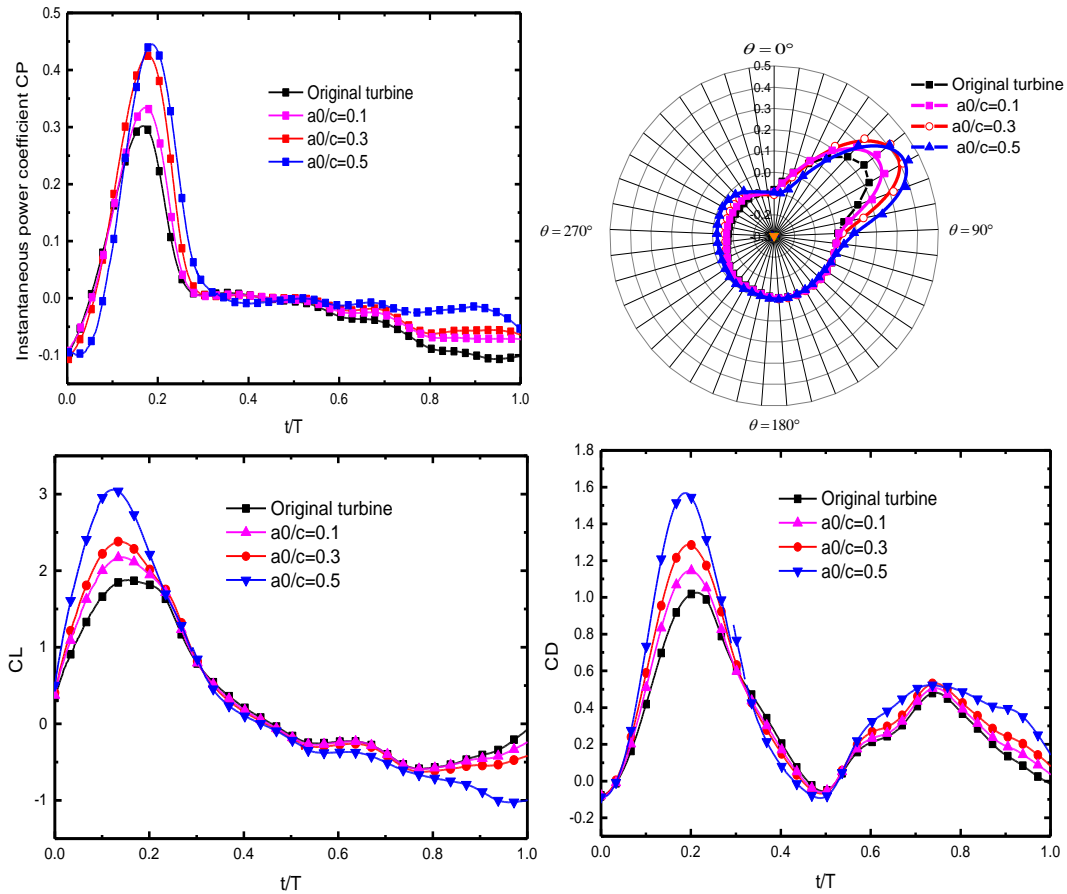


Fig.III.20. (a) Instantaneous blade moment coefficient versus θ (b) Instantaneous power coefficient (c) Instantaneous lift coefficient (d) Instantaneous drag coefficient .

The effect of oscillating amplitude on the time-mean power coefficient and the time average input power coefficient is shown respectively in Fig.III.21 (a) and (b). For a comparison among all cases, It can be seen that the turbine with the largest amplitude of $a_0/c = 0.5$ and $a_0/c = 0.3$ displays the highest power coefficient, in which an increase of 25% as compared to original turbine is possible. The time-mean power coefficient values becomes smaller when the oscillating amplitude decreases from $a_0/c = 0.5$ to $a_0/c = 0.1$. For the case $a_0/c = 0.5$ the input

power factor appears to be greater with 5–10 % than that of the two cases $a_0/c=0.3$ and $a_0/c=0.1$.

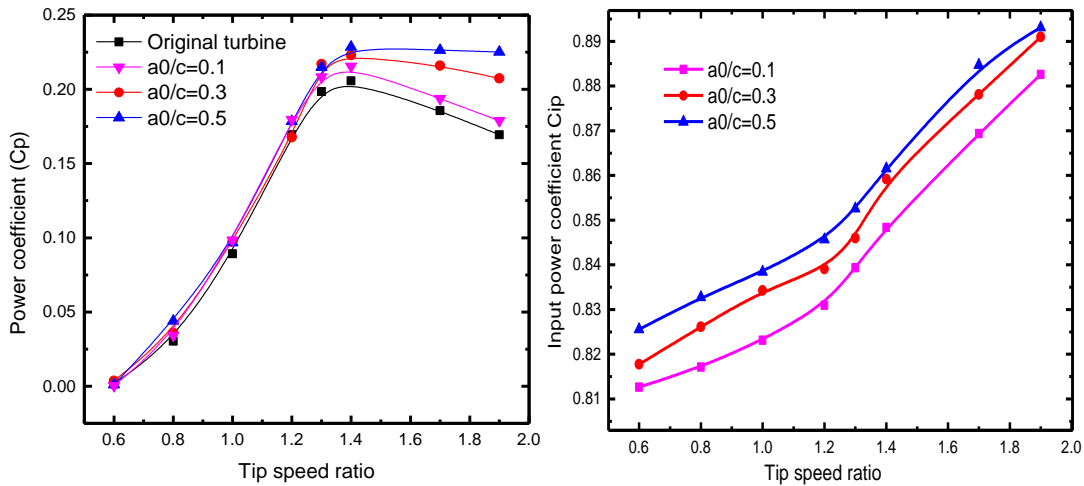


Fig.III.21.(a) Time-averaged power coefficient versus λ .(b) Time-averaged input power coefficient versus λ .

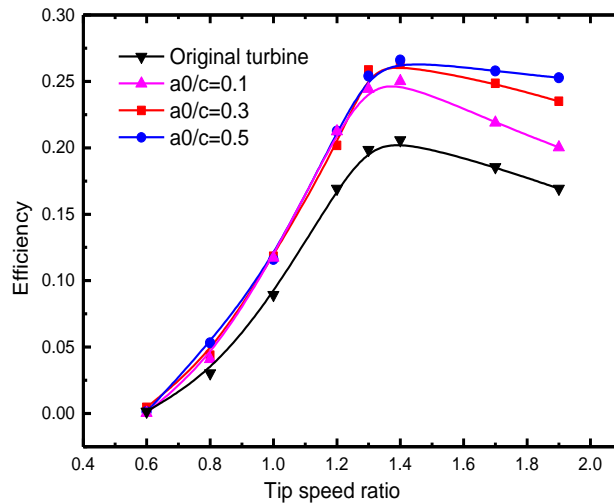


Fig.III.22. Time-averaged efficiency coefficient versus λ .

The variation of turbine efficiency coefficient is depicted in Fig.III.22. Typically this factor is equal to zero for the rigid blade turbine. It can be seen that this factor tends to increase with the rise of tip speed ratio values. Fig.III.22 indicates that the efficiency has the same behavior as that of power coefficient. Fig.III.23 illustrates that the increase in the flexure amplitude lead to a larger vortex size in the blade wake. It should recall that for the best performance, large oscillating amplitude must be chosen in the first quarter of the turbine, with which the LEV is effectively controlled. Thus the enlargement of the LEV affects in advantage the performance of the VAWT.

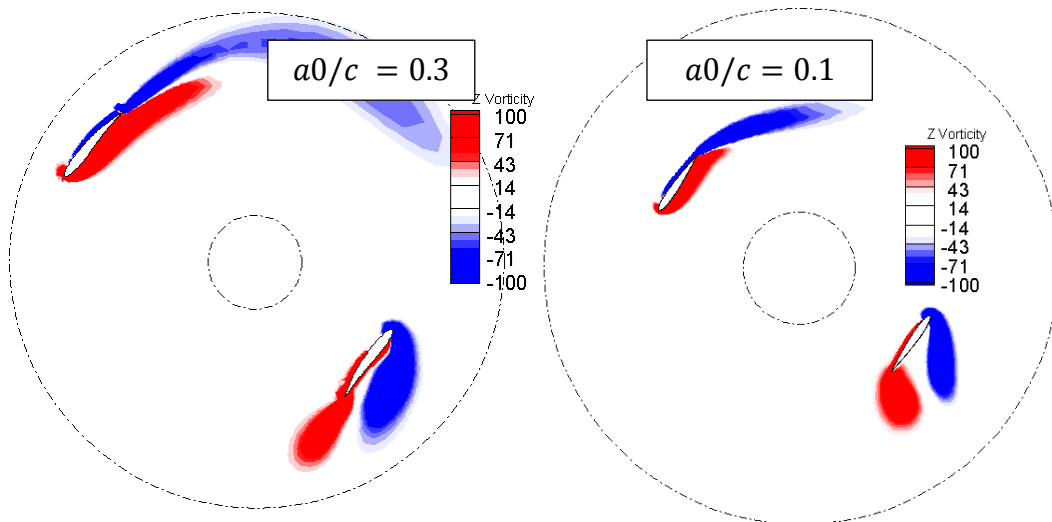


Fig.III.23. Comparison of instantaneous vortex contours at $\lambda = 1.4$ with $z_i = 2$.

In this section, it is shown that the proposed active flow control mechanism that consists in the use of a flexible turbine blade instead of rigid blade can improve energy extraction. Computational results indicate that for a tip speed ratio $\lambda = 1.4$, a frequency controlled parameter $z_i = 4$, and a flexure amplitude $a_0/c = 0.3$, the peak power coefficient (CP) rises about 38% relative to the original turbine.

III.3.5. Airfoil shape effect

The effect of flexible airfoils types and blades flexibility on the net output power is proposed. To this end, five different flexible airfoils (Symmetric and Non-symmetric) are employed (Fig.III.24).

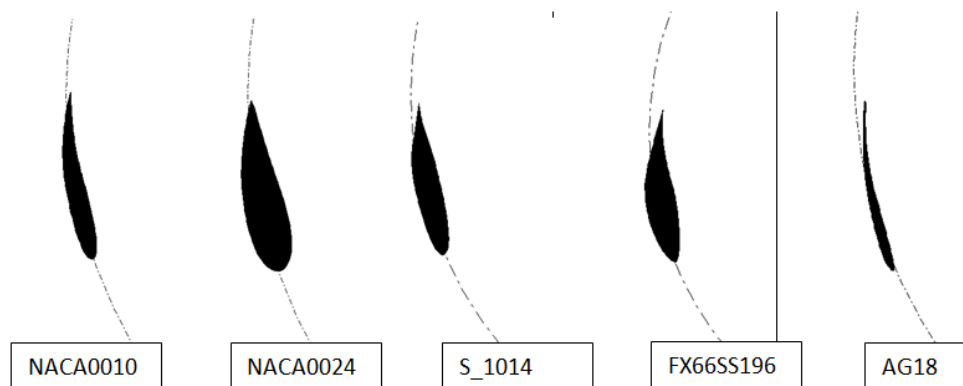


Fig.III.24. Photographs for the flexible airfoils shapes at $\theta = 100^\circ$.

The present section investigates the effect of flexible airfoil shapes on the vertical axis tidal turbine performance. Thus, symmetric (NACA0024, NACA 0010) and non-symmetric

(AG18, S_1014, FX66SS196) airfoil shapes are employed. Results indicate that, for both rigid and flexible blades, the turbine based of the symmetric NACA0024 airfoil can generate the highest torque as compared firstly to the symmetric NACA0010 airfoil; this means that the airfoil thickness has an important impact on the turbine performance with or without the new concept of flexibility. Secondly, compared to non-symmetric airfoils the symmetric airfoils produce wider torque which means that the stall can be delayed by using symmetric airfoils. A flexible thin airfoil (AG18) is absolutely not preferable as compared to rigid blade. The maximum NACA0024 instantaneous C_m coefficient is 0.45 which is about 55% times that of the NACA0024 rigid blade turbine. The NACA0024 rigid blade turbine (without flexion) performs better than the AG18 and FX66SS196 flexible and rigid turbine. An increase in torque coefficient of 30%, 66.66%, 51.11% and 22.22% as compared respectively to NACA 0010, AG18, FX66SS196 and S_1014, is achievable with the flexible NACA0024 airfoil type.

Fig.III.25 shows (a) the instantaneous power coefficient for rigid airfoils and (b) the maximum instantaneous power coefficient for the flexible turbine case corresponds to $z_i=4$ and $a_0/c=0.1$.

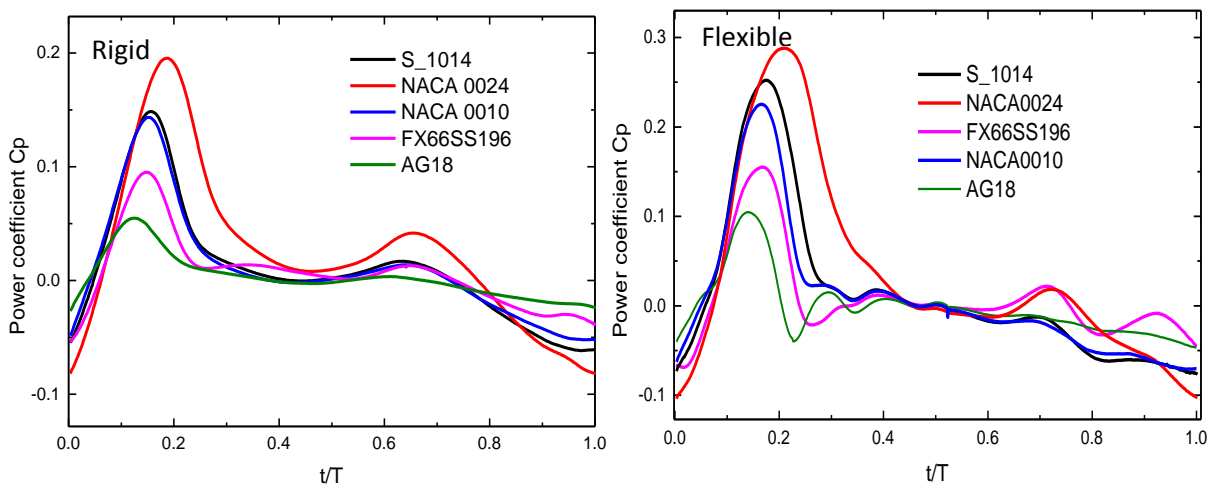


Fig.III.25. Instantaneous power coefficients for different airfoils $z_i=4$, $a_0/c=0.1$. $\lambda = 0.7$

Typically, the NACA0024 turbine which has the maximum instantaneous C_m coefficient will generate the maximum power coefficient. It can be seen that the power coefficient is shifted right by increasing the airfoil thickness, which mean that the turbine can extract energy for a large azimuthal angle and therefore large operating range (tip speed ratio) is expected for such configuration. The gain in power coefficient ΔC_P is depicted in Fig.III.26. It can be found that for the two airfoils S1014 and NACA0024 a similar gain is registered. Also using the

flexible blade is more efficient for the NACA0010 airfoil than the FX66SS196 and AG18 airfoil.

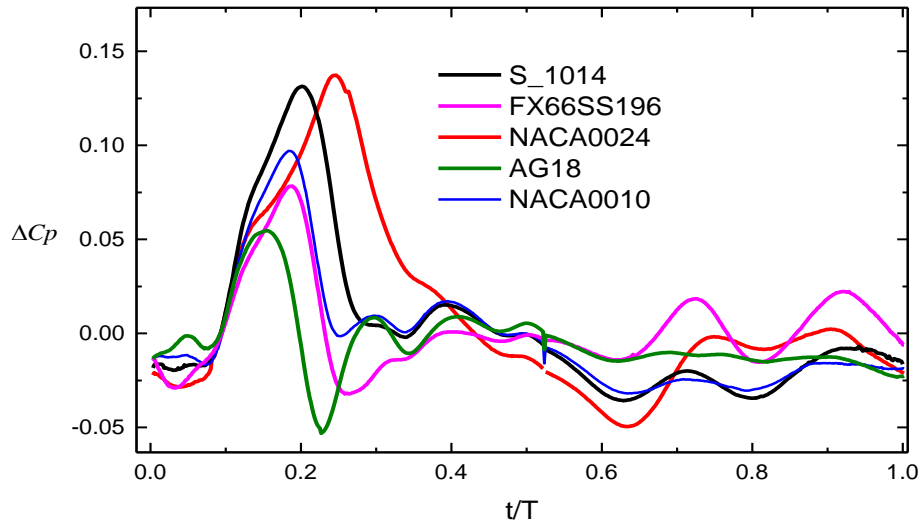


Fig.III.26. Gain in power coefficients for different airfoils.

The airfoil thickness has an important impact on the flow behavior and therefore on the turbine performance with or without the new concept of flexibility. Compared to non-symmetric airfoils the symmetric airfoils produce wider torque which means that the stall can be delayed by using symmetric airfoils this is attributed to the fact that for non-symmetric airfoils the flexure motion increases the profile curving and then when the blade coming to large azimuthal angle, the vortices shed without attached to the blade suction surface (Fig.III.27), which leads to a deep stall interpreted by a drop in the torque coefficient.

In contrast to the pressure contour associated with the other turbine blades, the NACA 0024 (Fig.III.28) shows that the pressure is distributed correctly along the blade and a lessened flow separation range is registered. For the AG18 and FX66SS196 turbines, blades are in deep stall and the high pressure region is delayed to the half of the blades which interpreted by a drop in the output power coefficient.

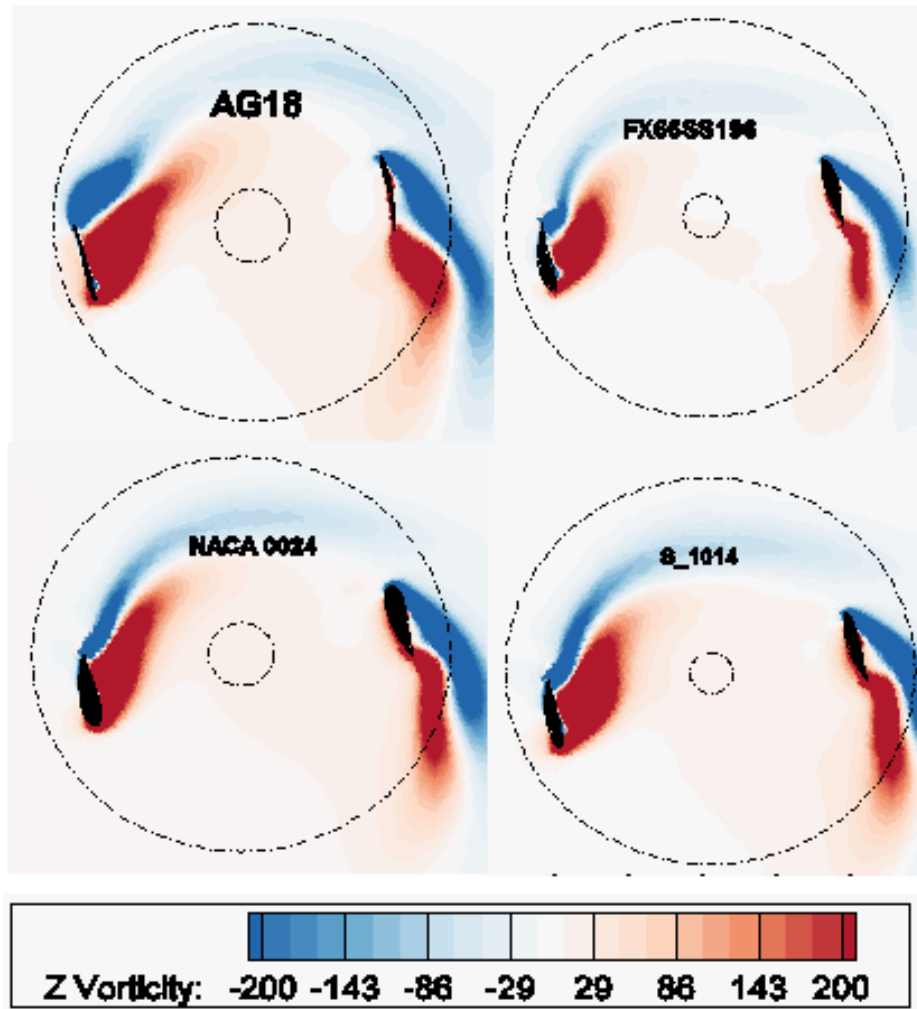


Fig.III.27. Comparison among instantaneous vortex contours.

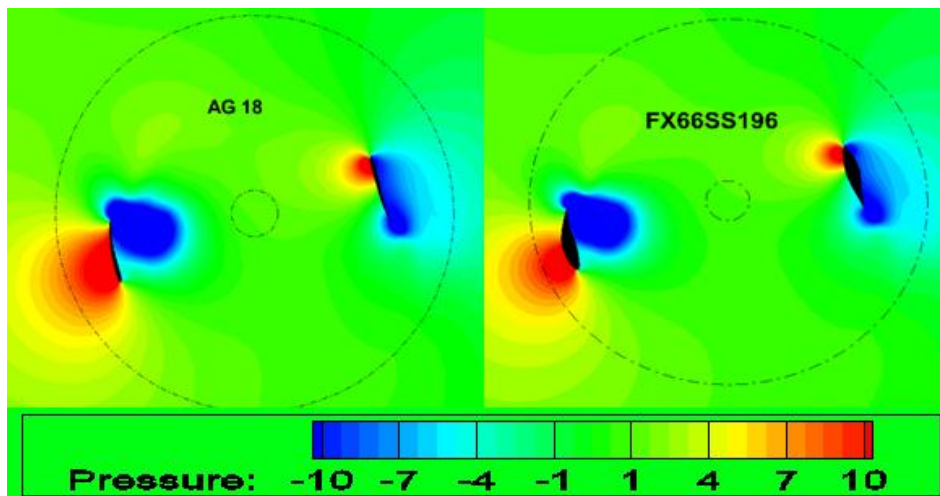


Fig.III.28. (a) Pressure contour for AG18 and FX66SS196 turbines

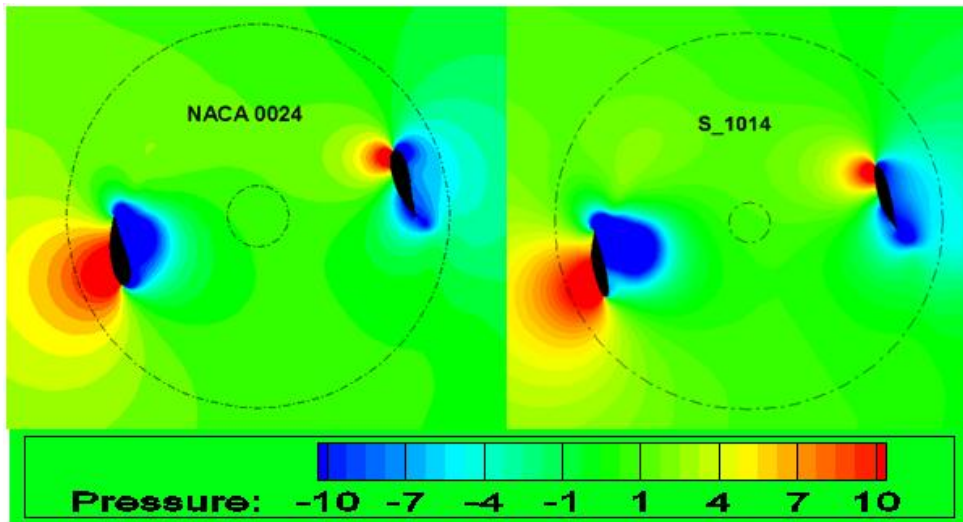


Fig.III.28 (b) Pressure contour for NACA0024 and S_1014 turbines.

III.3.6. Effect of flexible coefficient n

To study the effect of flexible coefficient n , (see equations II.24 to II.28 chapter II) on the output power, the NACA 0024 it selected. Fig.III.29. depict the blade deformation for different n values. As it is shown, the degree of flexibility is controlled by the factor n , where n equals to 1 means a rigid wing. Fig.III.30. (a) and (b) introduce the blade flexibility effect on the instantaneous momentum coefficient and the instantaneous power coefficient. It is clearly seen that all flexible cases offer a higher momentum coefficient than the rigid case. Results reveal also that the degree of flexibility influences weakly the peak power and momentum coefficients. The mean CP coefficient increase about 5% by varying the flexible factor from 1 to 5.

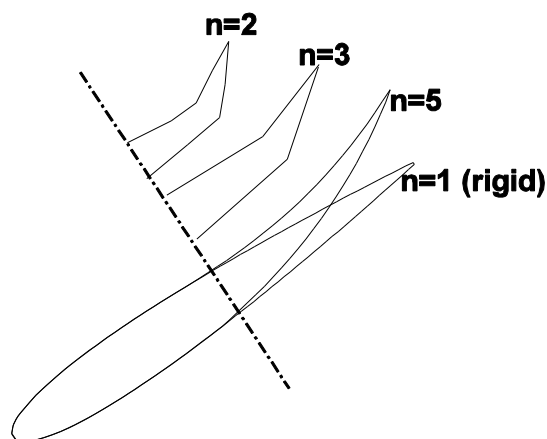


Fig.III.29. Effect of flexible coefficient n on the blade shape

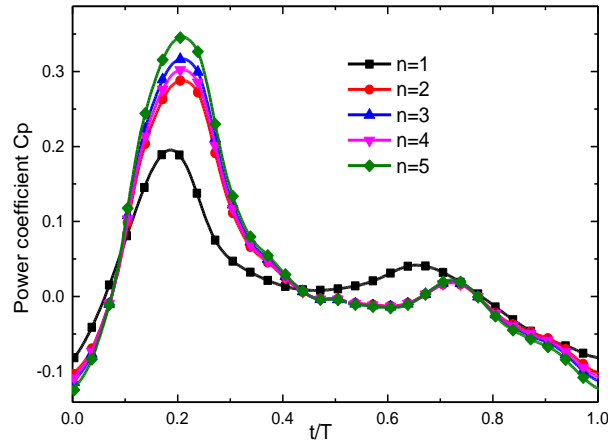


Fig.III.30. Effect of flexible coefficient n on the instantaneous power coefficients (NACA0024).

III.3.7. Effect of flexure length L_c

As it is mentioned in chapter II, the flexion is started from a given distance L_c (see Fig.III.31). In this section, the flexible coefficient L_c effect is investigated. Fig.III.32 indicates that the maximum CP of 0.3 and Cm of 0.41 is achieved for $L_c = 0.1$. Increasing the flexible coefficient L_c from 0.1 to 0.3, the peaks Cm drop respectively to 0.23 and 0.33. This behavior is attributed to the mechanism of LEV forming. The appropriate selection of this factor leads to an effective control of the LEV size and strength.

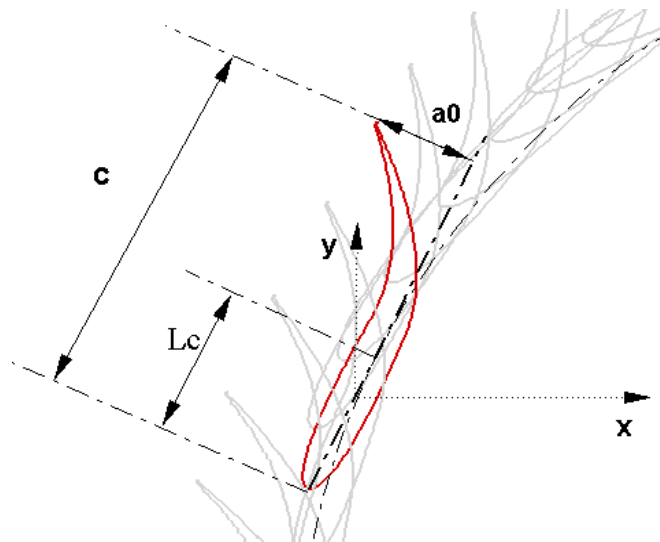


Fig.III.31. Schematic diagram of the deforming turbine blade

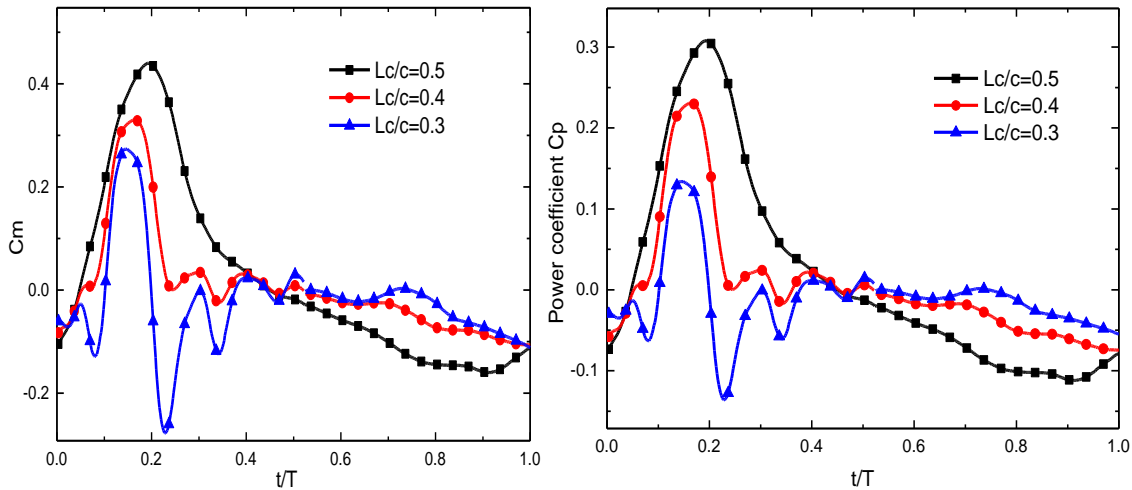


Fig.III.32. Effect of flexible coefficient Lc on (a) Instantaneous moment coefficients and (b) Instantaneous power coefficients (NACA0024)

In practice, a distinction between air and water Darrieus turbines is necessary. For water applications, because of the fluid density, Darrieus water or tidal turbines are always associated with dynamic stall phenomena. For air, the Darrieus turbine is less affected.

Ashraf [64] studied the effects of a static camber deformation over the flapping cycle on the flapping foil propulsive efficiency. The results indicated that the propulsive efficiency increased effectively for the first half of the flapping cycle and decreased by about the same amount for the second half, which reveals that a time varying camber deformation will increase dramatically the efficiency. Hoke et al [65] outlined that the concept of time varying camber deformation can effectively improve the efficiency of a flapping airfoil power extraction system. In this section, the effect of camber deformation on the VATT performance is proposed.

III.4. Flow control by flexible deformable blade with a time varying camber deformation (Tidal turbine)

In order to investigate the effect of this type of deformation, a time varying camber deformation is applied by deforming the airfoil camber line via a sinusoidal circular arc. Evaluating from fluid analysis perspectives, a time varying camber deformation can effectively boost the size and the strength of the leading edge vortex (LEV). The camber deformation can be considered as a deflection of the trailing edge plus a deflection of the leading edge which controls firstly the flow angle of attacks and therefore the LEV time of growth (leading edge control) and secondly, the size and strength of the LEV (trailing edge

control). When the LEV grows up a suction zone is simultaneously generated, which increase the pressure difference between the upper and the lower surfaces of the foil. Thus, the peaks of lift force can effectively increase.

III.4.1. Mechanism of the VATT performance improvement

To delve into the mechanism by which the camber deformation affects the power extraction performance, the pressure distribution and torque are necessary to be examined in detail. To this end, the flexible case with $z_i = 4$ and $a_0/c=0.1$ is examined. As a reference, the corresponding rigid blade case is also considered.

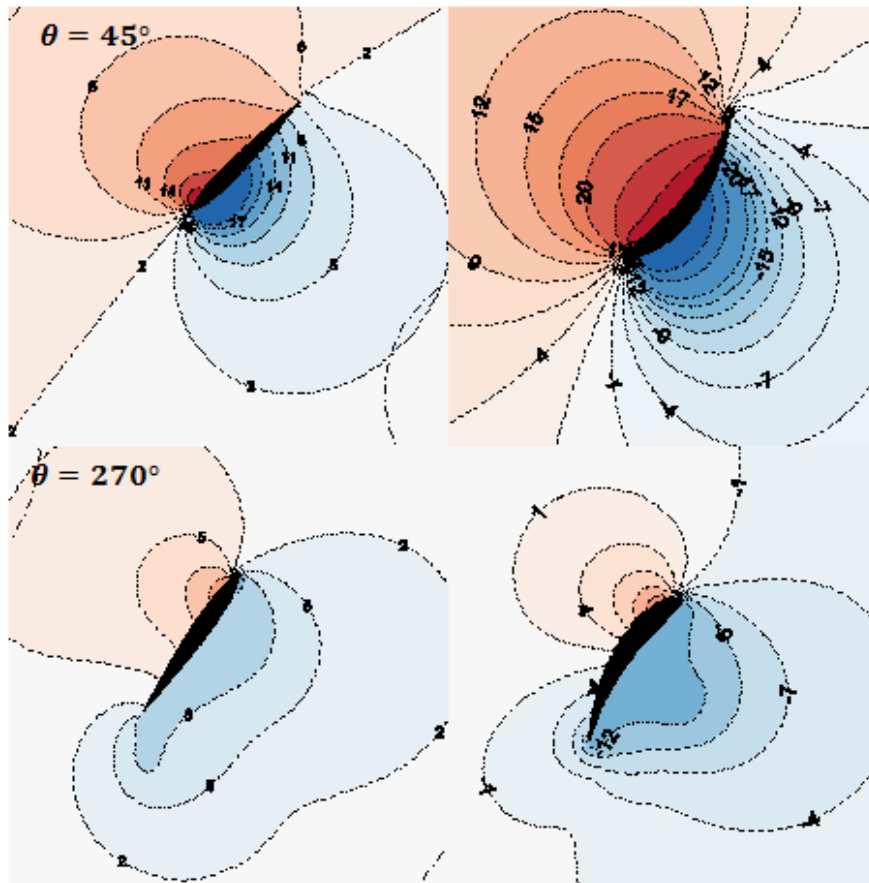


Fig.III.33. Comparison between blade surface pressure distributions

Fig.III.33 provides the instantaneous pressure coefficients. At azimuthal angle $\theta = 45^\circ$ the foil is at the middle position of the first quarter, which results in the maximum depression along the downward direction. At this moment, the leading edge vortex (LEV) that is frequently observed is fully developed; consequently, the instantaneous torque coefficient approximately achieves the maximum value (Fig.III.34). Due to the camber deformation, trailing edge vortices (TEV's) occur around the tip end (Fig.III.35) of the blade which can

simultaneously increase the pressure above the upper surface of the blade and decrease the pressure below the lower surface. As a result, the instantaneous torque can be boosted. When the blade undergoes the upward stroke $\theta = 270^\circ$, the flow pattern is similar to that discussed in the trailing edge flow control section.

The camber deformation can be considered as a deflection in the trailing edge plus a deflection in the leading edge which controls firstly the flow angle of attacks and therefore the LEV time of growth and secondly, controls the size and strength of the LEV.

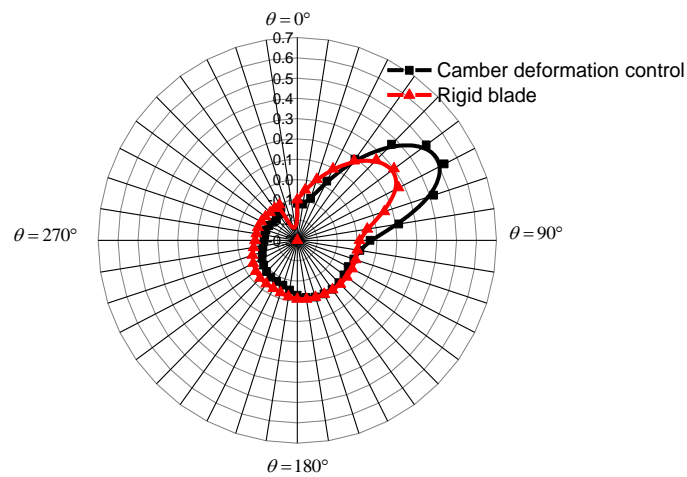


Fig.III.34. Comparison of instantaneous moment coefficients for different blade turbines

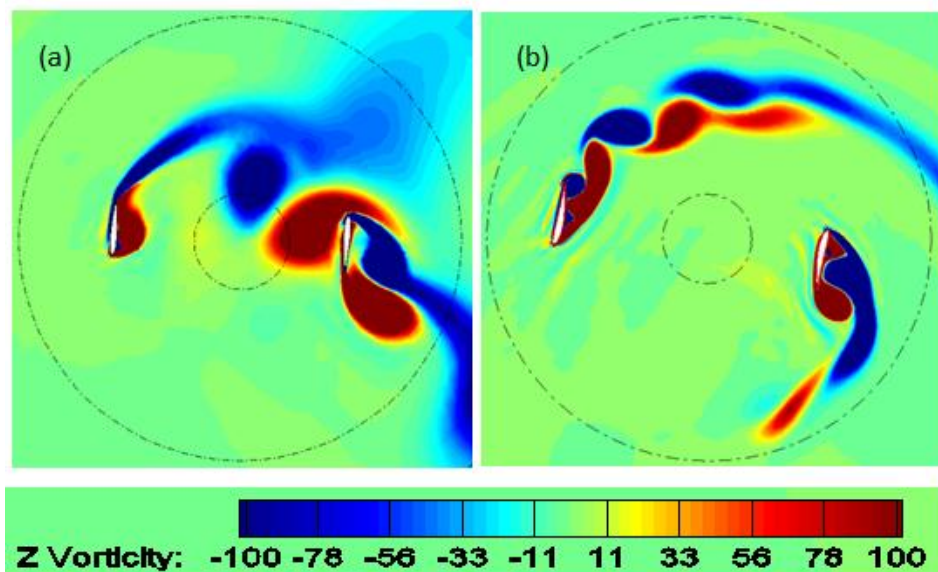


Fig.III.35. Downstream wakes contours for both cases (a) Original and (b) Flexible configuration

III.4.2. Output power

It will be very judicious to check the effects of varying the flapping frequency and the flexure amplitude on the energy extraction efficiency. The frequency is controlled between $zi = 4$ and 12, while the extent of the plunging amplitudes is controlled between $a_0/c = 0.03$ and 0.2. While, the considered tip speed ratio is between 2 and 4.7.

- **Oscillating amplitude effect**

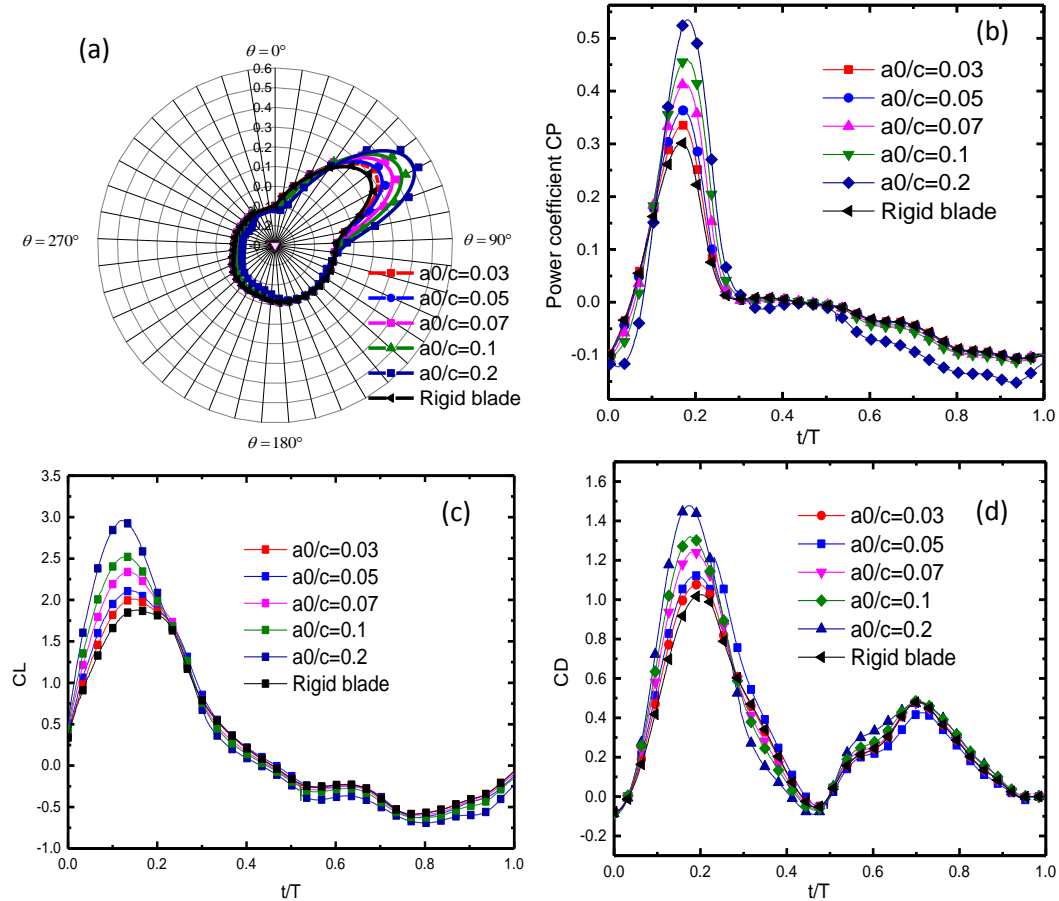


Fig.III.36. (a) Instantaneous blade moment coefficient versus θ .(b) Instantaneous power coefficient .(c) Instantaneous lift coefficient .(d) Instantaneous drag coefficient

For a controlled frequency $zi=4$, the effect of oscillating amplitude is considered. It can be seen that a similar trends of the rigid blade is recorded for the quantities C_m , CP , CL and CD (Fig.III.36). By Taking a look to the instantaneous power coefficient in Fig.III.36 (b), an increase of 42% for the CP compared to the original turbine, is possible with an oscillating amplitudes of $a_0/c = 0.2$ This behavior is attributed to the enlargement of the LEV.

By increasing the flexure amplitude from $a_0/c=0.03$ to $a_0/c=0.2$ CL and CD increase respectively from 2 to 3 and from 1.1 to 1.5. To achieve a best performance, large oscillating amplitude must be chosen with which the LEV is effectively controlled.

The effect of oscillating amplitude on the mean power's coefficient and the average input power coefficient is shown respectively in Fig.III.37 (a) and (b). For the considered cases, It can be seen that the turbines with the largest amplitude of $a_0/c = 0.2$ display the higher power's coefficient, the increase is about 42% compared to the original turbine. The power coefficient values increases with the increasing in the oscillating amplitude from $a_0/c = 0.03$ to $a_0/c = 0.2$. For the case $a_0/c = 0.2$ the input power factor is greater than that of the case $a_0/c = 0.03$ about 23.52% for a tip speed ratio equal to 2 and about 6.36% for a tip speed ratio equal to 4.7.

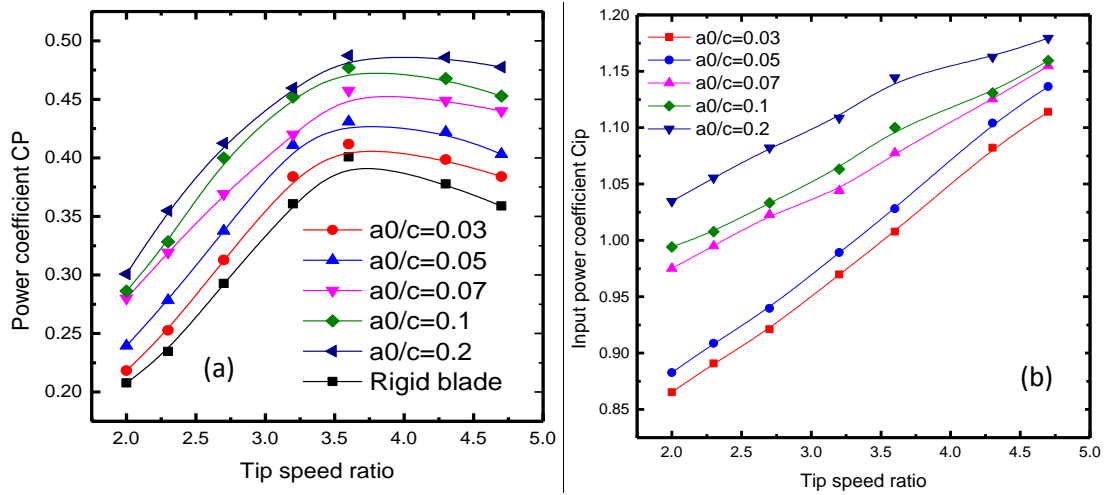


Fig.III.37. a) Time-averaged power coefficient versus λ .(b) Time-averaged input power coefficient versus λ

The variation of the turbine efficiency coefficient is depicted in Fig.III.38. Typically this factor is equal to zero for the rigid blade turbine. It can be seen that this factor tends to increase with the rise of tip speed ratio values. Also Fig.III.38 indicates that the efficiency curves have the same tendency of the power coefficient curves.

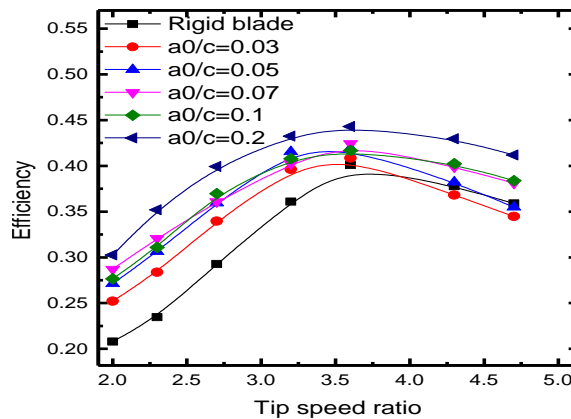


Fig.III.38. Time-averaged efficiency coefficient versus λ

• **Oscillating frequency effect**

The effects of oscillating frequency on the instantaneous torque coefficient C_m , the instantaneous power coefficient C_P , the lift coefficient C_L and the drag coefficient C_D are illustrate in Fig.III.39 (a) to (d).

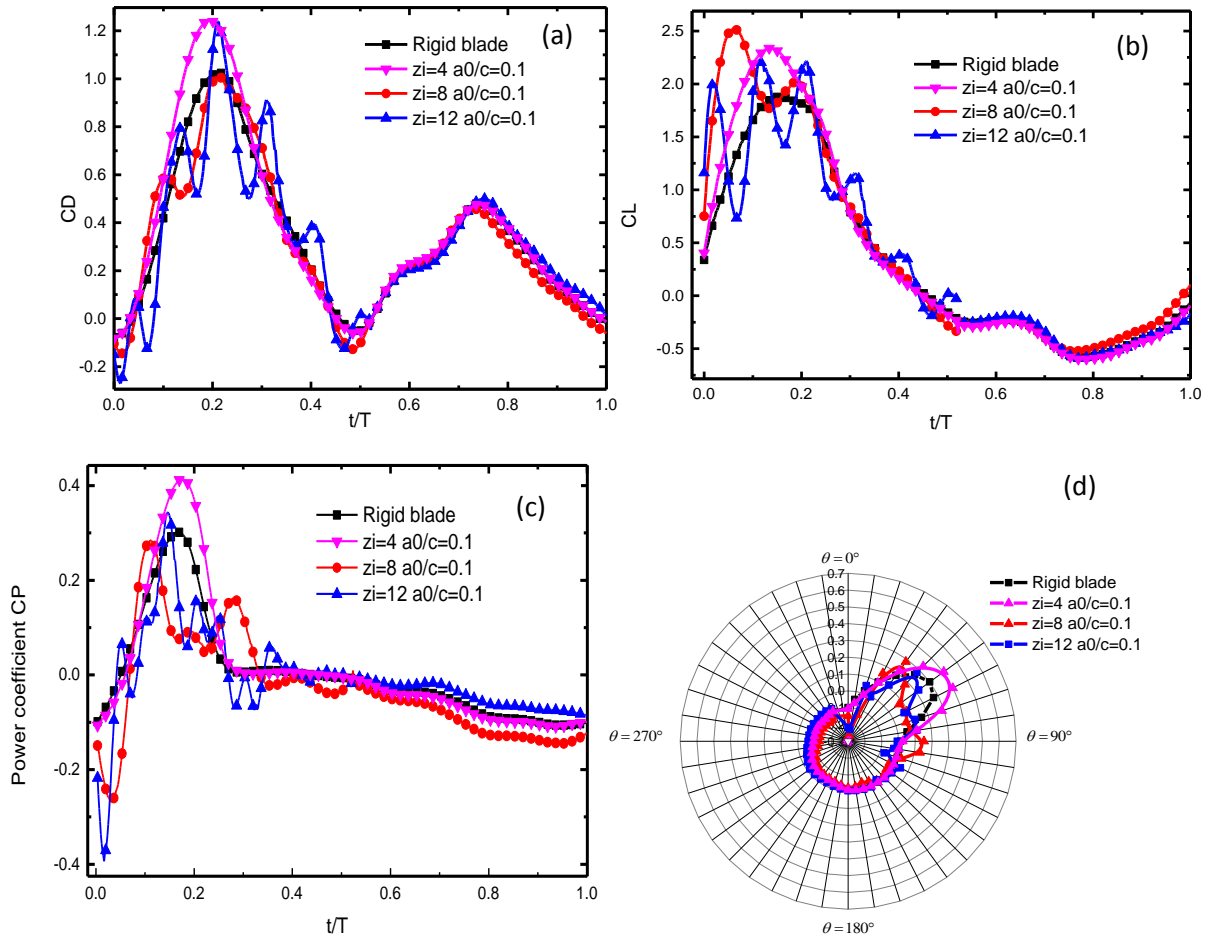


Fig.III.39. (a) Instantaneous drag coefficient.(b) Instantaneous lift.(c) Instantaneous power coefficient coefficient. (d) Instantaneous blade moment coefficient versus θ

It can be seen that, for all tested cases the peak of the moment coefficient is registered for an azimuthal angle θ between 0° and 90° , which means that the greater part of the harvested energy is done between the azimuthal coordinates 0° and 90° . Moreover, excluding the case $z_i=4$, all controlled cases generate a lower moment peaks than the rigid blade turbine. For the two case $z_i = 8$ and $z_i = 12$, the C_L, C_D and C_P curves display multiple peaks with a smaller amplitudes due to the vortex shedding that is caused by the blades deformation. For the case $z_i=4$, all curves have the same trends of the rigid blade. However, a higher peak is registered for the flexible turbines.

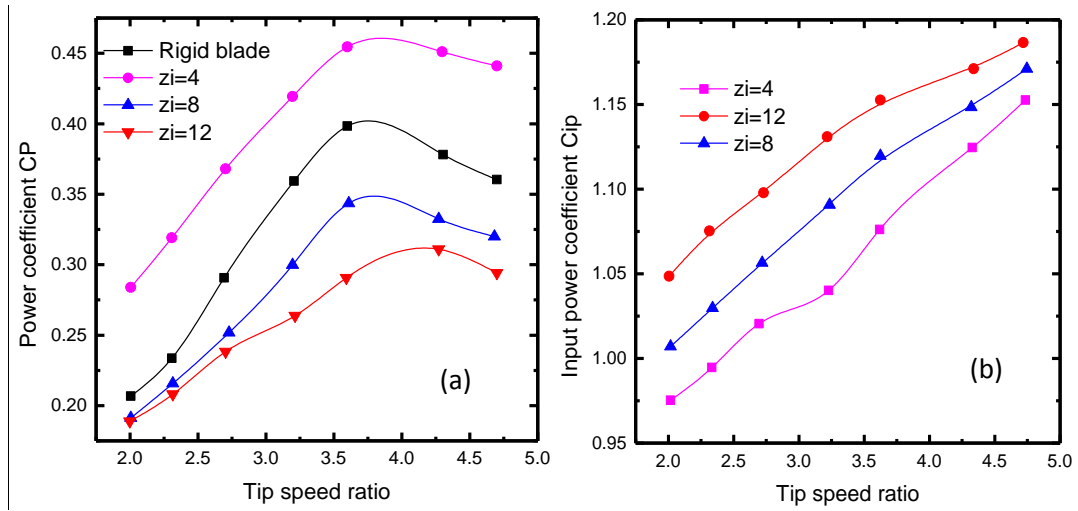


Fig.III.40 (a) Time-averaged power coefficient versus λ .(b) Time-averaged input power coefficient versus λ

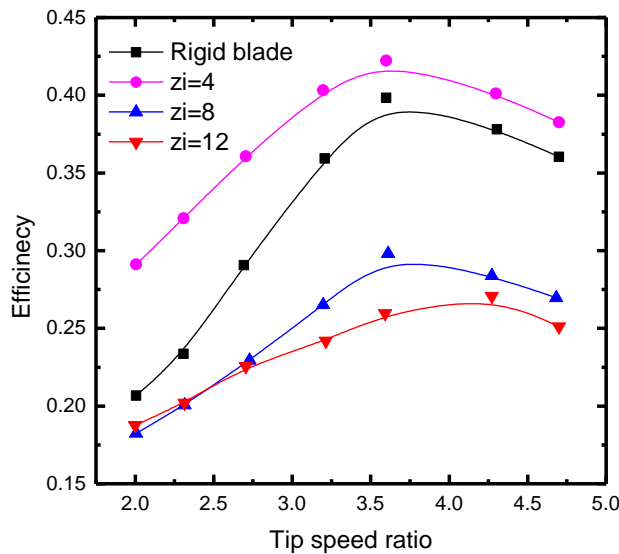


Fig.III.41.Time-averaged efficiency coefficient versus λ

The peak CP increases from 0.3 to 0.41, the CL and CD peaks increase respectively from 1.8 to 2.4 and from 1 to 1.24. This fact is attributed to the control of LEV strength compared to rigid blade. The effect of varying the flapping frequency on the mean power coefficient is shown in Fig.III.40 (a). Taking a closer look to the power coefficient curves, it can be draw the common features: for low speed's tip ratio $\lambda < 3.5$, the power coefficient CP follows a quasi-linear evolution until a critical point which corresponds to the $C_{p_{max}}$, after what it decreases with the further increase in the tip speed ratio. For all λ , the foil oscillating with $zi=4$ produces the much higher CP. The maximum power coefficient is 0.46 which is about 12.5% better than the original turbine. Therefore, the proposed control strategy in this work allows reaching a wider range of high power coefficient. By against, for the frequency $zi=8$

and $z_i = 12$, the efficiency of the turbine decreases, compared to the VATT with rigid blade. A drop of about 46 % in the output power coefficient is registered. This behavior is due to the change in the flexion direction that has been discussed previously. This indicates that this control case is not useful compared to the conventional rigid turbine. Typically, the efficiency improvement caused by an increase in input power; Fig.III.40 (b) represents the variation of the average input power coefficient in term of the tip speed ratio for different cases. It can be noted that the input power coefficient tends to increase with the tip speed ratio values for all cases. Fig.III.41 shows that the efficiency curves have the same behavior of the power coefficient curves.

III.5. Flow control by using two backward flapping wings

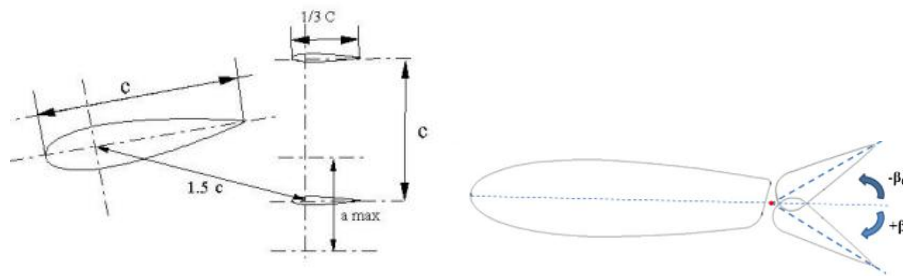


Fig.III.42. (a) Two flapping wings associated to the main blade of the turbine. (b) Slotted blade with oscillating flap [29].

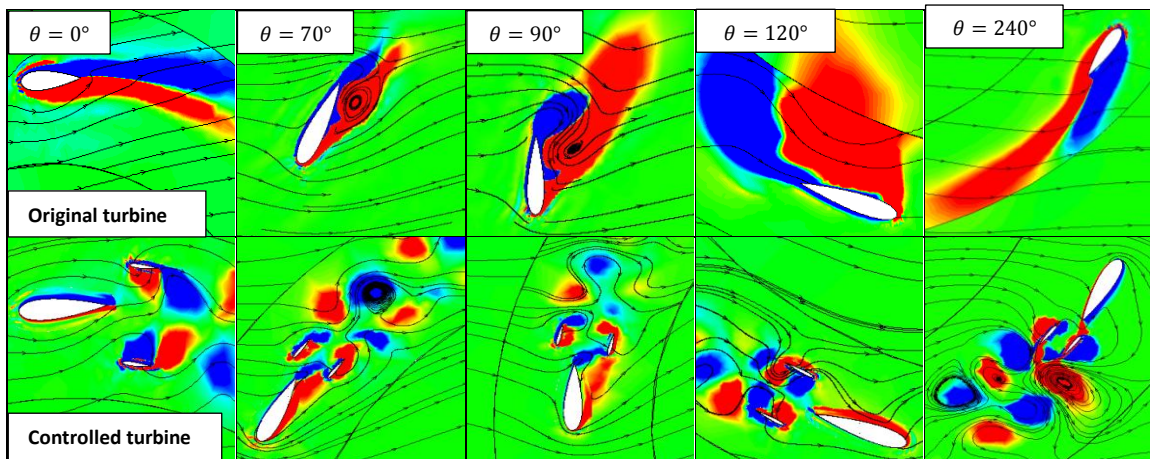


Fig.III.43. Instantaneous Z-Vorticity contours and the generated wakes for different azimuthal positions ($\lambda=2.2$, $z_i=40$)

Inspired from the classical strategy of flow control by using slotted blade with oscillating flap[29], the present section proposes a dynamic control device which consists in the association to each turbine blade, a couple of flapping wings, in biplane configuration. It can be seen that the proposed model allows; first, an excellent reattachment of the boundary layer

and great attenuation of the vortices magnitude around the blades, and secondly, a remarkable reduction of the generated wakes, then avoiding the interaction of the disturbed flow by different turbine blades (Fig.III.43).

III.5.1. The effect of the proposed device on the turbine performance

Fig.III.43 illustrates the vorticity contours of the flow relative to several azimuthal positions for both cases; the original configuration and the controlled configuration. The main results are: At the angle $\theta=0^\circ$; the contours of the vorticity show an attached flow in the main rotor blade for both cases, the stabilizer factor here is the viscosity. A net reduction of vorticity magnitude on the controlled blade is obtained, while counter-rotating vortices arise downstream of flapping-wings. For the angles adjacent 70° , a highly visible vortex appears along the original blade, resulting in a detached flow from the trailing edge and grows while going towards the leading edge. By contrast for the controlled turbine, the two flapping wings generate a phenomenon of reverse Karman Street. For the angles adjacent 120° the situation is highly critical because the vortex is detached closely to the leading edge, and simultaneously, and at the trailing edge in counterclockwise, another swirl grows. The flapping wings prevent the development of large vortices by giving rise to small size vortices in their wake. For the angles range 90° 350° , the flapping motion of the backward wings insures efficiently the reattachment of the separated boundary layer of the main blade, relative to the original turbine. This attachment is the result; firstly to the readjustment of the pressure field, and secondly to suction and acceleration of the fluid flow by the flapping motion. In conclusion, it can be noticed:

For the original configuration:

In general, and for most azimuthal positions, thick areas of recirculation flow are installed along the blade. Furthermore, energetic vortices are quickly detached from the blades. This phenomenon generates extended wakes occupying an important space. Mainly, the stall occurs closely to the leading edge and the generated wakes by previous blade interferes with the next one, which compromise the turbine efficiency. Strong dynamic stalls are encountered mostly in the azimuthal angle range between 90° and 180° .

For the controlled turbine:

A substantial attenuation of the flow recirculation is obtained. The controlling device results in the breakdown and the fragmentation of the large energetic vortices, it produces instead

smaller vortices. Moreover, the controlling device reduces substantially the extended of the vortex tails in the downstream wake, then avoiding, the interference with the disturbed flow caused by the previous blades.

III.6. Comparison among flow control techniques

For the comparison among flow control techniques, it is seen that the turbine blade with flexible deformation reaches a maximum power coefficient among three turbines (Fig.III.45). This is attributed to the change in the pressure distribution along the blade. For the flexible blade strategy of control and for a tip speed ration of $\lambda = 0.6$, the peak CP increases from 0.05 to 0.15, the CL and CD peaks increase respectively from 1 to 1.6 and from 0.5 to 1. This fact is attributed to the control of LEV strength compared to rigid blade. For the configuration of backward flapping wing the same trends as the original turbine are registered.

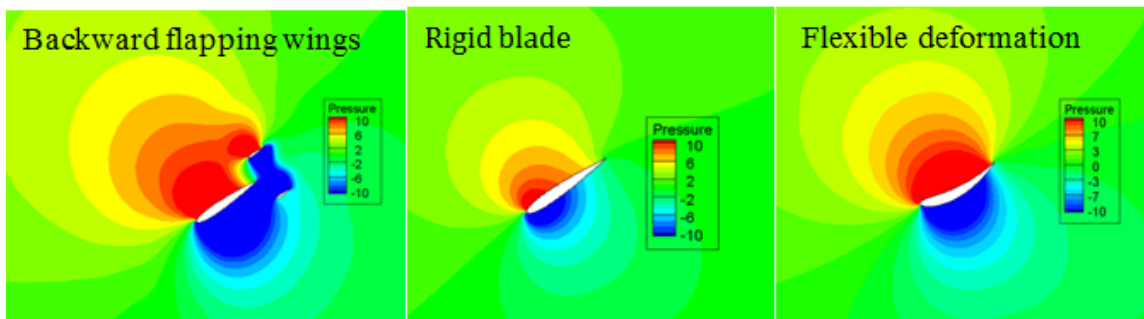


Fig.III.44. Comparison between blades pressure distributions

Examinations of the pressure contour (Fig.III.44) associated with the configuration of backward flapping wings indicate that the depression in the blade upper surface and the overpressure in the lower surface increase with the same amount which obstructs the improvement of the turbine performance, recall that the lift force is due to the difference between the blade upper and lower surface.

In general, it can be concluded that:

- The turbine performance improvement is related directly to the boundary layer flow control
- The downstream wake control cannot enhance the turbine energy extraction efficiency

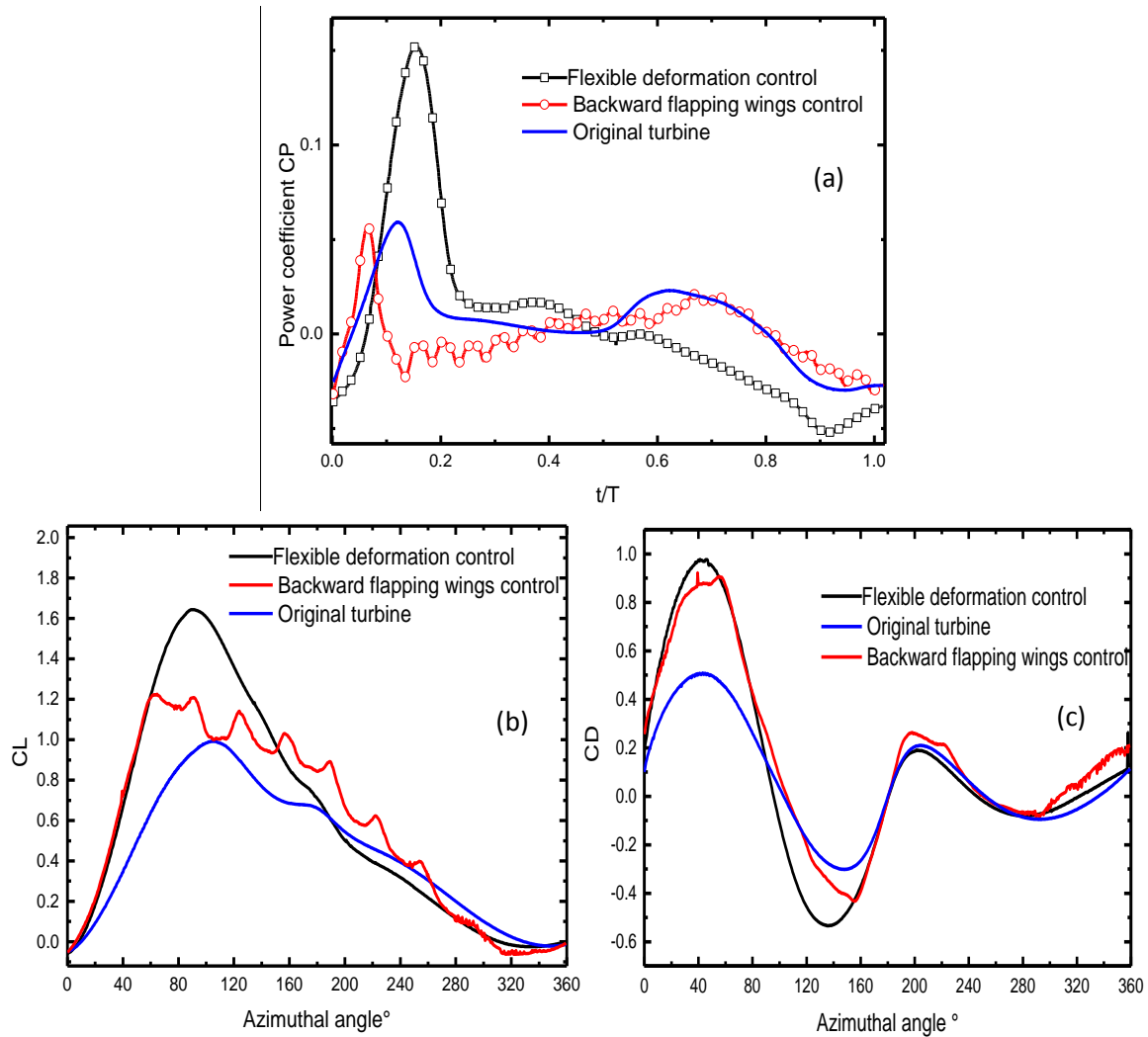


Fig.III.45.(a) Instantaneous power coefficient (b) Instantaneous lift coefficient (c) Instantaneous drag coefficient.

III.7. Conclusion

The extraction of useful and usable power from the renewable energy sources requires the design and the use of specific and appropriate devices, which represents a real challenge that is not always easy to overcome. This study falls within this issue. It deals with the efficiency improvement of vertical axis wind/tidal turbines. A Turbine competitiveness will depend on its level of performance, therefore, will depend directly and in large part, on the air flow behavior passing through it. It is therefore imperative to master and control the boundary layer attachment and the extended of the generated vortices and wakes. The proposed idea is the use of different active control techniques, the first one proposed an active flow control mechanism that consists in the use of a flexible turbine blade instead of rigid blade.

Computational results indicate that for a tip speed ratio $\lambda = 1.4$, a frequency controlled parameter $zi = 4$, and a flexure amplitude $a_0/c = 0.3$, the peak power coefficient (CP) rises about 38% relative to the original turbine. The second one utilizes a flexible deformable blade that change shape during the turbine rotation. A time varying camber deformation is applied by deforming the airfoil camber line via a sinusoidal circular arc. Numerical results show that this strategy of control indeed enhance the VATT performance. For a tip speed ratio $\lambda=3.5$, a frequency $zi=4$, and a flexure amplitude $a_0/c=0.2$; the power coefficient (CP) rises about 40% relative to the original turbine. The third one consists of the association to each turbine blade, a couple of flapping wings, in biplane configuration. The proposed model ensures an excellent boundary layer reattachment and an important attenuation in the magnitude of the generated vortices, and a rapid mitigation of the generated wakes, then avoiding, the interference with the disturbed flow caused by previous blades.

GENERAL CONCLUSIONS

Wind and tides have been considered as promising renewable sources for energy extraction and electricity generation. The two sources share many similarities concerning energy harvesting. In recent decades, the wind industry focused totally in the Horizontal Axis Wind Turbine (HAWT) as the best tools for electricity generation, based on efficiency and scalability, consequently, this technology has been deeply developed. The use of vertical axis wind or tidal turbines remained less investigated due to this fact.

Newly, the interest is converted to vertical axis turbines technology due to its potential advantages as an aerodynamic or hydrodynamic device. The VAWT can be an efficient alternative to HAWT due to its simple installation, cost and its insensibility to flow direction.

In this thesis, new flow control strategies are proposed to improve the turbine efficiency, the first is a VAWT having flexible deforming blades, the second is a control by using backward flapping wings. The numerical model has been validated against experimental results. A better understanding of the complex flow behavior across the VAWT has been achieved. The ultimate objective was the proposition of a robust and efficient model of VAWT. This goal is achieved by computational tool that can provide a detailed description of the flow behavior and the entire related data, at relatively short time and low cost. If an experiment is performed, the computation will reduce its cost by building only the optimum or near-optimum prototype. The combination between the simulations and the experiments will powerfully speed up the VAWT development and bring it back to the top of the wind industry agenda. The Reynolds Average Navier Stokes (RANS) equations with a $k - \varepsilon$ turbulence model were applied using the commercial computational fluid dynamics software ANSYS FLUENT v15.0. With the objective of describing the extremely unsteady flow over the VAWT, an appropriate mesh around the geometry of the turbine blades and a transient solver were employed.

The turbine rotation is performed through both the sliding mesh strategy and a layering technique. In order to govern the mesh generation in different zones, the equations governing the synchronized flapping motion are integrated in a User Defined Function (UDF) instructed as a C++ code.

The use of a flexible turbine blade instead of rigid blade indicates that for a tip speed ratio $\lambda = 1.4$, a frequency controlled parameter $z_i = 4$, and a flexure amplitude $a_0/c = 0.3$, the peak power coefficient (CP) rises about 38% relative to the original turbine.

This study examines also the effect of flexible airfoils types and blades flexibility on the net output power. To this end, five different flexible airfoils (Symmetric and Non-symmetric) are employed. Results show that, the use of a thick flexible symmetric airfoil can effectively increase the output power. An increase in torque coefficient of 30%, 66.66%, 51.11% and 22.22% as compared respectively to NACA 0010, AG18, FX66SS196 and S_1014, is achievable with the flexible NACA0024 airfoil type. It is also apparent that blades having high flexibility are not recommended as compared to less flexible or rigid blades.

The use of camber deformation indicates that for a tip speed ratio $\lambda=3.5$, a frequency controlled parameter $zi=4$, and a flexure amplitude $a0/c=0.2$; the power coefficient (CP) rises about 40% relative to the original turbine. Performing a control by using backward flapping wings indicates that the turbine performance improvement is related directly to the boundary layer flow control, not to the downstream wake control.

It is our hope that the proposed models and their future developments can be used in commercial scale to support the implementation of VAWT technology as viable, environmentally- kindly tool for electricity generation.

BIBLIOGRAPHY

- [1] European Commission Climate Action, 2010. URL http://ec.europa.eu/clima/policies/package/index_en.htm.
- [2] REN21. "Renewables Global Status Report." 2014. www.ren21.net (accessed October 20, 2014).
- [3] GWEC. Global Wind Energy Council. 2012. www.gwec.net (accessed October 20, 2014).
- [4] Darrieus GJM. Turbine having its rotating shaft traverse to the flow of the current, US Patent No. 1,835,018; 1931.
- [5] Tjiu W, Marnoto T, Mat S, Ruslan MH, Sopian K: Darrieus vertical axis wind turbine for power generation I: assessment of Darrieus VAWT configurations. *Renew Energy* 75 (2015)50-67.
- [6] Muhammad M, Aslam B, Nasir H, Ahmed U F, Zain A, Sh. Rehan J, Zahid. H: Vertical axis wind turbine –A review of various configurations and design techniques *Renewable and Sustainable Energy Reviews* 16 (2012) 1926– 1939.
- [7] SRC–Vertical. <http://www.eng.src-vertical.com/information/infobasic>[accessed 04.03.11]
- [8] Eriksson S, Bernhoff H, Leijon M : Evaluation of different turbine concepts for wind power. *Renewable and Sustainable Energy Reviews* 12 (2008) 1419–34.
- [9] Howell R, Qin N, Edwards J, Durrani N : Wind tunnel and numerical study of a small vertical axis wind turbine. *Renewable Energy* 35(2010) 412–22.
- [10] Gorelov DN, Krivospitsky VP. Prospects for development of wind turbines with orthogonal rotor. *Thermophysics and Aeromechanics* 15(2008) 153–7
- [11] Energy Efficient Choices. <http://www.energyefficientchoices.com/wind-turbine-power-energy/vertical-axis-wind-turbines.php> [accessed 04.03.11].
- [12] Ponta FL, Seminara JJ, Otero AD : On the aerodynamics of variable-geometry oval-trajectory Darrieus wind turbines. *Renewable Energy* 32 (2007) 35–56.
- [13] Price TJ. UK large-scale wind power programme from 1970 to 1990: the carmarthen Bay experiments and the Musgrove vertical-axis turbines. *Wind Eng* 30(2006)225-42
- [14] Sharpe T, Proven G. Crossflex: Concept and early development of a true building integrated wind turbine. *Energy and Buildings* 42(2010) 2365–75
- [15] Zhang Q, Chen H, Wang B : Modelling and simulation of two leaf semi-rotaryVAWT. *Zhongyuan Institute of Technology* 2010. p. 389–398.
- [16] Mohamed MH, Janiga G, Pap E, Thévenin D : Optimal blade shape of a modified Savonius turbine using an obstacle shielding the returning blade. *Energy Conversion and Management* 52(2011) 236–42
- [17] Sukanta R, Antoine D : Unsteady analysis on the instantaneous forces and moment arms acting on a novel Savonius-style wind turbine *Energy Conversion and Management* 121 (2016) 281–296
- [18] Gavalda J, Massons J, Diaz F. *Solar Wind Technology* 7(1990)457.
- [19] Gupta R, Biswas A. Computational fluid dynamics analysis of a twisted three- bladed H-Darrieus rotor. *Renewable and Sustainable Energy* 2(2010)1–15.

- [20] Debnath BK, Biswas A, Gupta R. Computational fluid dynamics analysis of a combined three-bucket Savonius and three-bladed Darrieus rotor at various overlap. *Journal of Renewable and Sustainable Energy* 1(2009)1–13.
- [21] Wakui T, Tanzawa Y, Hashizume T, Outa E, Usui A. Optimum method of operating the wind turbine-generator systems matching the wind condition and wind turbine type. *World Renewable Energy Congress* 23(2000) 48–51.
- [22] Muller G, Mark F, Jentsch MF, Stoddart E. Vertical axis resistance type wind turbines for use in buildings. *Renewable Energy* 34(2009)1407–12.
- [23] Vertical Axis Wind Turbine, Johnson System, Inc., 2013. Available from: <http://www.johnsonsysteminc.com/green-energy/verticle-axis-wind-turbine/> [accessed 01.03.13].
- [24] Mackenzie J. Clines corners wind energy demonstration project. VAWT Power Management, Inc. 2005. Available from: http://www.vawtpower.blogspot.com/2005_05_01_archive.html [accessed 24.02.13].
- [25] Chi-Jeng Bai, Wei-Cheng Wang Review of computational and experimental approaches to analysis of aerodynamic performance in horizontal-axis wind turbines (HAWTs) *Renewable and Sustainable Energy Reviews* 63 (2016) 506–519
- [26] M. L. Robinson, “The Darrieus Wind Turbine for Electrical Power Generation,” *Aeronaut. J.*, June 1981, pp. 244–255
- [27] Maître T, Amet E, Pellone C: Modeling of the low in a Darrieus water turbine: wall grid refinement analysis and comparison with experiments. *Renew Energy* 51(2013) 497–512
- [28] M.H. Mohamed : Performance investigation of H-rotor Darrieus turbine with new airfoil shapes *Energy* 47 (2012) 522-530
- [29] Xiao Q, Liu W, Incecik A : Flow control for VATT by Fixed and oscillating flap. *Renew Energy* 51 (2013) 141-152
- [30] Xiao Q, Liu W, Hu J: Parametric study on a cylinder drag reduction using downstream undulating foil *European Journal of Mechanics B/Fluids* 36 (2012) 48–62.
- [31] Crimi, P. Dynamic stall. *A G A R Do graph*, (172), 1973. ISSN 03652467.
- [32] Larsen, J. W., Nielsen, S. R. K. and Krenk, S. Dynamic stall model for wind turbine airfoils. *Journal of Fluids and Structures* 23(2007)959–982.
- [33] McCroskey, W. J. The phenomenon of dynamic stall Document ID:19830012625 (1981).
- [34] Brochier G., Fraunité P, Béguiert C, Paraschivou I. (1986), "Water Channel Experiments of Dynamic Stall on Darrieus Wind Turbine Blades", *Journal of Propulsion* 2, pp.445-449.
- [35] Fujisawa N, Shibuya S. Observations of dynamic stall on Darrieus wind turbine blades *Journal of Wind Engineering and Industrial Aerodynamics* 89, n. 2, pp.201-214. (2001)
- [36] Mclean J D, Crouch J D, Stoner R C, Sakurai S, Seidel G E, Feifel, W M, Rush H M: Study of the application of separation control by unsteady excitation to civil transport aircraft Technical report CR–1999–209338, NASA, 1999.
- [37] Gomes L, Crowther W, Wood N: Towards apractical piezoelectric diaphragm based synthetic jet actuator for high subsonic applications – effects of chamber and orifice depth on actuator peak velocity. In 3rd AIAA Flow Control Conference, San Francisco, California, 2006, paper AIAA-2006-2859.

- [38] Gad-el-Hak, M.: Flow Control: Passive, Active, and Reactive Flow Management, Cambridge University Press, Cambridge United Kingdom, Chapter 1, 2000.
- [39] Modi V.J. Ying, B. Yokomizo T. (1989). "Boundary Layer Control of Bluff Bodies Through Momentum Injection" SAE paper, 902225.
- [40] Ericsson L. E. (1993). "Unsteady flow separation on slender bodies at high angles of attack" *Journal of Spacecraft and Rockets* 30 (6), 689-695."
- [41] Cassel K. W. The effect of convective heat transfer on steady boundary-layer separation. *Journal of Fluid Mechanics*, 428(2001)107-13
- [42] Gopalkrishnan R, Triantafyllou MS, Triantafyllou GS, Barrett D Active vorticity control in a shear flow using a lapping foil. *J Fluid Mech* 274(1994) 1–21
- [43] Lai JCS, Yue J, Platzer MF (1997) Control of backward facing step flow using a lapping airfoil. ASME1997 FEDSM97-3307
- [44] Jones KD, Platzer MF (2006) Bio inspired design of lapping wing micro air vehicles an engineer's perspective. 44th AIAA Aerospace Sciences Meeting and Exhibit AIAA 2006-37
- [45] Xiao Q, Sun K, Liu H, Hu J Computational study on near wake interaction between undulation body and a D-section cylinder. *Ocean Eng* 38(2011) 673–683
- [46] Miao JM, Ho MH Effect of flexure on aerodynamic propulsive efficiency of lapping flexible airfoil. *J Fluids Struct* 22(2006) 401–419
- [47] Roland Schiestel (1998) : Les écoulements turbulents „modélisation et simulation“. 2e édition, éditions HERMES.
- [48] Ferreira C.J.S, Bijl H, van Bussel G. van Kuik G : Simulating Dynamic Stall in a 2D VAWT Modeling strategy, verification and validation with Particle Image Velocimetry data *Journal of Physics: Conference Series* 75 (2007) 012023
- [49]. Hansen M.O.L , D.N. Soresen : CFD model for Vertical Axis Wind Turbine. Wind Energy for the New Millennium-Proceedings of the European Wind Energy Conference, Copenhagen, Denmark, 2001.
- [50] Allet A, Halle S, Paraschivoiu I. Numerical simulation of dynamic stall around an airfoil in Darrieus motion. *Journal of Solar Energy Engineering*, 121(1999) 69–76
- [51] I. Paraschivoiu and A. Allet. Aerodynamic analysis of the Darrieus wind turbines including dynamic-stall effects. *Journal of Propulsion and Power*, 4(5) 1988.472–477
- [52] Paraschivoiu I Beguier C. Visualization, measurements and calculations of dynamic stall for a similar motion of VAWT: Proceedings of the European Wind Energy Conference, Herning, Denmark, 1998.
- [53] Paraschivoiu I. Wind Turbine Design - With Emphasis on Darrieus Concept. Polytechnic international Press, 2002.
- [54] Iida A, Kato K, Mizuno A. Numerical simulation of unsteady flow and aero-dynamic performance of vertical axis wind turbines with LES. 16th Australasian Fluid Mechanics Conference, Crown Plaza, Gold Coast, Australia; 2-7 December 2007
- [55] Chao Li, Songye Zhu , You-lin Xu , Yiqing Xiao 2.5D large eddy simulation of vertical axis wind turbine in consideration of high angle of attack flow *Renewable Energy* 51 (2013) 317-330

- [56] Shih T, Liou WW Shabbir A, Yang Z, Zhu J A new $k-\epsilon$ eddy viscosity model for high Reynolds number turbulent flows. *Comput Fluids* 24 (1995) 227–238
- [57] Nicoud F, Ducros F: Subgrid-scale stress modelling based on the square of the velocity gradient tensor. 1999, *Flow, Turbulence and Combustion*, Vol. 62 (3), pp. 183-200.
- [58] ANSYS® *Academic Research, Release 14, Help System, dynamic mesh Guide, ANSYS, Inc.*
- [59] Nabavi Y (2008) Numerical study of the duct shape effect on the performance of a ducted vertical axis tidal turbine. PhD thesis, University of British Columbia, Vancouver, Canada
- [60] Castelli MR, Englaro A, Benini E: The Darrieus tidal turbine: proposal for a new performance prediction model based on CFD. *Energy* 36(2011) 4919–4934
- [61] Amet E, Maître T, Pellone C, ACHARD JL. 2D numerical simulations of blade vortex interaction in a Darrieus turbine. *Journal of Fluids Engineering* 2009; 131/111103:1-15
- [62] Nakata T, Liu H : Aerodynamic performance of a hovering hawkmoth with flexible wings: a computational approach. *Proc R Soc Lond B Biol Sci* 279(2012) 722–731
- [63] Liu W, Xiao Q, Cheng F (2013) A bio-inspired study on tidal energy extraction with flexible flapping wings. *Bioinspir Bio-mim*. doi:10.1088/1748-3182/8/3/036011
- [64] Ashraf M, Young J, and Lai J: Reynolds number, thickness and camber effects on flapping airfoil propulsion. *Journal of Fluids and Structures* 27 (2011) 145–160
- [65] Hoke C.M, Young J, Lai J.C.S : Effects of time-varying camber deformation on flapping foil propulsion and power extraction *Journal of Fluids and Structures* 56 (2015) 152–176

Résumé

Dans le cadre de cette thèse, différentes stratégies de contrôle d'écoulement sont proposées pour améliorer les performances des turbines à axe vertical. La première stratégie est une turbine avec des pales flexibles, différents types de déformations sont étudiés. La deuxième stratégie est un contrôle par des ailes battantes. Une meilleure compréhension du comportement d'écoulement complexe à travers les turbines a été achevée. L'objectif ultime est de proposer un modèle robuste et efficace de VAWT. L'efficacité d'extraction d'énergie a été améliorée.

ملخص

في هذه الأطروحة، تم اقتراح استراتيجيات جديدة لمراقبة تدفق الرياح لتحسين فعالية التوربينات ذات المحور العمودي. اعتمدت الاستراتيجية الأولى على استخدام شفرات مرنة حيث تم دراسة تأثير أنواع مختلفة من التشوه. أما الاستراتيجية الثانية فاعتمدت على التحكم بالجريان باستخدام أجنحة خافقة. تم التوصل إلى فهم أفضل للسلوك المعقد للجريان. كان الهدف المرجو لهذه الأطروحة هو اقتراح نموذج قوي وفعال للتوربينات ذات المحور الرأسي وقد تحسنت كفاءة استخراج الطاقة بشكل ملحوظ.

Abstract

In this thesis, new flow control strategies are proposed to improve the vertical axis turbines efficiencies, the first strategy was a turbine with flexible deforming blades. Different types of deformation are investigated. The second strategy was a control by using backward flapping wings. A better understanding of the complex flow behavior across the turbines has been achieved. The ultimate objective was the proposition of a robust and efficient model for this type of turbines. The turbines energy extraction efficiency has been effectively improved.